

Molecular Dynamics Simulations of sheared brush-like systems

Dissertation

zur Erlangung des Grades

„Doktor der Naturwissenschaften“

am Fachbereich Physik, Mathematik und Informatik

der Johannes Gutenberg-Universität Mainz

vorgelegt von

Leonid Spirin

geboren in Moskau

Mainz, Juli 2010

Tag der mündlichen Prüfung: 15.10.2010

D77

Parts of the thesis have been published in
Galuschko, A.; Spirin, L.; Kreer, T.; Johner, A.; Pastorino, C.; Wittmer, J.; Baschnagel,
J. *Langmuir* **2010**, *26(9)*, 6418.

Zusammenfassung

Mit Hilfe von Molekulardynamik-Simulationen untersuchen wir bürstenartige Systeme unter guten Lösungsmittelbedingungen. Diese Systeme sind, dank ihren vielfältigen Beschaffenheiten, die von Molekularparametern und äußeren Bedingungen abhängig sind, wichtig für viele industrielle Anwendungen. Man vermutet, dass die Polymerbürsten eine entscheidende Rolle in der Natur wegen ihrer einzigartigen Gleiteigenschaften spielen. Ein vergrößertes Modell wird verwendet, um die strukturellen und dynamischen Eigenschaften zweier hochkomprimierter Polymerbürsten, die eine niedrige Reibung aufweisen, zu untersuchen. Allerdings sind die Lubrikationseigenschaften dieser Systeme, die in vielen biologischen Systemen vorhanden sind, beeinflusst. Wir untersuchen so-genannte "weiche Kolloide", die zwischen den beiden Polymerbürsten eingebettet sind, und wie diese Makroobjekte auf die Polymerbürsten wirken.

Nicht-Gleichgewichts-Molekulardynamik-Simulationen werden durchgeführt, in denen die hydrodynamischen Wechselwirkungen durch die Anwendung des DPD-Thermostaten mit expliziten Lösungsmittelmolekülen berücksichtigt werden. Wir zeigen, dass die Kenntnis der Gleichgewichtseigenschaften des Systems erlaubt, dynamische Nichtgleichgewichtseigenschaften der Doppelschicht vorherzusagen.

Wir untersuchen, wie die effektive Wechselwirkung zwischen kolloidalen Einschlüssen durch die Anwesenheit der Bürsten (in Abhängigkeit der Weichheit der Kolloide und der Pfpfödicke der Bürsten) beeinflusst wird. Als nächsten Schritt untersuchen wir die rheologische Antwort von solchen komplexen Doppelschichten auf Scherung. Wir entwickeln eine Skalen-Theorie, die die Abhängigkeit der makroskopischen Transporteigenschaften und der lateralen Ausdehnung der verankerten Ketten von der Weissenberg Zahl oberhalb des Bereichs, in dem die lineare Antwort-Theorie gilt, voraussagt. Die Vorhersagen der Theorie stimmen gut mit unseren und früheren numerischen Ergebnissen und neuen Experimenten überein. Unsere Theorie bietet die Möglichkeit, die Relaxationszeit der Doppelschicht zu berechnen. Wenn diese Zeit mit einer charakteristischen Längenskala kombiniert wird, kann auch das "transiente" (nicht-stationäre) Verhalten beschrieben werden.

Wir untersuchen die Antwort des Drucktensors und die Deformation der Bürsten während der Scherinvertierung für grosse Weissenberg Zahlen. Wir entwickeln eine Vorhersage für die charakteristische Zeit, nach der das System wieder den stationären Zustand erreicht.

Elektrostatik spielt eine bedeutende Rolle in vielen biologischen Prozessen. Die Lubrikationseigenschaften der Polymerbürsten werden durch die Anwesenheit langreichweitiger Wechselwirkungen stark beeinflusst. Für unterschiedliche Stärken der elektrostatischen Wechselwirkungen untersuchen wir rheologische Eigenschaften der Doppelschicht und vergleichen mit neutralen Systemen. Wir studieren den kontinuierlichen Übergang der Systemeigenschaften von neutralen zu stark geladenen Bürsten durch Variation der Bjerrumlänge und der Ladungsdichte.

Abstract

By means of Molecular Dynamics simulations we investigate brush-like systems under good solvent conditions. These systems are important in many industrial applications due to their rich properties depending on the molecular parameters and external conditions. It is believed that polymer brushes play a crucial role in nature due to their unique lubrication properties. A simple coarse-grained model is used to investigate structural and dynamic properties of two highly compressed polymer brushes that exhibit low friction. However, the lubrication properties of these systems are strongly influenced by embedded molecules, which often are present in biological systems. We study so-called "soft colloids", which are embedded between two polymer brushes, and investigate how these macroobjects effect the brushes.

Non-equilibrium Molecular Dynamics simulations are performed, in which hydrodynamic interactions are taken into account applying the DPD thermostat in presence of explicit solvent molecules. We show that the knowledge of the system's properties in static equilibrium allows to predict dynamic properties of the bilayer.

We study how the effective interactions between the colloidal inclusions are influenced by the presence of the brushes (as a function of the softness of the colloids and the grafting density of the brushes). As a next step, we investigate the rheological response of such complex bilayers to steady shear. We develop a scaling theory that predicts the dependence of the macroscopic transport properties and the lateral extension of the grafted chains on the Weissenberg number beyond linear response. The predictions are found to be in good agreement with our and previous numerical results and recent experiments. Our theory offers a way to calculate the relaxation time of the bilayer. This time, in a combination with a characteristic length scale, can be used further for a description of the transient behavior.

We investigate the response of the stress tensor and the deformation of the brushes during shear inversion for large Weissenberg numbers. We develop a prediction for the characteristic time after which the system reaches again steady state.

Electrostatics play a crucial role in many biological processes. The lubrication properties of polymer brushes are significantly influenced by the presence of long-range interactions. For different strengths of electrostatic interactions we investigate rheological properties of the bilayer and compare to neutral brushes. We show the continuous transition of the system properties from neutral to strongly charged brushes by varying the Bjerrum length and the charge density.

Contents

1	Theoretical and experimental approaches	11
1.1	Theoretical approaches	11
1.1.1	Free polymer chains in solution	11
1.1.2	Polymers in solution	12
1.1.3	Polymer brushes	15
1.1.4	Charged brushes	19
1.1.5	Sheared brushes	22
1.2	Experimental approaches	24
2	Model and simulation technique	27
2.1	Model	27
2.2	Electrostatic interaction and Ewald summation	31
2.3	DPD-thermostat	34
2.4	MD Simulations	35
3	Static Equilibrium	37
3.1	Introduction	37
3.2	Brushes-induced interactions	37
4	Steady-state shear	45
4.1	Introduction	45
4.2	Theoretical approach	46
4.2.1	Zimm dynamics	46
4.2.2	Rouse dynamics	49
4.3	Computer simulations	50
4.3.1	Density profiles and overlap region	50
4.3.2	Kinetic friction coefficient	56
4.3.3	Structure of brushes	59
4.3.4	Structure of stars	63
4.3.5	Viscosity and shear forces	65
4.3.6	Comparison to experiment and other numerical approaches	69

5	Non-stationary shear	73
5.1	Introduction	73
5.2	Shear inversion	74
6	Charged systems	91
6.1	Introduction	91
6.2	Influence of long-range interactions	91
7	Conclusions and outlook	99
	Bibliography	103

List of Figures

1	Schematic section through part of a hip joint	9
1.1	Schematic demonstration of rheological response of complex fluids	24
2.1	Interaction potentials between non-bonded and bonded beads	30
2.2	Snapshot of the system	31
2.3	Snapshot of stars, top view	32
3.1	Snapshots of the system for different pinning distances between stars	38
3.2	The volume fraction of the brush beads between the stars and the gyration radius of stars in X -, Y -, and Z -directions as a function of distance between them for different star configurations	40
3.3	Brushes-induced potential between two stars of different configurations for different grafting densities of the brushes, and the number of interactions between the stars and the brushes as a function of distance between stars	41
3.4	Brushes-induced potential between two colloids (hard spheres) as a function of distance between them	43
4.1	Density profiles of components of the system in static equilibrium and steady state	51
4.2	Profile of the chain ends of the brushes and center monomer distribution of stars in static equilibrium and in steady state	52
4.3	The brush height around the center monomer of a star	53
4.4	Overlap integral vs. the number of binary interactions between the brushes	54
4.5	Forces acting between the brushes vs. shear rate	55
4.6	Force acting between the brushes and the stars vs. shear rate	56
4.7	Forces between the brushes and the stars in gradient and shear direction vs. shear rate	57
4.8	The kinetic friction coefficient vs. shear rate for different grafting densities and different lengths of chains	58
4.9	The kinetic friction coefficient vs. shear rate for different star configurations and different densities of stars	59

4.10	Kinetic friction coefficient vs. shear rate for solvent-free case, systems with explicit solvent molecules (dimers), systems with stars	60
4.11	Gyration radius of chains in the brushes vs. shear rate	61
4.12	Rescaled gyration radius of chains in the brushes in shear and in gradient directions as a function of the Weissenberg number	62
4.13	Gyration radius of stars vs. shear rate for different star configurations fixing grafting density, chain length of brushes and distance between the substrates	63
4.14	Gyration radius of stars with large functionality and short arms' length vs. shear rate for different brushes' chain lengths and distances between substrates	64
4.15	Gyration radius of soft stars vs. shear rate for different grafting densities . .	65
4.16	Normalized viscosity vs. Weissenberg number	66
4.17	Normalized viscosity vs. Weissenberg number, deviations from the universal power-law behavior for systems with stars	67
4.18	Normalized shear force vs. Weissenberg number	68
4.19	Comparison of shear forces with experiment	70
4.20	Comparison of shear forces with grand canonical simulations	71
5.1	Shear protocol of the walls during shear inversion	74
5.2	Normalized shear stress vs. time during shear inversion	75
5.3	Response of the gyration radius of brushes onto shear inversion for different compositions of the system	76
5.4	Relative interpenetration between two opposing brushes, brush and star, inclination angle of chains in brush and brush height as a function of time during shear inversion	77
5.5	Comparison of the distribution of solvent molecules in the bilayer in static equilibrium, in steady state and during shear inversion at time point when the interpenetration between the brushes exhibits maximum	78
5.6	Velocity profiles of stars, solvent molecules, and brushes during shear inversion, four selected snapshots	79
5.7	The time series of the slip length of each component of the system and the relative interpenetration of chain ends into the opposing brush during shear inversion	81
5.8	Schematic picture of the behavior of the brushes and the stars during shear inversion	82
5.9	Gyration radius of the stars in X -, Y -, and Z -directions as a function of time during shear inversion	83
5.10	Gyration radius of the brushes in shear direction as a function of time during shear inversion for different compositions of the system and shear rates . . .	84

5.11 Gyration radius of the brushes' chains normalized by its value in steady state as a function of rescaled time	85
5.12 The shear stress normalized by its value in steady state as a function of rescaled time	86
5.13 Response of the normal stress during shear inversion	87
5.14 Components of the normal stress during shear inversion. Layer resolved response of the component of the normal stress for interactions between the brush and the solvent molecules	88
5.15 Component of the normal pressure layer resolved due to the interaction between the solvent molecules; and component of the shear stress layer resolved due to the interactions between the brushes during shear inversion	89
6.1 Shear forces for the charged systems as a function of shear rate for different Bjerrum lengths and charge fractions	92
6.2 Kinetic friction coefficient for monovalent counterions, bivalent counterions and different charge fractions versus shear rate	93
6.3 Density profile and distribution of end monomers, comparison to neutral systems	94
6.4 Overlap between the brushes for different Bjerrum lengths as a function of shear rate	95
6.5 Difference between pair correlation functions of the brush monomers and the counterion monomers in steady state and static equilibrium	96
6.6 Charge profile for different Bjerrum lengths (from neutral to highly charged), comparison of sheared and unsheared systems	97

Introduction

Das einzige Mittel, die Welt zu verändern, ist sie zu verstehen.

Lion Feuchtwanger

A Polymer is a large molecule, called macromolecule, which consists of repeating structural units (monomers) connected by covalent bonds. The simplest polymers are poly(ethylene) or poly(styrene). If all segments have the same chemical composition, the polymer is called homopolymer. Properties of the polymers can be modified, such that they adsorb on surfaces. These systems are important in many phenomena and industrial applications, such as adhesion[1–3], stabilization of colloidal dispersions[4, 5], protection against corrosion[6], flotation of minerals[7–9], oil recovery[10], smart materials[11], wetting and spreading phenomena[12, 13], biotechnology[14], and so forth. A very important role in bio-nano-technology are playing so-called polymer brushes[12]. A polymer brush is a system of polymers irreversibly grafted by one chain end onto a surface. In a polymer brush, chains tend to stretch away perpendicular from the substrate due to the steric repulsion between the monomers. Of particular interest are two opposing brush-covered surfaces. They can carry very high normal loads, whereas simultaneously the resistance to lateral sliding motion can be extremely small. The resulting friction coefficients may be orders of magnitude smaller than those found in dry friction[15, 16]. Polymer brushes have thus important applications as lubricants, e.g. in machine parts or artificial joints[14]. Moreover, they are believed to play a crucial role in biolubrication, e.g. in synovial joints[17]. This effect of low friction is well established experimentally[15–18]. The macroresponse, e.g. shear and normal forces, or the viscosity can be measured experimentally, whereas investigations of the structure, e.g. density profiles, or of the underlying mechanism causing the low friction, are still incomplete. For these purposes computer simulation is the best tool. Like a high-resolution microscope it allows to investigate in detail stationary and non-stationary properties, forces acting in the system, as well as response and structure of the system on different length scales. Like a ballet-performance in the theater polymer brushes act in nature. Once one sits close to the stage, small details can be recognized - costumes, mimics of dancers, parts of

decoration. It looks interesting and every detail is important - like microproperties of the brush, e.g. local viscosity, interpenetration depth of the brushes, forces acting between them, velocity profiles of brushes, local structure of them. All these details depend on each other. They have their own rules - way of dancing, order of steps or order of appearing on the stage of decorations in correspondance with the libretto - like the behavior of microobjects, e.g. molecules, monomers and chemical bonds, accordingly to the laws of nature. All this creates the whole palette, which can be seen only on the macrolevel - further away from the stage, e.g. in the first circle in the middle. These best seats are the most expensive. Summing up all the properties it allows to see the beauty of the performance, and we see the great lubrication properties of the brushes. The correct model has to be chosen in order to see these effects, and to provide molecular factors causing the rheological response of the grafted layers to external stimuli missing in experiments. These model systems have been investigated extensively over the past decades, e.g. in Refs. [18–23, 26–38]. The vast majority of the numerical approaches have treated solvent effects without explicitly including solvent molecules in the simulations (implicit solvent simulation). Many of them have been done via the application of thermostats and the adjustment of the interaction potential between the monomers[13, 19, 21, 26, 31, 33, 34, 36, 37]. Other approaches have been made[18, 20, 22, 27, 28] by solving the Brinkman equation[39] for solvent- and monomer-flow field self-consistently. Solvent effects as well can be considered implicitly via the Lattice-Boltzmann method (see [40] and Refs. therein) or stochastic rotational dynamics[41]. Within the small number of investigations that have been carried out with an explicit solvent (see, e.g. Refs. [30, 32, 35, 38]), systematic studies of the effects neglected in implicit solvent simulations are rare[32].

In nature, e.g. in hip joints, one finds more complex systems than monodisperse neutral brushes, which have been investigated in majority of the studies. The lubrication in animals' and humans' joints are thought to be due to the presence charged macromolecules, aggrecans and lubricins - that extend to the surface to form a brush-like layer. Figure 1 shows a close-up view of the articular cartilage surface. The kinetic friction coefficient between the articular layers, compressed to 50 atmospheres or more in a hip joint, can be as low as 0.001 [42, 43]. Synthetic charged brushes ([91]) lead to low friction similar to that in the articular cartilage. It seems, that the mechanisms causing a decrease of friction coefficient in the simple system consisting only of two opposing polymer brushes is important also for these complicated systems. However, in order to model nature more realistically, the investigated systems have to be modified by taking into account inclusions, e.g. polymer stars or colloids and one can argue that simulations have to be carried out in the presence of explicit solvent molecules. Also electric charges are believed to play a role for the properties of such systems.

The main aim of the present work is to investigate the influence of such inclusions

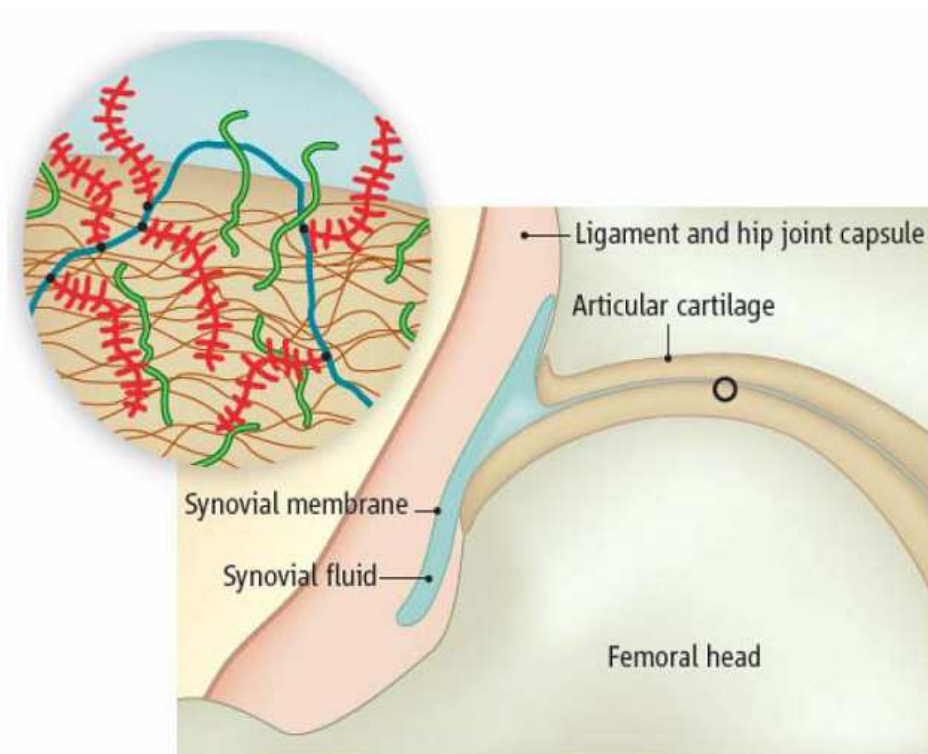


Figure 1: Schematic section through part of a hip joint [42]. Inset: charged macromolecules - acids (blue), to which aggrecans (red) and lubricins (green) are attached.

between the polymer brushes, e.g. of polymer stars, colloids, or explicit solvent molecules, on the viscoelastic properties and nanotribological aspects under steady shear conditions or non-stationary external stimuli. Moreover, we want to describe the structure of the systems and understand the characteristic relaxation times. For that purpose we use Molecular Dynamics simulations of a classical coarse-grained model. The systems under consideration consist of two opposing polymer brushes under good solvent conditions, with and without explicit solvent molecules, and with additional inclusions. We vary the degree of compression, the density and the length of grafted chains, the size and shape of the inclusions, e.g. configurations of the stars, size of colloids. Moreover, we extend our investigations to charged polymer brushes with explicit counterions. We study static equilibrium properties, Couette flows at various shear rates, and the response of the bilayer when the shear direction, starting from steady-state configurations of different shear rates, is instantaneously inverted.

In Chapter 1 different theoretical and experimental approaches are presented. In Chapter 2 model and simulation techniques are described. Chapter 3 deals with static

equilibrium properties and forces acting on the inclusions, which are located in the interface between two opposing brushes. Chapter 4 is devoted to the simulations and the newly developed scaling theory describing steady shear properties. These are followed by the nonequilibrium Molecular Dynamics simulations of the two opposing brushes during shear inversion and the theoretical approach in Chapter 5. Results of the simulations and the discussion of charged systems are presented in Chapter 6. The conclusions and plans for further work are given in Chapter 7.

Chapter 1

Theoretical and experimental approaches

1.1 Theoretical approaches

1.1.1 Free polymer chains in solution

The simplest model of a polymer chain is the freely-jointed chain model or random walk. According to this model the chain consisting of $N+1$ monomers is approximated by a sequence of N steps. The step (so-called bond vector) length is fixed, and equal to a , but the direction in which the step is taken is completely random and independent of all previous steps. This model is analogous to the randomly diffusing particle and permits the backfolding of a chain onto itself, the situation of a so-called random walk. The average displacement of the particle in this case is zero. Therefore, it is meaningful to use the root mean square displacement as a characteristic parameter, which, in this case, is equal to the end-to-end radius R_e ,

$$R_e^2 \equiv Na^2 = La, \quad (1.1)$$

where $L = Na$ is the contour length of the chain.

For this model the characteristic length turns out to be proportional to the square root of the number of steps, N , $R_e \propto N^{1/2}$. This model describes ideal chains and does not account for interactions between monomers (excluded volume effects). This situation approximately is realized experimentally at a certain temperature or solvent condition, when the attraction between monomers effectively cancels their steric repulsion. This is the so-called theta-solvent condition.

Another way to characterize the average size of a polymer coil is to introduce the radius

of gyration,

$$R_g^2 \equiv \langle \mathbf{R}_g^2 \rangle \equiv \frac{1}{N} \left\langle \sum_i (\mathbf{r}_i - \mathbf{r}_{\text{cm}})^2 \right\rangle, \quad (1.2)$$

where \mathbf{r}_{cm} denotes the chain's center-of-mass position vector,

$$\mathbf{r}_{\text{cm}} \equiv \sum_i \mathbf{r}_i, \quad (1.3)$$

and \mathbf{r}_i is the position vector of monomer i .

In case of good solvent conditions the interaction between polymer segments and solvent molecules is favorable. Under this condition the chain is swollen, because monomers try to avoid each other in solution. The reason for this behavior is conformational entropy, which prevents full stretching of the chain in combination with the preferable interaction between monomers and solvent molecules. The standard model for taking into account interactions between monomers is the mean field Flory theory[45]. In case of repulsive interactions between the monomers, the positive second virial coefficient, ν_2 , is of order of the monomer volume, $\nu_2 \propto a^3$. The repulsive interaction between the monomers is balanced by the chain elasticity, which is due to the entropy loss because of chain stretching. According to the Flory theory for a flexible chain of radius R_g the free energy of a chain in units of the thermal energy $k_B T$ (k_B the Boltzmann constant) writes as a sum of two terms,

$$F \approx \frac{R_g^2}{R_i^2} + \nu_2 \frac{N^2}{R_g^3} \quad (1.4)$$

where $R_i \propto R_e$ is the radius of gyration of an ideal chain. The first term is the entropic elastic energy associated with swelling of a polymer chain multiplied by the effective spring constant of an ideal chain, $k_B T/R_i^2$. The second term is the second virial repulsive energy, proportional to N times the second virial coefficient, ν_2 , and the segment density of a monomer gas. Minimizing the free energy with respect to R_g one gets $R_g \propto aN^\nu$ with $\nu = 3/5$. This is the situation of the self-avoiding walk.

1.1.2 Polymers in solution

In the previous section we have recalled scaling concepts of a single polymer chain. In this section we will deal with polymers in solution, where c is the concentration of chains. There are three different regimes:

- a) dilute systems
- b) semidilute systems
- c) concentrated systems or polymer melts

In the case of dilute systems, chains do not feel each other and behave like single, independent chains. The scaling exponent of the gyration radius remains the same,

$R_g \propto aN^\nu$ for good solvent conditions. The crossover from the dilute to the semidilute regime occurs at the critical concentration, c^* , when chains start to overlap. In this case the chain behaves on different length scales differently. For this purpose another characteristic length can be defined, the so-called blob size, ξ_c . Within this length the chain behaves like a single independent chain of size $\xi_c \propto ag_c^\nu$, where g_c is the number of monomers within the blob. For distances larger than ξ_c the chain behaves like an ideal chain consisting of blobs of size ξ_c , and polymer segments can not distinguish any longer to which polymer chain they are connected. The gyration radius of chains reads

$$R_g \propto \xi_c n_c^{1/2}, \quad (1.5)$$

where n_c is the number blobs per chain, $n_c = N/g_c$, such that

$$R_g \propto (\xi_c/a)^{1-2/\nu} aN^{1/2}. \quad (1.6)$$

The blob-picture allows to represent a polymer solution as a network with a certain average mesh size, which is proportional to the blob size, ξ_c . While ξ_c depends on the concentration, the network structure and its characteristic size should not depend on the degree of polymerization N for a given $c > c^*$. We suppose, that the chains must be longer than the mesh size. When $c \approx c^*$, where coils are in contact but do not interpenetrate, the mesh size must be comparable with the size of one coil, R_g . These two requirements lead to the expression

$$\xi_c(c) \propto R_g \left(\frac{c^*}{c} \right)^\kappa. \quad (1.7)$$

Since $c \propto N/R_g^3$, one gets $c^* = a^{-3}N^{1-3\nu}$. The exponent κ must be such that the powers of N from $R_g(\propto N^\nu)$ and from the $c^*(\propto N^{1-3\nu})$ cancel. This means that $\kappa = \nu/(1-3\nu)$ and leads to

$$\xi_c \propto a(ca^3)^{(\nu/(1-3\nu))}. \quad (1.8)$$

An increase of concentration, c , leads to a decrease of the blob size, ξ_c . When it reaches the monomer size, $\xi_c = a$, at the second critical concentration, c^{**} , the system becomes highly concentrated, and excluded volume interactions within a chain are fully screened. In this case of so-called polymer melts the chain shows almost ideal behavior (excluded volume effects are negligible) and the polymers approximately follow random walk statistics, $R_g \propto aN^{1/2}$.

Dynamic properties of the chains also depend on the concentration. We will consider Rouse and Zimm descriptions.

The Rouse model is the simplest model of polymer dynamics. It is based on three key assumptions. The first one is that the chains consist of "beads" separated by bond-vectors

along the "springs". The second assumption is that the chains are phantom chains, meaning that they are allowed to cross themselves, i.e. the chains are ideal. The third assumption is the locality of response, which means that each bead experiences a force only from its two neighbors. In other words, while a Newtonian description requires the positions and momenta of all particles, the Rouse model only takes into account the positions of monomers and it does not take into account all correlation effects with other chains, or hydro dynamic interactions. The Rouse model assumes the following equation of motion

$$\frac{d}{dt}\mathbf{r}_i = \frac{1}{\psi}\mathbf{F}_i + \rho_i, \quad (1.9)$$

where ψ is the monomer friction coefficient, ρ_i the random displacement per unit time of monomer i , and \mathbf{F}_i the force acting on monomer i . The latter follows from

$$\mathbf{F}_i = -\frac{\partial V}{\partial \mathbf{r}_i}, \quad (1.10)$$

where the potential, V , can be derived from the assumption that the chains are Gaussian and consist out of beads and springs,

$$V = \frac{3k_B T}{2a^2} \sum_i^{N-1} (\mathbf{r}_{i+1} - \mathbf{r}_i)^2. \quad (1.11)$$

The random displacement per unit time is Gaussian white noise satisfying the fluctuation-dissipation theorem,

$$\langle \rho_i^\alpha \rangle = 0, \quad (1.12)$$

and

$$\langle \rho_i^\alpha(t) \rho_j^\beta(t') \rangle = 2 \frac{k_B T}{\psi} \delta_{ij} \delta_{\alpha\beta} \delta(t - t'), \quad (1.13)$$

where greek indices denote Cartesian indices. The stochastic displacements in different directions and of different monomers are assumed as statistically independent.

Looking at Eq. (1.9) for the center of mass, one sees that the drift forces cancel due to Newton's third law. Moreover, the friction coefficients of all the monomers can be added up. This property we will use later for calculation of shear forces for brush laers. The diffusion constant in this model can be derived as

$$D = \frac{k_B T}{N\psi}, \quad (1.14)$$

and therefore

$$D \propto N^{-1} \propto R_g^{-2} \quad (1.15)$$

The longest relaxation time can be found considering that the object will move its own

size within a time, τ_R ,

$$D\tau_R \propto R_g^2, \quad (1.16)$$

such that

$$\tau_R \propto R_g^4 \propto N^2. \quad (1.17)$$

While the Rouse model does not take into account hydrodynamic interactions, or transport of momentum, the Zimm model does not ignore these self-correlation effects. The main effect is the following: A monomer i is randomly kicked by a surrounding monomer j and both are moved by their random displacements per unit time ρ_i and ρ_j . The motion in this case is highly correlated due to fast diffusive momentum transport through the medium. The equation of motion in this case can be modified to

$$\frac{d}{dt}\mathbf{r}_i = \sum_j \mu_{ij}\mathbf{F}_i + \rho_i, \quad (1.18)$$

where μ_{ij} is the mobility tensor and the stochastic displacements satisfy the relation

$$\langle \rho_i^{\alpha\beta}(t)\rho_j^{\alpha\beta}(t') \rangle = 2k_B T \mu_{ij} \delta(t - t'), \quad (1.19)$$

where $\rho_i^{\alpha\beta}$ is the displacement tensor. This relation is due to the incompressibility constraints of the solvent flow. One can show that the diffusion constant in this case can be derived as

$$D \propto \frac{1}{R_g}, \quad (1.20)$$

indicating that the chain as a whole essentially moves like a Stokes sphere. The longest relaxation time of the Zimm model, τ_Z , can be found by requiring $D\tau_Z \propto R_g^2$, such that $\tau_Z \propto R_g^3 \propto N^{3\nu}$.

1.1.3 Polymer brushes

In this section we will review theoretical approaches describing polymer chains, which are grafted by one of their ends onto the surface: polymer brushes. First, let us consider a single chain consisting of N monomers end-grafted onto the surface. Like a single chain in solution, it has its characteristic size, $R_g \propto N^\nu$. Increasing the number of chains, N_g , which are grafted onto the surface of area A , one reaches a situation, when chains start overlapping, such that the grafting density,

$$\rho_g = \frac{N_g}{A}, \quad (1.21)$$

is equal to the so-called critical grafting density,

$$\rho_g^* = \frac{1}{\pi R_g^2}, \quad (1.22)$$

where πR_g^2 is the area covered by one unperturbed chain. For grafting densities below the critical grafting density ($\rho_g < \rho_g^*$) the polymers have a mushroom conformation, when the chains have a coiled form, similar to a mushroom, and do not interact with each other. For grafting densities beyond the critical grafting density ($\rho_g > \rho_g^*$) the polymers are stretched due to the repulsion between the chains, which leads to loss of entropy of each chain in comparison with the ungrafted chains. These brushes are called semidilute brushes. Further increase of the concentration leads to molten brushes, when the brushes are highly concentrated, such that no more solvent molecules can be in the system due to the incompressibility of the brushes. Therefore, another important variation among brushes is also the presence or absence of solvent for the behavior of the grafted polymer chains. With solvent the physical reason for the stretching of the chains from the surface is their affinity for the solvent or dislike of each other. When no solvent is present (melt conditions), the chains stretch away from the substrate in order to avoid overfilling space, since they are incompressible.

Due to the constraint that the chains are grafted, the polymers will not behave like free chains in solution. The oldest and simplest model describing the regime of chains that are fully stretched away from the surface is the Alexander model[46]. In this model each chain consists of blobs of the same size in the strongly stretched limit ($\rho_g \gg \rho_g^*$) under good solvent conditions. The free ends of the chains are located at the height h from the surface, such that the density profile has the form of a step-function,

$$\rho(z) = N\rho_g/h, \quad (z \leq h). \quad (1.23)$$

The stretching of the chains leads to an entropic free energy loss of h^2/R_g^2 per chain, and the repulsive energy density due to unfavorable monomer-monomer contacts is proportional to the monomer density times the excluded-volume parameter times the length of the chains, $\nu_2 N$. Analogous to the derivation of the gyration radius of a free chain in a good solvent the free energy per chain is then

$$\frac{F}{k_B T} \simeq \frac{h^2}{a^2 N} + \nu_2 \frac{\rho_g N^2}{h}. \quad (1.24)$$

Minimizing the free energy one obtains the equilibrium height h ,

$$h = N \left(\frac{2}{3} \nu_2 a^2 \rho_g \right)^{1/3}. \quad (1.25)$$

In contrast to the Alexander model, when the chains are supposed to be fully stretched away from the interface with uniform monomer density, experiments and simulations have shown that brushes demonstrate a rather rounded behavior and density profiles approach zero continuously.

Theoretical studies of surface-anchored polymers based on the self-consistent field theory

(SCFT) representing full mean-field treatments first introduced by Edwards[47] and the strong stretching theory(SST) formulated by Semenov[48] are more realistic in comparison with the scaling methodologies. These methods make no assumption about the structure of the system, i.e. about the density profile, but determine it self-consistently. Both theories are based on the same Gaussian chain model. The advantage of the SST is that it provides simple analytical predictions, while SCFT (in general) only can be solved numerically. The SST neglects fluctuations around the "classical path", which connects grafted and free end-monomers of a chain, by minimizing the action. This is in analogy with the classical approximation of quantum mechanics, where the motion of a particle is given by the quantum path with maximum probability. The SST also can be used in polymer adsorption theories as a chain connectivity equation resembling the diffusion equation, such that this method is called the diffusion equation approach. However, a major difference between a diffusing particle and a polymer molecule is the fact, that a polymer molecule has two chain ends whereas a diffusing particle does not have a specific end. A polymer segment located near one of the ends will in general behave differently from a middle segment, as the non grafted ends have more freedom of motion. In the original SST theory the importance of the chain ends is neglected.

A simple hypothesis about the free chain ends of a single polymer brush, that they may be located at any distance from the surface, leads to the prediction of a parabolic molecular field[49],

$$\Phi(z) = \Phi_0 - \frac{1}{2} \left(\frac{\pi z}{2h} \right)^2, \quad (1.26)$$

with Φ_0 a constant and h the height of the Alexander brush (except prefactors). The corresponding density profile is supposed to be proportional to the molecular field, $\rho(z) \propto \Phi(z)$. The end density distribution $\epsilon(z)$ obeys[49]

$$\epsilon(z) \propto 2z(h^2 - z^2)^{1/2} + (A/B - h^2)z(h^2 - z^2)^{-1/2}, \quad (1.27)$$

where A and B are constants derived in Ref. [49]. This is so-called Milner-Witten-Cates (MWC) model brush.

Now let us turn to the case of two opposing brushes. The key assumptions of the MWC theory are that two compressed brushes each have a parabolic molecular field and they do not interpenetrate into each other. Later calculations[50] showed the existence of an exponential tail in compliance with the SCFT. Further, assuming that the chains can slightly interpenetrate into each other, leads to the following form of the end distribution tail and the tail of the density profile:

$$\epsilon(z) \propto \rho(z) \propto \exp \left(-\pi \left(\frac{z - D/2}{\xi_t} \right)^{3/2} \right), \quad (1.28)$$

where ξ_t is the length of the tail, $\xi_t = (D/2)^{-1/3} a^{4/3} N^{2/3}$, and D is the distance between the opposing surfaces. This equation is derived for the case that only a small fraction of the chains stretches into the opposing brush, the so-called regime of weak compression.

With the full mean field approach[51] it can be shown that the tail exhibits the Gaussian form,

$$\epsilon(z) \propto \frac{z}{aN^{1/2}} \exp\left(-\frac{3z^2}{2a^2N}\right), \quad (1.29)$$

and

$$\rho(z) \propto \frac{aN^{1/2}}{z} \exp\left(-\frac{3z^2}{2a^2N}\right). \quad (1.30)$$

These predictions are not in perfect agreement with computer simulations results. Only in strongly stretched limit these two methods converges. More recent SST investigations[52–54] show that a depletion layer near the interface occurs, demonstrating that a parabolic molecular potential does not necessarily imply a parabolic density profile. Moreover, more recent studies have shown, that taking into account the entropy of the free ends [53] and finite-stretching corrections [54] lead to an almost perfect superposition of the SST and the SCFT, but the SST becomes analytically unsolvable.

Allowing brushes to interpenetrate into each other one can show that in the case of concentrated or molten brushes the overlap thickness can be derived from the change in free energy, ΔF , when a chain segment of length δ is pushed into the opposing layer. Witten *et al.* [55] demonstrated that by the calculation of the work in order to insert a single chain into a brush, ΔF can be written as

$$\Delta F \propto \left(-\frac{\delta^3}{a^2} \frac{\partial \Phi(z)}{\partial z}\right)^{1/2}, \quad (1.31)$$

where the molecular field, $\Phi(z)$, may be of the classical parabolic form, Eq. 1.26. The interpenetration is due to thermal fluctuations, thus ΔF is of the order $k_B T$. We take the derivative of $\Phi(z)$ at the middle of the bilayer, $z = D/2$, and obtain from Eq. (1.31)

$$\delta \propto \left(\frac{N^2 a^4}{D}\right)^{1/3} \quad (1.32)$$

for the interpenetration depth of strongly compressed, molten bilayers.

Equation (1.32) is similar to the expression found by Witten *et al.* [55],

$$\delta \propto \left(\frac{N^2 a^4}{h}\right)^{1/3},$$

where D is replaced by the unperturbed brush height. The difference occurs because in Ref. [55] the derivative of $\Phi(z)$ is taken at $z = h$, which hence characterizes the behavior of two brushes just coming into contact (weak compression regime). The prediction of

the interpenetration depth [Eq. 1.1.3] we will use below in the theoretical description of two opposing brushes under shear.

1.1.4 Charged brushes

Polyelectrolytes are polymers containing ionizable subunits which can dissociate in a polar solvent providing charged macroions and counterions. There are polycations (positively charged chains), polyanions (negatively charged chains) and polyampholytes, which contain both negatively and positively charged subunits placed along the polymer chain. The model of a polyelectrolyte chain in solution is similar to the neutral one. A chain consists of N monomers each of size a . The degree of ionization or the monomer charge fraction can be characterized by the number of charged monomers, m ,

$$f_i = \frac{m}{N}. \quad (1.33)$$

Many analytical calculations for polyelectrolytes in solution start from the Poisson equation,

$$\nabla^2 \phi(\mathbf{r}) = -\frac{\rho(\mathbf{r})}{\epsilon_0 \epsilon(\mathbf{r})}, \quad (1.34)$$

where $\phi(\mathbf{r})$ is the potential at point \mathbf{r} , $\rho(\mathbf{r})$ is the local charge density, ϵ_0 is the vacuum permittivity, and $\epsilon(\mathbf{r})$ is the dielectric permittivity of the medium, which in most models is a constant, $\epsilon(\mathbf{r}) = \epsilon = \text{const}$. For a point charge with a charge density $\rho(\mathbf{r}) = Q_1 \delta(\mathbf{r} - \mathbf{r}_1)$ being located at $\mathbf{r} = \mathbf{r}_1$ and having a total charge $Q_1 = z_1 e$, where e is the elementary charge, the potential is given by

$$\phi(\mathbf{r}) = \frac{1}{4\pi\epsilon_0\epsilon} \frac{Q_1}{|\mathbf{r} - \mathbf{r}_1|}. \quad (1.35)$$

For a system of several ionic species each of valence z_i and with local concentration c_i the local charge density reads

$$\rho(\mathbf{r}) = e \sum_i z_i c_i(\mathbf{r}). \quad (1.36)$$

In the mean field approach, i.e. neglecting fluctuations, $c_i(\mathbf{r})$ obeys the Boltzmann distribution

$$c_i(\mathbf{r}) = c_i^{(0)} \exp\left(-\frac{z_i e \phi(\mathbf{r})}{k_B T}\right), \quad (1.37)$$

where $\phi(\mathbf{r})$ is the time averaged value and $c_i^{(0)}$ is the bulk concentration, such that the

requirement of electroneutrality gives

$$\sum_i z_i c_i^{(0)} = 0. \quad (1.38)$$

In this case the Poisson-Boltzmann (PB) equation

$$\nabla^2 \phi(\mathbf{r}) = -\frac{e}{\epsilon_0 \epsilon} \sum_i z_i c_i^{(0)} \exp\left(-\frac{z_i e \phi(\mathbf{r})}{k_B T}\right) \quad (1.39)$$

can not be solved analytically. Another approximation is necessary. The linearized PB equation reads

$$\nabla^2 \phi(\mathbf{r}) = \frac{1}{\lambda_D} \phi(\mathbf{r}), \quad (1.40)$$

where the Debye length is the screening length, defined as

$$\lambda_D \equiv \sqrt{\frac{\epsilon_0 \epsilon k_B T}{e^2 \sum_i z_i^2 c_i^{(0)}}}. \quad (1.41)$$

This is the so-called Debye-Hückel approximation. It is valid only for weak potentials

$$\phi(\mathbf{r}) \ll \frac{k_B T}{z_i e}. \quad (1.42)$$

Assuming the charge of all the other ions to be continuously smeared around a test charge, the spherically symmetric solution of Eq. (1.40) is

$$\phi_i(\mathbf{r}) = \frac{z_i e}{4\pi \epsilon_0 \epsilon} \frac{\exp(-r/\lambda_D)}{r} \quad (1.43)$$

and the corresponding pair interaction energy reads

$$U_{ij} = z_i z_j k_B T \frac{\lambda_B}{r} \exp(-r/\lambda_D), \quad (1.44)$$

with the Bjerrum length, λ_B , defined as the distance at which the Coulomb interaction between two unscreened elementary charges is equal to the thermal energy,

$$\lambda_B \equiv \frac{e^2}{4\pi \epsilon_0 \epsilon k_B T}. \quad (1.45)$$

The Bjerrum length characterizes the strength of the Coulomb interaction, whereas from Eq. (1.43) it is evident that the charge cloud around a test ion results in a screening of the Coulomb interaction. Hence, the Debye length gives the screening range of the resulting effective potential.

The Flory-like mean field argument can be, analogously to the neutral systems, used to calculate the end-to-end distance. Assuming all monomers are charged (monomer charge

fraction $f_i = 1$) the free energy is written as

$$\frac{F}{k_B T} \simeq \frac{R_e^2}{N a^2} + \lambda_B \frac{N^2}{R_e}, \quad (1.46)$$

where the first term is the elastic free energy of the Gaussian chain and the second term represents the electrostatic free energy of the charged monomers. The end-to end distance in this case is

$$R_e \simeq \lambda_B^{1/3} a^{2/3} N. \quad (1.47)$$

The linear dependence of R_e on N makes the strongly charged chain rod-like. The deviation from the rod-like structure is described by the Odijk-Skolnick-Fixman (OSF) theory[56].

To understand the scaling picture of charged brushes, one assumes a box model[57], where the brush is characterized by two length scales. The polymer chains are assumed to extend to a distance h from the grafting surface, the counterions in general form a layer of thickness H . There are two different regimes. In the first one the counterion cloud exceeds the height of the brush, $H > h$. In the second regime they are confined inside the brush, $H \approx h$. This is a strongly charged brush in contrast to the first case of a weakly charged brush.

There are four contributions to the free energy. First, the osmotic free energy F_{os} associated with the entropy cost of confining the counterions to a layer of thickness H is given by

$$F_{os} \simeq N f_i \rho_g \ln \frac{N f_i \rho_g}{H}. \quad (1.48)$$

Afterwards the second virial contribution to the free energy and the stretching free energy have to be taken into account. They are the same as for the neutral brushes [see Eq.(1.24)].

The third term is the electrostatic contribution. This term is nonzero when the brush is not locally electroneutral throughout the system. This is given by [57]

$$F_{el} \simeq \lambda_B (N f_i \rho_g)^2 \frac{(h - H)^2}{H}. \quad (1.49)$$

For strongly charged brushes all counterions are inside the brush, which means that the Gouy-Chapman length

$$\lambda_{GC} = \frac{1}{2\pi \lambda_B N f_i \rho_g}, \quad (1.50)$$

which is the height at which counterions are effectively bound to a surface of charge density $e f_i N \rho_g$ [58]. This height is small compared to the brush height h . For weakly charged brushes it can be shown that the counterion height reads

$$H \simeq h + \frac{3}{2}\lambda_{GC}. \quad (1.51)$$

In the case of the so-called osmotic brush regime[58] one can show, via minimizing osmotic and stretching free energies, that the brush height reads

$$h \simeq Naf_i^{1/2}. \quad (1.52)$$

Minimization of stretching and electrostatic free energies leads to the Pincus brush regime, where the brush height is

$$h \simeq N^3(af_i)^2\lambda_B\rho_g. \quad (1.53)$$

For both regimes there is a strong dependence on the Bjerrum length λ_B and the charge fraction f_i .

The picture of the polyelectrolyte brush behavior changes if salt is added to the solution. The salt concentration is an important parameter to tune structure and properties of the brush. Both in experiments and in theoretical work the main attention is focussed on the behavior of the brush height and density profiles. The brush height is predicted to be

$$h \simeq Na \left(\frac{\rho_g f_i^2}{ac_s} \right)^{-1/3}, \quad (1.54)$$

where c_s is the salt concentration. There are, however, also another prediction[58] expecting $h \propto c_s^{-2/3}$ and $h \propto c_s^{1/3}$ [59]. Despite of the different predicted exponents of the power laws one can conclude that the structure of the brushes strongly depends on the salt concentration.

In contrast to neutral brushes at low grafting densities, when chains are not overlapping, one observes a pancake conformation due to the long-range interaction. Increase of the critical grafting density leads to the mushroom conformation and further to the brush conformation. The crossover appears at lower grafting densities and, therefore, at lower critical concentrations in comparison with neutral systems.

Concluding, one can see that polymer brushes exhibit rich behavior when charged depending on the strength of the long-range interactions and molecular parameters of the system.

1.1.5 Sheared brushes

Now let us turn to the description of the brushes under shear. In case of ideal viscous (Newtonian) fluids, the stress depends only on the current rate of deformation, and there is no memory of previous deformations. At the other extreme of perfect elastic solids, stress depends only on the deformation from the preferred shape. Energy is dissipated in

viscous materials and stored in elastic bodies. Polymeric fluids are called viscoelastic, as they have both viscous and elastic properties depending on the time scale of observation. Elasticity is the ability of the fluid to return to its original state and shape after release of the applied stress. In most cases either the relaxation time of the material undergoing deformation is so small that the fluid exhibits mostly viscous response, or the relaxation is very slow (structural memory is very long) and materials behave like elastic bodies. Macromolecular fluids are unique since their structural relaxation times often span many orders of magnitude. For instance, chains grafted to surfaces might have different relaxation times than free chains of the same length located in the interface between two opposing brushes. The relaxation time of the system as a whole is influenced by all components.

Ideal Newtonian liquids placed between two opposing surfaces exhibit a linear velocity profile under shear. Complex systems, i.e. polymer brushes, do not show a linear velocity profile during steady shear. The mechanical response of any fluid to shear might be described by the viscosity, which can be calculated from the shear stress, σ_{xz} ,

$$\eta_{xz}(\dot{\gamma}) \equiv \sigma_{xz}/\dot{\gamma}, \quad (1.55)$$

where $\dot{\gamma}$ is the shear rate and σ_{xz} is an off-diagonal element of the stress tensor (X is the shear and Z is the gradient direction). For ideal viscous materials the shear forces are always proportional to the shear rate (linear response), and normal forces represent the pressure in the system. Macromolecular systems exhibit shear rate dependent viscosities. Another characteristic of system under shear is the Weissenberg number, W , which is typically defined as a product of the shear rate, $\dot{\gamma}$, and the characteristic relaxation time of the system τ ,

$$W = \dot{\gamma}\tau. \quad (1.56)$$

For such systems as polymer brushes one often takes the relaxation time of a single chain of equivalent length N in the bulk. Another example is the system of polymer stars, where the relaxation time of arms in the bulk is taken[60]. As we will show in the following, these definitions of the Weissenberg number is not applicable for such complex systems. Let us (re)define the Weissenberg number by the critical shear rate $\dot{\gamma}^*$, when the crossover from the linear response regime to the non-Newtonian behavior occurs,

$$W \equiv \dot{\gamma}/\dot{\gamma}^*. \quad (1.57)$$

The shear force in the linear response regime is proportional to the Weissenberg number up to the critical shear rate $\dot{\gamma}^*$. For Weissenberg numbers above the critical shear rate ($W > 1$), the system can exhibit a shear thinning or a shear thickening. Similarly to a

system of dendrimers or of polymer stars in the bulk the system of two opposing brushes may reveal a power law dependence with an exponent $\alpha < 1$ and $\alpha > 1$, correspondingly. As we will see in the following the first case is applicable independently of the molecular parameters, i.e. grafting density, chain length. This is the case of the so-called non-Newtonian behavior.

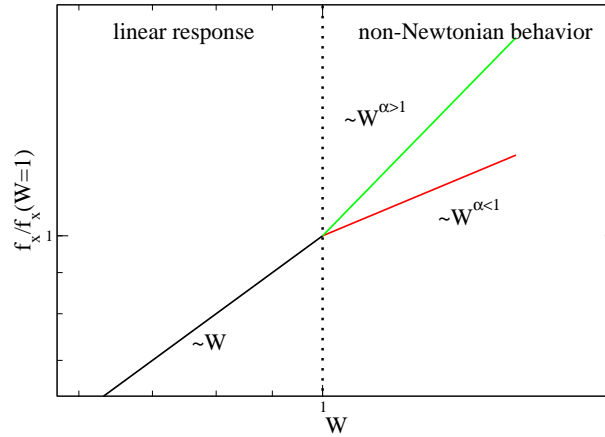


Figure 1.1: Schematic demonstration of shear thinning and shear thickening. Normalized by its value at the critical shear rate the shear force shows linear response behavior up to a Weissenberg number $W = 1$. For $W > 1$ the system reveals non-Newtonian behavior.

For increasing shear force there is a spontaneous symmetry breaking when the work of the shear force acting on a chain exceeds the thermal energy. At higher shear rates the chains are deflected in the shear direction. Therefore, the critical shear rate $\dot{\gamma}^*$ can be defined by the comparison of the thermal fluctuations with the work. Defining as a characteristic length scale the gyration radius in shear direction, $R_{g,x}$, and the total shear forces acting on the substrates, $f_x(\dot{\gamma})$, the Weissenberg number may be written as

$$W \equiv \dot{\gamma}/\dot{\gamma}^* = \frac{f_x(\dot{\gamma})R_{g,x}}{N_g k_B T}, \quad (1.58)$$

where $\dot{\gamma}^* \propto 1/\tau$, which can be regarded as an inverse relaxation time of the bilayer, and $R_{g,x} \equiv \langle R_{g,x}^2 \rangle^{1/2}$ the gyration radius at zero shear. This definition of the Weissenberg number we will use in the following.

1.2 Experimental approaches

Experimentally there are two basic ways of producing a grafted polymer layer. The first method is the so-called "grafting from" method, when polymerization is started from the surface with a suitable surface-linked initiator. The monomers have to diffuse through

the forming brush layer and thus the reaction kinetics is fast, and quite high grafting densities can be reached, but this method can result in quite high polydispersity [61]. The second method is the "grafting to" procedure, when polymers are attached with special end-groups that act as anchors on the surface. This method has slow kinetics during the formation stage due to the fact that whole molecules have to diffuse through the grafted layer; only smaller grafting densities can be achieved, but the length of the anchored chains and their chemical composition is under better control. The chains can be physically or chemically adsorbed to the substrates. An example for the first case are zwitter-ionic end-groups attached to poly(styrene) chains that lead to binding to mica in organic solvents such as toluene or xylene [62]. Or poly(ethylene oxide) (PEO) adsorbs on inorganic surfaces like mica via an ion-exchange reaction and forms a polymer brush. The second method leads to stronger covalent binding and therefore a more stable attachment of end-grafted chains is possible. The examples are poly(dimethylsiloxane) chains which carry hydroxyl end-groups and undergo condensation reactions with silanols on a silica surface[63]. Diblock copolymers (two dissimilar polymers joint end-to-end) can also be used in order to produce polymer brushes, where one block adsorbs on the surface whereas the other experiences repulsion[64]. Examples are poly(styrene)(PS)-poly(vinylpyridine)(PVP) diblock copolymers on sapphire [65] or quartz substrates[66] in selective solvent, which is a poor solvent for the PVP and leads to strong adsorption onto the surface, but a good solvent for PS, stretching this block from the substrate. The better control and larger grafting densities can be achieved in the case of diblock copolymers on a liquid-air[67] or a liquid-liquid interface. The grafting density can be varied via the variation of the lateral compression and therefore of the area of interface[68]. As an example diblock PS-PEO[69] can be taken. The PS block is shorter, insoluble in water, and can be used as an anchor at the air/water interface. As the surface pressure increases and the unit area per polymer decreases, the PEO is expelled from the surface and forms a polymer brush. Finally, the chain may be attached to a "substrate" that is the narrow interface between microdomains in a melt or concentrated solution of diblock copolymers when the two blocks of the copolymer are strongly segregated.

Grafted polymer materials can be either non-charged (neutral) or charged polymers, so-called polyelectrolytes. Polyelectrolytes can be categorized in two groups: strong (quenched) or weak (annealed). A simplest polyelectrolyte may be defined as a homopolymer, where at least one monomer unit carries an ionizable group. Such a group may be a strong salt, acid or base, so that its charge is virtually independent of pH. This is the case of strong polyelectrolytes. Weak polyelectrolytes carry weakly acidic (e.g. carboxylic) or basic (e.g. amino) groups. Their solution behavior depends on pH, which can be varied, for example, by adding salt.

The structure of polymer brushes can be investigated using different techniques. The

force-balance technique used in surface force measurements allows to measure directly shear and normal forces[15] in rheological experiments. Moreover, this technique gives a rough measure of the brush height by measuring the force as a function of the separation between two solid surfaces[70, 71]. Atomic force microscopy (AFM) has been used to probe the structure of surface-anchored polymers by measuring the force between the polymers and the AFM-tip[72]. Experiments involving scattering techniques have been used to investigate the structure of end-grafted polymer systems. These include ellipsometry[73], evanescent wave fluorescence[74], infrared spectroscopy[75], neutron reflectivity[65], neutron scattering[76], small angle scattering (SANS)[77], etc. These techniques have been used to determine the extension of the copolymers from the substrate and the total number of molecules adsorbed onto the surface. Most of the techniques lack the resolution necessary to describe monomer density profiles near the surface. Neutron reflectivity and SANS are able to provide more complete data about the structure of the concentration profiles of end-anchored polymers.

Chapter 2

Model and simulation technique

2.1 Model

In our simulations the system consists of two opposing compressed polymer brushes. Chains include N monomers each of size a . The polymers are grafted onto a surface with one chain end. The brushes are monodisperse. The degree of polymerization, N , is equal to $N = 30$ or $N = 60$. These lengths are small enough to avoid entanglements in the bulk[78]. Reference [79] suggests that the entanglement length increases with decreasing thickness of a confined concentrated solution, such that we expect non-entangled chains for all systems under consideration.

In experiments it is impossible to synthesize and investigate pure brushes. Not all free chain are adsorbed on the substrates due to slow kinetics; some of them are ribbed off the surfaces, especially in rheology experiments. Moreover, in nature even more complex systems occur, which have different kinds of inclusions. In this way special functions can be realized, for example, in natural cells as studied in tribology[80]. In these systems bilayers of lipids play an important role, which form effectively two highly fluctuating brush layers, where proteins are located inside of them. As inclusions in our systems we simulate colloids of different softness. Star polymers can be a good model for such inclusions allowing to vary configurations from "fluffy" stars to spherical-like[60]. The configuration of polymer stars is varied through functionality, f , and number of monomers in each arm N_{mon} . Varying these two values we change the "softness" of the stars from rather "hard" stars with small length of arms, $N_{\text{mon}} = 3$, and large functionality, $f = 50$, to "softer" stars, with $N_{\text{mon}} = 15$ and $f = 10$ and to bigger stars with longer arms up to $N_{\text{mon}} = 30$, which is comparable with the degree of polymerization of our brushes. Hard colloids were simulated as hard spheres of size $\sigma = 3$. A more detailed list of investigated parameters can be seen in Table 2.1.

We vary the surface density of the grafted chains, ρ_g . Our smallest grafting density for $N = 30$ is $\rho_g \approx 1.1\rho_g^*$, and the biggest is $\rho_g \approx 8.8\rho_g^*$, where ρ_g^* is the critical grafting

D	N	ρ_g/ρ_g^*	N_{arms}	N_{mon}	ρ_{st}	Solvent
12	30	2.2	-	-	0	A
14.75	30	2.2	-	-	0	A
17.5	30	2.2	-	-	0	A
12	30	2.2	-	-	0	B
14.75	30	2.2	-	-	0	B
17.5	30	2.2	-	-	0	B
12	30	1.1; 2.2	5	30	0.22	C
12	30	2.2	3	50	0.22	C
12	30	2.2	10	15	0.22	C
12	30	2.2	15	10	0.22	C
12	30	2.2	12	12	0.22	C
12	30	2.2	30	15	0.44	D
12	30	2.2	21	21	0.44	D
14.75	30	1.1; 4.4	5	30	0.22	C
14.75	30	1.1; 4.4	10	15	0.22	C
14.75	30	2.2	3	50	0.22	C
14.75	30; 60	2.2	5	30	0.22	C
14.75	30; 60	2.2	10	15	0.22	C
14.75	30	2.2	15	10	0.22	C
14.75	30	2.2	12	12	0.22	C
14.75	30	2.2	15	30	0.44	C
14.75	30	2.2	30	15	0.44	C
14.75	30	2.2	21	21	0.44	C
17.5	30	1.1; 4.4	10	15	0.22	C
17.5	30	1.1; 4.4	5	30	0.22	C
17.5	30; 60	2.2	5	30	0.22	C
17.5	30; 60	2.2	10	15	0.22	C
17.5	30	2.2	3	50	0.22	C
17.5	30	2.2	15	10	0.22	C
17.5	30	2.2	15	30	0.44	D
17.5	30	2.2	30	15	0.44	D
17.5	30	2.2	21	21	0.44	D
12	30	2.2; 3.3	5	30	0.08	2
12	30	3.3; 3.3	10	15	0.08	2
14.75	30	2.2; 3.3; 4.4	5	30	0.06	2
14.75	30	2.2; 3.3; 4.4	10	15	0.06	2
17.5	30	2.2; 3.3; 4.4; 6.6	5	30	0.005	2
17.5	30	2.2; 3.3; 4.4; 6.6	10	15	0.005	2
17.5	30	3.3; 6.6	21	21	0.015	2
21	30	2.2; 3.3; 4.4; 6.6; 8.8	5	30	0.04	2
21	30	2.2; 3.3; 4.4; 6.6; 8.8	10	15	0.04	2

Table 2.1: Different parameter combinations under consideration: distance D between grafting planes, chain length N , and ratio between grafting density and (approximate) critical grafting density for chains of length $N = 30$, star configurations ("—" denotes systems without stars). Solvent A - implicit solvent systems without stars, Solvent B - explicit solvent as dimers without stars, Solvent C Solvent D - with stars of density $\rho_{\text{st}} = 0.22$ and $\rho_{\text{st}} = 0.44$ respectively. "2" denotes the case when only two stars are present in the system (for the simulations of the effective interactions).

density. With $\rho_g \approx \rho_g^*$, we consider a system just at the mushroom-to-brush crossover for the chain length $N = 30$. For $N = 60$ we consider one grafting density, $\rho_g \approx 2.2\rho_g^*(N = 30)$.

The distances between the grafting surfaces, D , investigated is equal to $D = 12\sigma$, $D = 14.75\sigma$, $D = 17.5\sigma$, and $D = 21\sigma$. With that we consider four different degrees of compression. Depending on N and ρ_g , this corresponds to compressions between $2h/D \approx 2$ and $2h/D \approx 6.5$ relative to the height h of a single, uncompressed brush without explicit solvent[81].

In many previous simulations[13, 19, 21, 26, 31, 33, 34, 36, 37], the solvent was treated implicitly, i.e. the kinetic energy dissipated to the solvent is mimicked by the application of a thermostat. We consider four different types of solvents; referred to as solvent A, B, C, and D in the following. Solvent A accounts for solvent effects only via the repulsive potential acting amongst the monomers in the brush. Solvent B consists of dimers, corresponding to "polymer" chains of $N = 2$. We use dimers instead of (e.g.) monomers for the solvent in order to hamper packing and to account for rotational and vibrational degrees of freedom. However, our approach does not aim at describing all features of a real solvent but rather attempts to reflect excluded volume and finite inertia effects, as well as the momentum transport of an explicit solvent. For a given parameter combination of N , ρ_g , and D we add solvent dimers until a total number density of $\rho = 0.9$ is reached. Solvent C is a mixture of dimers and star polymers of different functionalities and arm lengths, such that the density of star monomers is $\rho_{st} \approx 0.22$. The total number of monomers in one star is $fN_{\text{mon}} + 1$ taking into account the central monomer to which all arms are connected. Solvent D corresponds to density of star monomers $\rho_{st} \approx 0.44$. For all parameters (N, ρ_g, D) , except systems of Solvent A, we keep the total number density at $\rho = 0.9$.

Periodic boundary conditions are applied parallel to the surfaces in X - and Y - directions. The substrates are represented by rigid, face-centered cubic (fcc) crystalline surfaces with area $A = L_x L_y = 42\sigma \times 36.373\sigma = 1527.666\sigma^2$.

The components of the system are represented by the Kremer-Grest (KG) model[24, 25], which is a generic coarse-grained model that has been applied in many previous studies[13, 19, 21, 24, 26, 31, 33, 34, 36, 37, 78, 81]. In the KG model, monomers interact via the Lennard-Jones (LJ) potential,

$$U_{\text{LJ}}(r_{ij}) = \begin{cases} 4\epsilon[(\sigma/r_{ij})^{12} - (\sigma/r_{ij})^6 - (\sigma/r_c)^{12} + (\sigma/r_c)^6], & (r_{ij} < r_c) \\ 0, & (r_{ij} \geq r_c) \end{cases}, \quad (2.1)$$

where $\epsilon = 1$ and $\sigma = 1$ define the units of energy and length, respectively. r_{ij} denotes the distance between monomer i and j and r_c is the cut-off radius of the potential. We consider a purely repulsive polymer model, i.e. we choose $r_c = 2^{1/6}\sigma$, and shift U_{LJ} to

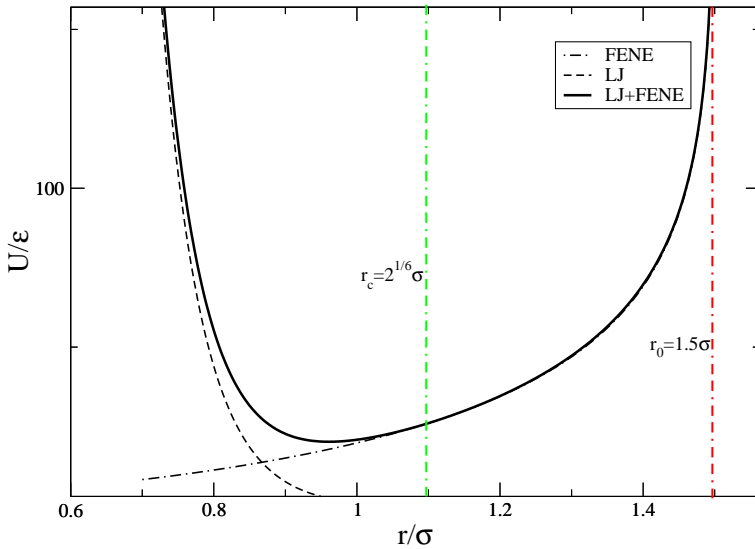


Figure 2.1: Interaction potentials between non-bonded and bonded beads, cut and shifted Lennard-Jones and FENE potentials and their sum (LJ+FENE).

avoid a discontinuous force at the cut-off. The excluded volume parameter in this case is $\nu_2 \approx a^3$ [82]. Since ν_2 is positive, we have good solvent conditions, independent of the temperature.

The connectivity along the chain backbone is assured via the FENE potential[24],

$$U_{\text{FENE}}(r) = \begin{cases} -\frac{1}{2}kr_0^2 \ln[1 - (r/r_0)^2], & (r < r_0) \\ \infty, & (r \geq r_0) \end{cases}, \quad (2.2)$$

where r is the distance between neighboring monomers in a chain, $k = 30\epsilon/\sigma$, and $r_0 = 1.5\sigma$. The equilibrium bond length, $b = 0.97\sigma$, follows from the minimum of $U_{\text{LJ}}(r) + U_{\text{FENE}}(r)$. The KG model prevents bond crossing and yields the characteristic properties of polymer solutions and melts[24, 78]. The potentials can be seen in Fig. 2.1.

We mimic the interaction of monomers and solvent with the wall atoms by Eq. (2.1) using the same values for r_c , σ , and ϵ as for the monomer-monomer interaction. The only exception concerns the interaction between the grafted end-monomers and the wall atoms, where we increase ϵ by a factor of 250 with respect to the monomer-monomer interaction and make the LJ potential attractive by doubling r_c . The wall atoms remain at fixed relative positions and move only with the given shear velocity. Using this approach, we imply chemisorbed polymer chains on a substrate with infinite mass.

Solvent molecules are simulated as LJ dimers. The connectivity of the latter, as well as of arms in stars and their bonding to the center monomer are assured via the FENE-potential, Eq. (2.2), with the same interaction parameters as for the

monomer-monomer interaction in the brush.

Figure 2.2 shows a typical snapshot of the simulated system. A top view on the stars, which shows the distribution of them in the system can be seen in Fig. 2.3. They strongly interact with each other as well as with the brushes.

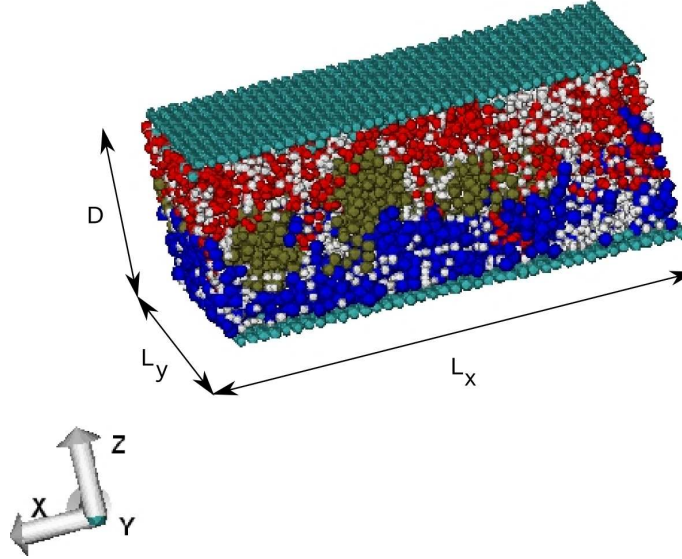


Figure 2.2: Typical snapshot of two polymer brushes with stars and explicit solvent molecules at static equilibrium. The distance between grafting planes is $D = 12$. Each brush consists of chains with $N = 30$ monomers per chain (blue and red beads). The grafting density is approximately twice the critical grafting density, at which the chains overlap. Green spheres are the stars and white spheres are solvent molecules (dimers).

2.2 Electrostatic interaction and Ewald summation

In charged systems ions are interacting via the long-range Coulomb interaction

$$U_{\text{Coul}}(r) = \frac{k_{\text{B}}Tq_iq_j\lambda_{\text{B}}}{r}, \quad (2.3)$$

where q_i and q_j are the corresponding charges in units of the elementary charge e , and λ_{B} is the Bjerrum length[Eq. 1.45].

In order to take this long-range interaction into account the Ewald Summation technique[83] was implemented. The electrostatic potential may be divided into the following contributions: interactions due to continuous background charge, self-interaction and real contribution due to screened charges. The first contribution may

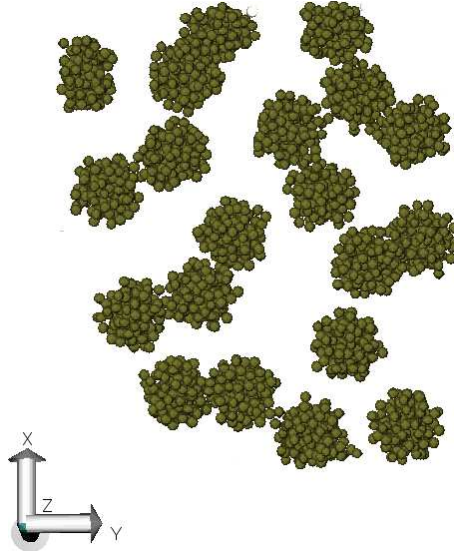


Figure 2.3: Top view of the system, only the stars are presented (green objects in the Fig. 2.2). They are located in the middle of the bilayer. The functionality of stars is $f = 30$, the number of monomers per arm is $N_{\text{mon}} = 5$.

be computed using Fourier transformation

$$U_f = \frac{1}{2V} \sum_{\mathbf{k} \neq 0} \frac{4\pi}{\mathbf{k}^2} |\rho(\mathbf{k})|^2 e^{-\mathbf{k}^2/4\alpha}, \quad (2.4)$$

where

$$\rho(\mathbf{k}) \equiv \sum_{i=1}^N q_i e^{i\mathbf{k} \cdot \mathbf{r}_i}, \quad (2.5)$$

with $\rho(\mathbf{k})$ the charge density in Fourier space, α the width of the Gaussian distribution, which is the compensating charge surrounding the ion, \mathbf{k} the lattice vectors in Fourier space, V the volume of the simulation box.

The second self-interaction contribution must be subtracted from the sum due to the periodic interaction of the continuous charge cloud, which is compensating the point charge q_i ,

$$U_{\text{self}} = \left(\frac{\alpha}{\pi}\right)^{\frac{1}{2}} \sum_{i=1}^N q_i^2. \quad (2.6)$$

The electrostatic energy due to the point charges and the compensating cloud in real space has the form

$$U_{\text{s-r}} = \frac{1}{2} \sum_{i \neq j}^N \frac{q_i q_j \text{erfc}(\sqrt{\alpha} r_{ij})}{r_{ij}}, \quad (2.7)$$

where r_{ij} is the distance between particles i and j , and

$$\operatorname{erfc}(x) \equiv 1 - \frac{2}{\sqrt{\pi}} \int_0^x e^{-u^2} du. \quad (2.8)$$

In order to take into account that the system is periodic only in two directions (slab geometry), it was shown[85], that one can add a correction term to obtain the correct limiting behavior in the limit of infinitely thin geometry ($D \ll L_x$ and $D \ll L_y$)

$$U_d = -\frac{2\pi}{V} M_z^2, \quad (2.9)$$

where

$$M_z = \sum_{i=1}^N q_i z_i, \quad (2.10)$$

with z_i the coordinate of the point charge q_i .

The total Coulomb energy is

$$U_c = U_f + U_{s-r} - U_{\text{self}} - U_d. \quad (2.11)$$

We vary degree of ionization from $f_i = 1$ (strongly charged polyelectrolyte), when every monomer of the chain has a charge $q = -1$, to $f_i = 1/30$ (the chain length is fixed $N = 30$), where only the end-monomer is charged. The Bjerrum length in this case is equal to size of monomers $\lambda_B = \sigma = 1$. Fixing the degree of ionization at $f_i = 1$ we also vary the Bjerrum length from $\lambda_B = 0.01\sigma$ up to $\lambda_B = 3\sigma$.

Charged systems are simulated under strong compression at a distance $D = 12$ between the walls; the grafting density is varied between $\rho_g = 1.1\rho_g^*$, $\rho_g = 2.2\rho_g^*$ and $\rho_g = 4.4\rho_g^*$; only the case of Solvent B is considered.

In order to keep the system electroneutral, such that

$$\sum q_i = 0, \quad (2.12)$$

where i goes over all charges in the system, counterions are added. Two cases of counterions are investigated. First, we treat counterions as LJ dimers like the solvent molecules. Every monomer of the dimer is charged, such that it is bivalent. In addition, we investigate systems with both monovalent counterions and solvent molecules, which, only for this special case, are treated as single monomers. Simulation results of the charged systems will be presented in Chapter 6.

2.3 DPD-thermostat

Temperature is kept constant at $T = 1.68\epsilon/k_B$ using a Dissipative Particle Dynamics (DPD) thermostat[83, 87–90]. The thermostat adds to the total conservative force on each particle i a dissipative force, \mathbf{F}_i^D , and a random force, \mathbf{F}_i^R . Both forces are applied in a pair-wise form, such that the sum of thermostating forces acting on a particle pair vanishes. With Γ the friction constant, the dissipative force reads

$$\mathbf{F}_i^D = -\Gamma \sum_{j(\neq i)} \omega^D(r_{ij})(\hat{\mathbf{r}}_{ij} \cdot \mathbf{v}_{ij})\hat{\mathbf{r}}_{ij}, \quad (2.13)$$

where $\hat{\mathbf{r}}_{ij} = (\mathbf{r}_i - \mathbf{r}_j)/r_{ij}$ and $\mathbf{v}_{ij} = \mathbf{v}_i - \mathbf{v}_j$ with \mathbf{r}_i and \mathbf{r}_j , \mathbf{v}_i and \mathbf{v}_j position vectors and velocities of particles i and j respectively. We choose the commonly employed weight function

$$\omega^D(r_{ij}) = \begin{cases} (1 - r_{ij}/r_c)^2 & (r_{ij} < r_c) \\ 0 & (r_{ij} \geq r_c) \end{cases}, \quad (2.14)$$

with the same cut-off range r_c as for the LJ interaction. The random force is given by

$$\mathbf{F}_i^R = \lambda \sum_{j(\neq i)} \omega^R(r_{ij})\theta_{ij}\hat{\mathbf{r}}_{ij}, \quad (2.15)$$

where θ_{ij} is a random variable with zero mean, unit variance, and $\theta_{ij} = \theta_{ji}$. $\omega^R(r_{ij})$ denotes the weight function for the random force. Friction and noise strength, λ , define the temperature via $\lambda^2 = 2k_B T \Gamma$. We choose $\Gamma = 5\tau_{LJ}^{-1}$ for the friction constant. In Ref. [35], a larger value ($\Gamma = 12.5\tau_{LJ}^{-1}$) was chosen. However, we want to avoid overdamping of the dynamics by the thermostat. During the simulation we monitor T and find isothermal conditions for all shear velocities considered here.

The fluctuation-dissipation theorem demands that the weight functions for dissipative and random forces satisfy

$$[\omega^R]^2 = \omega^D. \quad (2.16)$$

The weight function does not necessarily have to be of the specific form of Eq. (2.14). Instead one can choose a different function, as long as Eq. (2.16) is fulfilled. The strengths and weaknesses of different weight functions have been studied recently for the KG model without explicit solvent[37] and a slightly different model with solvent[35]. Using the DPD thermostat hydrodynamic interactions are taken into account and local momentum is conserved, such that the Zimm model is applicable to our results, which we will demonstrate in the following.

2.4 MD Simulations

To study the system we use Molecular Dynamics simulation methods[83]. The equation of motion for particle i is

$$m \frac{d^2 \mathbf{r}_i}{dt^2} = \mathbf{F}_i, \quad (2.17)$$

where \mathbf{F}_i is the sum of the all forces acting on the particle

$$\mathbf{F}_i = -\nabla_i U + \mathbf{F}_i^{\text{R}} + \mathbf{F}_i^{\text{D}} \quad (2.18)$$

where \mathbf{F}_i^{R} is defined in Eq. (2.15), \mathbf{F}_i^{D} in Eq.(2.13) and the potential is

$$U = U_{\text{LJ}} + U_{\text{FENE}} + U_{\text{c}} \quad (2.19)$$

where U_{LJ} in Eq. (2.1), U_{FENE} in Eq. (2.2) and U_{c} in Eq. (2.11).

We solve the classical equations of motion via the Velocity-Verlet algorithm[83]. It can be written in the following form:

$$\mathbf{r}(t + \delta t) = \mathbf{r}(t) + \delta t \mathbf{v}(t) + \frac{1}{2} \delta t^2 \mathbf{a}(t), \quad (2.20)$$

$$\mathbf{v}(t + \delta t) = \mathbf{v}(t) + \frac{1}{2} \delta t [\mathbf{a}(t) + \mathbf{a}(t + \delta t)]. \quad (2.21)$$

The algorithm is implemented in the following way. First, the new positions at time $t + \delta t$ are calculated using Eq. (2.20), and velocities at the mid-step are computed using

$$\mathbf{v}(t + \frac{1}{2} \delta t) = \mathbf{v}(t) + \frac{1}{2} \delta t \mathbf{a}(t). \quad (2.22)$$

The forces and accelerations at time $t + \delta t$ are computed and the velocity move completed

$$\mathbf{v}(t + \delta t) = \mathbf{v}(t + \frac{1}{2} \delta t) + \frac{1}{2} \delta t \mathbf{a}(t + \delta t). \quad (2.23)$$

The whole process is iterated using the newly computed positions and velocities. Since we get the velocities at each time step from Eq. (2.23), the instantaneous temperature can be calculated as

$$m \sum_{i=1}^{N_{\text{tot}}} \langle \mathbf{v}_i^2 \rangle = 3 N_{\text{tot}} k_{\text{B}} T, \quad (2.24)$$

where N_{tot} is the total number of monomers excluding surfaces particles.

We use a time-step of $\delta t = 2 \cdot 10^{-3} \tau_{\text{LJ}}$, where $\tau_{\text{LJ}} = \sigma(m/\epsilon)^{1/2}$ represents the LJ time unit. The particle mass, m , is set to unity for all monomers and solvent particles. We systematically checked that our results remain unchanged when the time-step is reduced to $\delta t = 5 \cdot 10^{-4} \tau_{\text{LJ}}$.

We consider stationary Couette flows, which are applied by shearing the substrates with a constant relative velocity of $2V$ at fixed distance D . The corresponding shear rate is defined as $\dot{\gamma} \equiv 2V/D$. All quantities will be presented in LJ units.

The response to shear may be characterized by the stress tensor, which can be calculated using the Irving-Kirkwood formula[86]

$$\sigma_{\alpha\beta} = \frac{1}{V} \left(\sum_i \mathbf{v}_\alpha \mathbf{v}_\beta H(z_i) \right) - \frac{1}{L_X L_Y} \left(\sum_{i < j} \frac{\mathbf{r}_{\alpha,ij} \mathbf{r}_{\beta,ij}}{|\mathbf{r}_{ij}|} \mathbf{F}_{ij} \frac{1}{z_{ij}} \theta \left(\frac{z - z_i}{z_{ij}} \right) \theta \left(\frac{z_j - z}{z_{ij}} \right) \right). \quad (2.25)$$

When the system is divided in the Z -direction into slabs of thickness Δz , $H(z_i)$ is expressed as

$$H(z_i) = \begin{cases} 1 & z - \frac{\Delta z}{2} < z_i < z + \frac{\Delta z}{2} \\ 0 & \text{otherwise} \end{cases} \quad (2.26)$$

Chapter 3

Static Equilibrium

3.1 Introduction

Polymer brushes are deeply investigated by means of theory[28, 49, 50, 55, 84], experiments[15, 17, 62, 65, 91, 92] and computer simulations[30, 31, 33, 34, 36, 37, 82]. In static equilibrium two opposing brushes can interpenetrate strongly into each other due to the non-parabolic tails of the brush-profiles. Computer simulations [93] demonstrate that highly fluctuating interface region between the brushes is built. A single brush expels macroobjects out of it [94, 95]. The influence of a single brush on two inclusions was extensively investigated by means of theory and computer simulations[94, 95]. These so-called effective interactions are observed in many systems, e.g. in biomembranes [96, 97], at fluid-fluid interfaces [98], in liquid crystals [99], in bilayer lipid membranes [100–102], in polymer-colloid mixtures [103] and so forth. Particularly, they are very important in cellular processes which lead to aggregation of proteins. We are interested in the interactions between two macroobjects located between two opposing brushes. These macroobjects are colloids or polymer stars of different softness. By varying the functionality, f , and the number of the monomers per arm, N_{mon} , we vary the size and the shape of the object. We will investigate the influence of the brushes on the interactions between these objects.

In this section, the results of simulations concerning the effective interactions in static equilibrium between stars and colloids in the brush-brush interface will be presented.

3.2 Brushes-induced interactions

The stars, when located close to each other, experience steric repulsion[104], therefore they do not prefer to be in contact. In order to investigate effective interactions between two objects and to "scan" all distances between them one can use, for example, umbrella sampling[83]. Experimentally, rare configurations can be investigated using laser

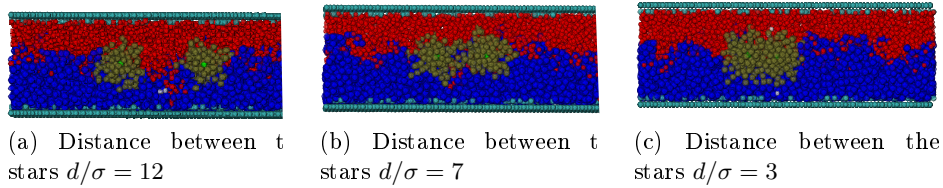


Figure 3.1: Snapshots of the system, two opposing brushes and two stars in the interface between them. Blue and red beads correspond to top and bottom brushes, green beads to the stars, light green to the center monomer. Close to each other two stars build one big object (3.1c). When the brushes are slightly separated the brushes start to penetrate between the stars (3.1b). At large enough distances the stars do not feel each other (3.1a). The grafting density is $\rho_g = 3.3\rho_g^*$, the distance between the walls is $D = 17.5$, the star configuration is $N_{\text{mon}} = 5$, $f = 30$.

traps[105], where the interaction potential is probed using laser tweezers. Similarly to this method we connect the center monomers of the stars to a fixed position in space by a spring. The spring constant is taken to be $k = 100$. This spring allows us to keep the objects close to each other. Due to interactions between polymer stars the position of the center monomers after equilibration differs from the pinning position. There is an effective potential between the stars, which is

$$U_{\text{st-st}}^0 = \frac{k\Delta x^2}{2}, \quad (3.1)$$

where Δx is the difference between the measured position of the center monomer and the pinning position. Δx depends on the relative position of the center of mass of the stars. Our aim is to investigate the deformation of the stars, moreover to study how the effective potential between these two objects is influenced by the presence of the brushes. The latter can be calculated from the difference between the potential, which acts between the stars in the presence of the brushes, $U_{\text{st-st}}^b$, and the pure potential acting between them, when there are no brushes in the system, $U_{\text{st-st}}^0$,

$$U_{\text{b-st}} = U_{\text{st-st}}^b - U_{\text{st-st}}^0. \quad (3.2)$$

In both situations the potentials between the stars can be directly measured via the position of the center monomers. Computer simulations allow to investigate in detail the relative deformations of each object in order to understand the nature of the occurring interactions.

The pinning distance d is the distance between the center monomers of the stars. We varied the pinning distance between $d/\sigma = 3$ and $d/\sigma = \min(L_x/2, L_y/2)$, where L_x and L_y are the sizes of the simulation box in X - and Y - directions, in which periodic boundary conditions are applied. The position of the center of mass of each star depends

on its deformation by the brushes. All measured variables will be presented as a function of the distance between the center of mass of each star, r_{cm} .

The monomers in the system are charge neutral. The length of the chains in the brushes is fixed to $N = 30$ for all simulations. The grafting density, ρ_g is varied between $\rho_g = 0.085$ and $\rho_g = 0.34$. This corresponds to $2.2\rho_g^*$ and $8.8\rho_g^*$, where ρ_g^* is the critical grafting density from which on chains within a brush start to overlap. Several star configurations were investigated as well as different separations between the walls. Snapshots of the investigated systems for different pinning distances of the stars, d are presented in the Figs. 3.1. The stars are located in the middle of the bilayer between the two opposing brushes. The Y -coordinate of the pinning position is fixed for all simulations. The pinned center monomers are able to fluctuate around their equilibrium positions. The resulting fluctuations around the pinning points are less than 1% of the distance between the walls, D . Via variation of the pinning positions in X -direction we vary the distance d . The Figure 3.1c shows the system, when two stars are close to each other and the distance between the pinning points is $d/\sigma = 3$. The stars build one big object in this case. They interact with the brushes as a whole, such that the brushes are not able to interpenetrate between the stars. Both stars are significantly deformed compared to their free configuration, they become aspherical. Figure 3.1b shows the situation, when the stars still interact with each other, but the brushes start interpenetrating between them, whereas Fig. 3.1a corresponds to the situation, when two stars are separated completely. One can see that in all three snapshots the stars also strongly deform the brushes.

In the following we focus on two star configurations. The first one is $f = 30$, $N_{\text{mon}} = 5$, which is rather colloid-like, and the second one is $f = 15$, $N_{\text{mon}} = 10$, which is softer and easier deformable as will be seen below. The first star exhibits in the bulk the gyration radius $R_g^{\text{st}} = 1.74$ and the second one $R_g^{\text{st}} = 2.3$. The distance between the walls is fixed to $D = 17.5$ and we compare two grafting densities, $\rho_g = 6.6\rho_g^*$ and $\rho_g = 3.3\rho_g^*$.

It is known that two compressed brushes try to prevent penetration into each other. Similarly to the brushes, it is not favourable for the stars to penetrate into the brush and therefore they are strongly deformed in Z -direction. The dependence of the gyration radius of the stars on the distance between the center of mass of each stars normalized by their unperturbed size, $r_{\text{cm}}/R_g^{\text{st}}$, can be seen in Fig. 3.2.

Let us first analyse the configuration of the stars when they are far apart from each other ($r_{\text{cm}} > 4R_g^{\text{st}}$). The higher is the grafting density of the brushes the more aspherical becomes the star. Compared to the unperturbed star size, X - and Y -directions are influenced by the presence of brushes, but remain almost equal ($R_{g,x}^{\text{st}} \approx R_{g,y}^{\text{st}}$). The stars are squeezed in Z -direction. One can see that the softer is the star, the more compressed it is in Z -direction.

Let us turn now to the situation when the stars are close to each other ($r_{\text{cm}} < 3R_g^{\text{st}}$). Due

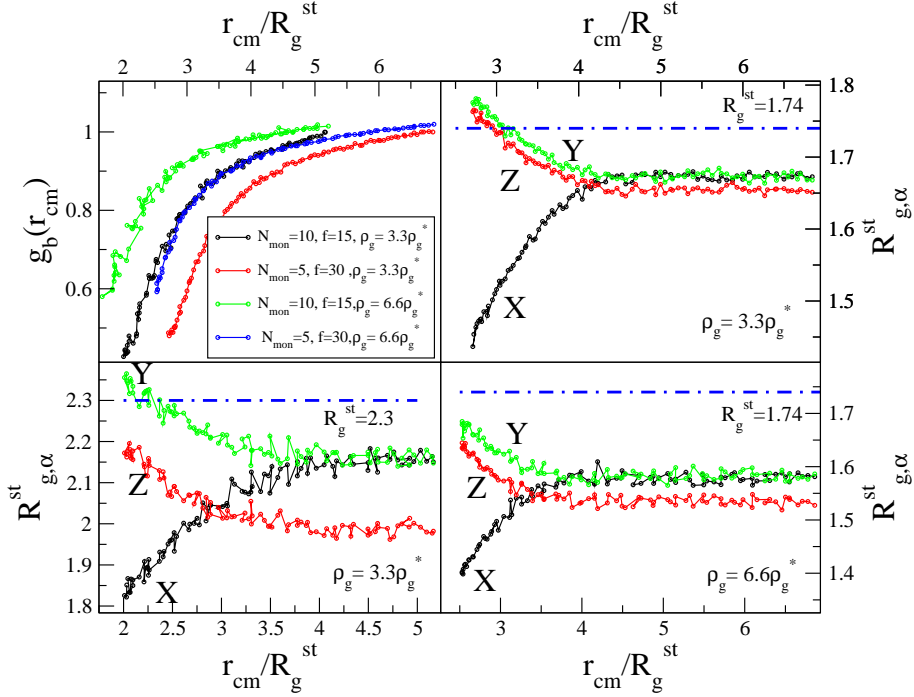


Figure 3.2: Normalized volume fraction of brush beads between the stars (upper panel), the gyration radius of stars (left bottom and the right panels) in X - (black lines), Y - (green lines) and Z -directions (red lines) as a function of reduced distance between centers of mass for different star configurations. The volume fraction of the brush beads increases continuously up to the distance of five times the gyration radius, $r_{\text{cm}} \approx 5R_{\text{g}}^{\text{st}}$. The gyration radius of the stars is influenced up to $r_{\text{cm}} \approx 4R_{\text{g}}^{\text{st}}$. Left bottom graph corresponds to the star configuration $N_{\text{mon}} = 10$, $f = 15$ with the gyration radius $R_{\text{g}}^{\text{st}} = 2.3$ (size of the unperturbed star), the right panel to the star configuration $N_{\text{mon}} = 5$, $f = 30$ with the gyration radius $R_{\text{g}}^{\text{st}} = 1.74$ (blue dashed-dotted line).

to the interaction with the other star the most significant deformation is in the X -direction, along which the pinning distance is varied. Due to the deformation in this direction, the stars are swollen in Y - and Z -directions. The size of stars differs in X - and in Y -directions up to $r_{\text{cm}} \approx 4R_{\text{g}}^{\text{st}}$, when the brush starts penetrating between the stars. In order to characterize it quantitatively we measure the volume fraction of the beads between two stars, $\phi^{\text{b}}(r_{\text{cm}})$, which is normalized by its value when the stars are infinitely far apart, for instance, in the half of the simulation box, $\phi^{\text{b}}(L_x/2)$.

$$g_{\text{b}}(r_{\text{cm}}) = \frac{\phi^{\text{b}}(r_{\text{cm}})}{\phi^{\text{b}}(L_x/2)}. \quad (3.3)$$

The left upper panel of Fig 3.2 shows $g_{\text{b}}(r_{\text{cm}})$. One can see that this number is growing upon increase of the distance between the stars. Comparing two configurations of the

stars one can see that the softer the star, the more deformable it is and, therefore, the number of brush beads between the stars is larger. The denser the brushes are, the earlier they penetrate between the stars. $g_b(r_{\text{cm}})$ reaches unity at the distance $r_{\text{cm}} \approx 5R_g^{\text{st}}$. This corresponds to the distances at which the brush between the stars do not feel the presence of the stars.

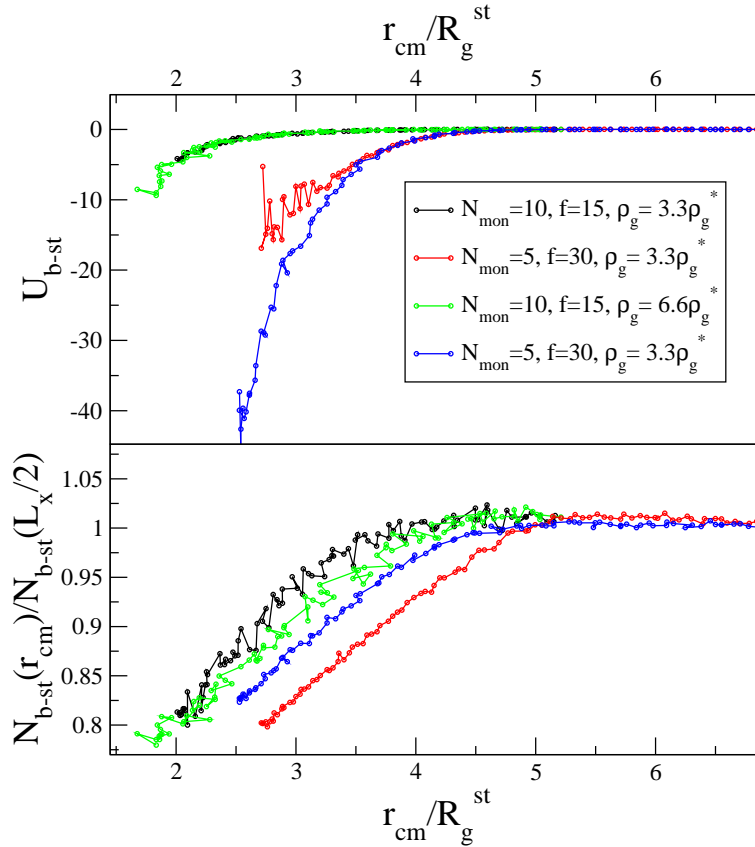


Figure 3.3: Brushes-induced potential between the two stars $U_{\text{b-st}}$ of different configurations for different grafting densities of the brushes and the number of interactions between the stars and the brushes normalized by the number of interactions when the stars do not interact with each other (at the distance between the stars equal to the half of the simulation box, $L_x/2$) as a function of distance between the inclusions. The potential reaches zero approximately when the number of interactions between the brushes and stars reaches a constant.

Now let us characterize how the brushes modify the interaction between the inclusions. One can see in Fig. 3.3 that it leads to attractive potential. Such behavior have been observed in polymer melts, when the attractive depletion interaction between colloids was observed [104]. Similarly to the case of polymer melts, an increase of the polymer density leads to a stronger attraction. But due to the irreversible anchoring to the walls and

strong ability to deform of the inclusions, the effect is much stronger (up to $40k_B T$) for the case of two opposing brushes with the stars. One can see, that the softer the star, the less influence has the brush on the effective interaction between them, even though softer stars are larger than the stars with higher functionality. The effective potential reaches zero at the distances between the centers of mass of about four times the radius of gyration of the unperturbed star, $d \approx 4R_g^{\text{st}}$, which is in the strong correlation with the deformation of the stars.

The effective potential can be characterized also in terms of the number of binary interactions between the brushes and the stars, $N_{\text{b-st}}$ (see Fig. 3.3, lower plot). When the macroobjects are close to each other, $N_{\text{b-st}}$ is smaller than when they are far apart. Similarly to the number of beads occurring between the stars, $g_{\text{b}}(r_{\text{cm}})$, the number of interactions grows upon increase of the distance between the stars. $N_{\text{b-st}}$ reaches a constant at distances $r_{\text{cm}} \approx 4R_g^{\text{st}}$. At this distance the stars stop interacting with each other and each macroobject behaves like a separate, independent one.

In case of so-called "fluid" brushes (allowing the grafted ends to freely move on the surface in X - and Y -directions), we expect a smaller influence of the brushes.

Next we replace the stars by two hard spheres. The diameter of the spheres, $R_c = 3\sigma$, is three times larger than the size of monomers in the brushes. In the case of the polymer melt one can observe entropy-induced short-range depletion forces [104]. The depletion zone is defined around the spheres at $2R_c < d < 3R_c$. These forces can be described and understood in terms of the Asakura-Oosawa approach [103], which predicts depletion interactions between them. The effect of the end-grafting of the chains does not increase strongly the depletion potential compared to the polymer melts. Upper plot of Fig. 3.4 shows the effective potential acting between two hard spheres as a function of the pinning distance between them, $U_{\text{b-co}}(d)$, for different grafting densities.

The higher the grafting density the more significant the influence of the anchored polymer chains. For the highest grafting density, $\rho_g = 6.6\rho_g^*$, a small periodicity appears. This may be due to the penetration of the brush-monomers between the pinned hard spheres. Increase of the distance between the walls fixing the grafting density of the brushes leads to a decrease of the density of the brushes in the system and, therefore, to a decrease of the influence on the interactions between the macroobjects. Our investigations reveal that the bigger the colloids, which are placed in the interface, the bigger the forces acting on them (not shown here).

Similarly to the case of stars, an increase of the grafting density leads to an increase of the number of binary interactions between the brushes and inclusions (Fig. 3.4, lower plot). For the highest grafting density one can see that the number of interactions shows an overshooting effect of $\approx 3\%$ and becomes even larger than for the case, when the two inclusions are far apart from each other. This happens at the distances when the potential shows a minimum in its periodic behavior. Since the brushes build a highly

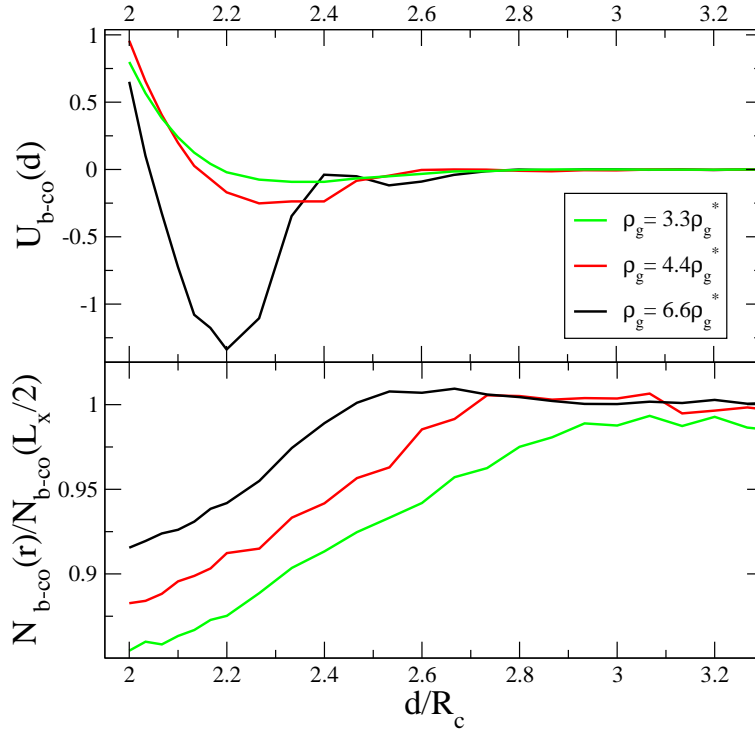


Figure 3.4: Brushes-induced potential between two colloids (hard spheres with radius $R_c = 3\sigma$) as a function of distance between the pinning points, d . The more brush beads are in the system, the more pronounced is the effective depletion interaction between the inclusions. The number of interactions between the brushes and hard spheres demonstrates an overshooting effect for the highest grafting density, when the periodicity appears in the brush-induced potential.

fluctuating interface, this periodicity may be interpreted also as a fluctuation induced forces, which have been discovered in the systems that consist of bilayer membranes with proteins [101].

Comparing the stars and the hard spheres one can conclude, that the shape, softness, the size and the components of the inclusions play a very significant role. The effective interactions between the stars are strong at small distances, when the objects are close to the direct contact with each other, therefore observed brush-induced potential of the soft inclusions has elastic nature. The periodicity of the potential that is observed for the hard spheres has not been measured for the soft objects. These forces are rather small with the small signal-to-noise ration due to high fluctuations of both, the brushes and the stars, and need a significant increase of statistics.

Chapter 4

Steady-state shear

4.1 Introduction

In this section we will present our investigations of two opposing, highly compressed polymer brushes with soft colloids. Our aim is to investigate the influence of the polymer stars on the response to shear, to study the structure of the bilayer and its relaxation time, and, moreover, to understand a possible mechanism of the low friction phenomena between two opposing brushes reported in experiments[15]. We start our description from the theoretical approach, which gives predictions for the behavior of the lateral extensions of the brushes, as well as shear forces and viscosity. Afterwards, we present computer simulation results which are in a good agreement with the newly developed theory. In our theoretical approach we first analyse the behavior of the system in linear response ($W < 1$), when shear forces are proportional to the Weissenberg number and the structure of the system is not influenced significantly by shear. Then, we study the behavior of the system for large Weissenberg numbers ($W \gg 1$) when the chains of the brush are strongly stretched. The starting point of our theory is that the two opposing brushes are highly compressed ($2h/D \geq 2$), such that the density profile in gradient direction exhibits an almost uniform behavior (except the layering effect at the walls). Moreover, we assume that the high compression leads to a flat density profile for all considered shear rates, such that the sum of the monomer density profiles of the brushes, $\rho_1(z) + \rho_2(z)$, ($\rho_1(z)$ and $\rho_2(z)$ are density profiles of the top and bottom brushes, respectively) is uniform. In the following, we therefore assume a uniform monomer concentration, $c \propto N\rho_g/D$, in the overlap region. We will use this feature below for the linear response regime. Moreover, let us assume that the brushes can be approximated by the MWC approach[55], such that each polymer brush provides parabolic molecular field [see Eq. (1.26)]. Let us allow the chain ends to interpenetrate into the opposing brush due to thermal fluctuations, such that the interpenetration depth, i.e. the overlap thickness of the bilayer, can be derived as in Eq. (1.32). The interpenetration depth, δ ,

depends on the degree of the polymerization, N , monomer size, a , the distance between the substrates, D , and the grafting density ρ_g .

4.2 Theoretical approach

4.2.1 Zimm dynamics

Let us first consider semidilute brushes. In this case, a brush may be considered as a dense melt of concentration blobs[45]. Each grafted chain in this case consist of the $n_c = N/g_c$ blobs, where g_c is the number of monomers in each blob, the size of each blob is ξ_c depends explicitly on the concentration of the system, c (see Eq. (1.8)). Therefore, Eq. (1.32) still holds with the replacements

$$N \rightarrow N/g_c, \quad a \rightarrow \xi_c. \quad (4.1)$$

With the uniform concentration $c \propto N\rho_g/D$, Eq. (1.32) yields for the interpenetration depth

$$\delta \propto a \left[N^{2\nu} (\rho_g a^2)^{2(1-2\nu)} \left(\frac{a}{D} \right)^{1-\nu} \right]^{1/3(3\nu-1)} \quad (4.2)$$

for strongly compressed, semidilute brushes. Under melt conditions, the gyration radius in shear direction (lateral extension) of a chain is given by $R_{g,x}(0) \propto N^{1/2}a$. With the same transition to the blob picture [see Eq. (4.1)] we get

$$R_{g,x}(0) \propto \left(\frac{N}{g_c} \right)^{1/2} \xi_c \propto a \left[N^\nu \left(\frac{D}{\rho_g a^3} \right)^{2\nu-1} \right]^{1/2(3\nu-1)} \quad (4.3)$$

for semidilute brushes in linear response.

In the next step, we estimate the friction force per unit area (f_x/A) for Weissenberg numbers $W \leq 1$ by assuming Zimm dynamics in the blob[45]. Since the size of the blobs is the same in the whole bilayer, the knowledge of the interpenetration depth [see Eq. 4.2] allows to calculate the number of blobs in the overlap region. Since there are $c\delta/g_c$ blobs (per unit area) in the overlap region, each having a friction coefficient $\eta_s \xi_c$ (η_s the solvent viscosity), and a typical velocity is the shear rate multiplied by the distance between the walls, $\dot{\gamma}D$, we may write

$$\frac{f_x(\dot{\gamma})}{A} \propto \frac{c\delta}{g_c} \eta_s \xi_c \dot{\gamma} D \quad (W \leq 1). \quad (4.4)$$

With Eqs. (1.8) and (4.2) this leads to

$$f_x(\dot{\gamma}) \propto \left[N^{8\nu} (\rho_g a^2)^{2(1+\nu)} \left(\frac{a}{D} \right)^{4(\nu-1)} \right]^{1/3(3\nu-1)} \eta_s \dot{\gamma} A \quad (4.5)$$

in the linear response regime. This result is different from the original calculation by Klein[16], who obtains

$$f_x(\dot{\gamma}) \propto h \rho_g^{1/2} \left(\frac{h}{D} \right)^{2/3(3\nu-1)} \eta_s \dot{\gamma} A \quad (W \leq 1). \quad (4.6)$$

This expression can be transformed into

$$f_x(\dot{\gamma}) \propto \left[N^{9\nu-1} (\rho_g a^2)^{(7\nu-1)/2\nu} \left(\frac{a}{D} \right)^2 \right]^{1/3(3\nu-1)} \eta_s \dot{\gamma} A, \quad (4.7)$$

when the relation $h \propto aN(\rho_g a^2)^{(1-\nu)/2\nu}$ [81] is used. A comparison with Eq. (4.5) reveals an almost identical exponent for N , but different scaling-laws for ρ_g and D . We attribute these deviations to the fact that Klein starts out from

$$\delta \propto \rho_g^{-1/2} \left(\frac{h}{D} \right)^{1/3}, \quad (4.8)$$

which rather describes the interpenetration for weakly compressed, molten brushes, and to a different estimate of the number of blobs in the interpenetration zone. However, since we base the following scaling argument on the N -dependence of the shear force, Klein's approach would lead to minor differences.

We anticipate that thermal fluctuations allow the chains of a brush to exchange between the overlap region and deeper layers[106]. Hence, the shear stress should be sustained by more chains than only those that are in the overlap region at a given time. However, our description is based on the lateral chain extension averaged over the whole layer. This is formally equivalent to the assumption that all chains sustain the stress equally.

The critical shear rate follows from the definition of the Weissenberg number Eq. (1.58) with $W = 1$. Using $\rho_g = N_g/A$ with Eqs. [4.3] and (4.5), we find

$$\dot{\gamma}^* \propto \frac{k_B T}{\eta_s a^3} \left[N^{-19\nu} (\rho_g a^2)^{20\nu-13} \left(\frac{a}{D} \right)^{14\nu-11} \right]^{1/6(3\nu-1)}, \quad (4.9)$$

or, with $\nu \approx 0.588$, $\dot{\gamma}^* \propto N^{-2.44} \rho_g^{-0.27} D^{0.6}$. For the shear force at $W = 1$, [see Eq. (1.58)], we obtain

$$f_x(\dot{\gamma}^*) \approx \frac{N_g k_B T}{R_{g,x}(0)}. \quad (4.10)$$

From the Eqs. (4.3) and (4.10) one finds

$$f_x(\dot{\gamma}^*) \propto \frac{N_g k_B T}{a} \left[N^{-\nu} \left(\frac{\rho_g a^3}{D} \right)^{2\nu-1} \right]^{1/2(3\nu-1)}. \quad (4.11)$$

We now address the regime beyond linear response. At large shear rates, the chains

strongly stretch in the shear direction, such that $R_{g,x}(\dot{\gamma}) \propto N$. Now let us define the ratios for the chain extension, shear forces, and viscosities between the non-Newtonian response regime and static equilibrium. For the chain extension

$$q_\alpha \equiv \frac{R_{g,\alpha}^2(\dot{\gamma})}{R_{g,\alpha}^2(0)}, \quad (4.12)$$

with $\alpha = x$ (shear direction), or $\alpha = z$ (gradient direction) for shear forces

$$u \equiv \frac{f_x(\dot{\gamma})}{f_x(\dot{\gamma}^*)}; \quad (4.13)$$

and for the viscosity

$$s \equiv \frac{\eta_{xz}(\dot{\gamma})}{\eta_{xz}(0)}, \quad (4.14)$$

with $\eta_{xz}(0)$ the zero shear viscosity.

Since $f_x/A = \sigma_{xz}\dot{\gamma}$, one may write for the shear viscosity

$$s \propto \frac{f_x(\dot{\gamma})}{f_x(\dot{\gamma}^*)} W^{-1} \Rightarrow u \propto sW. \quad (4.15)$$

With Eq. (4.3) we obtain

$$q_x \propto N^{(2-5\nu)/(1-3\nu)} \quad (W > 1). \quad (4.16)$$

On the other hand, Eq. (4.9) yields

$$W \propto \dot{\gamma}^{*-1} \propto N^{19\nu/6(3\nu-1)}, \quad (4.17)$$

such that

$$q_x \propto W^{6(5\nu-2)/19\nu} \quad (W > 1). \quad (4.18)$$

For strongly stretched chains, we expect the shear force to be proportional to the total number of monomers ($\propto N_g N$) and the typical velocity, i.e.

$$f_x(\dot{\gamma}) \propto N_g N \dot{\gamma} D \propto N \quad (W > 1). \quad (4.19)$$

Hence, upon inserting Eqs. (4.11) and (4.19) into Eq. (4.13), one finds

$$u \propto N^{(2-7\nu)/2(1-3\nu)}, \quad (4.20)$$

for the regime beyond linear response. In combination with Eq. (4.17), this yields for shear forces

$$u \propto W^{3(7\nu-2)/19\nu} \quad (W > 1), \quad (4.21)$$

and with Eq. (4.15) for the viscosity

$$s \propto W^{-2(3-\nu)/19\nu}. \quad (4.22)$$

4.2.2 Rouse dynamics

So far we have described strongly compressed, semidilute brushes in the Zimm model (including hydrodynamic interactions). Let us assume that hydrodynamic interactions are fully screened and that the monomers obey Rouse dynamics instead of Zimm dynamics. This would correspond to the case of "dry" brushes.

In the following, we distinguish two cases, a molten brush, where in addition to hydrodynamic interactions also the excluded volume interactions are screened, and a semidilute brush consisting of excluded volume blobs as in Sec. 4.2.1.

For brushes without hydrodynamic interactions, the friction force is proportional to the number of monomers in the overlap region, the friction coefficient, ψ , and the typical shear velocity in the system, $\dot{\gamma}D$,

$$f_x(\dot{\gamma}) \propto c\delta\psi\dot{\gamma}DA \quad (W \leq 1). \quad (4.23)$$

Let us first consider molten brushes. In this regime, Eqs. (1.32) and (4.23) yield

$$f_x(\dot{\gamma}) \propto N^{5/3} \quad (W \leq 1). \quad (4.24)$$

Since $R_{g,x}(0) \propto N^{1/2}$ under melt conditions, we find with $R_{g,x}(\dot{\gamma}) \propto N$ and Eq. (1.58)

$$\dot{\gamma}^* \propto \frac{k_B T}{\psi a^2} N^{-13/6} \left(\frac{D}{a}\right)^{1/3}. \quad (4.25)$$

In the non-linear regime, this yields

$$q_x \propto N \propto W^{6/13} \quad (W > 1) \quad (4.26)$$

With $f_x^{\text{melt}}(\dot{\gamma}) \propto N$ at large shear rates and $f_x(\dot{\gamma}^*) \propto 1/R_{g,x}(0)$ [Eq. (1.58)], we find

$$u \propto N^{3/2} \propto W^{9/13} \quad (W > 1) \quad (4.27)$$

and for the viscosity

$$s \propto W^{-4/13}. \quad (4.28)$$

This result can be compared to the earlier predictions of the viscosity of the molten brushes[107]. In that study the brushes were under weak compression. This leads to the prediction for the shear viscosity $s \propto W^{1/2}$.

Now let us turn to the semidilute brushes with Rouse dynamics. Although this case

appears awkward from an experimental point of view, it can be compared to numerical approaches where hydrodynamic interactions are not taken into account, e.g. due to specific thermostat implementations (e.g. Langevin thermostat).

When the chains are swollen, the interpenetration length is given by Eq. (4.2). With Eq. (4.23), the shear force for dry, semidilute brushes in linear response scales as

$$f_x(\dot{\gamma}) \propto N^{(11\nu-3)/3(3\nu-1)} \quad (W \leq 1). \quad (4.29)$$

The critical shear rate follows from Eqs. (1.58) and (4.3), such that

$$\dot{\gamma}^* \propto \frac{k_B T}{\psi a^2} \left[N^{6-25\nu} (\rho_g a^2)^{7(2\nu-1)} \left(\frac{a}{D} \right)^{8\nu-5} \right]^{1/6(3\nu-1)}. \quad (4.30)$$

Beyond linear response this yields, together with Eq. (4.16),

$$q_x \propto W^{6(5\nu-2)/(25\nu-6)} \quad (W > 1) \quad (4.31)$$

for the lateral chain extension, and the scaling of u with W follows from Eqs. (4.20) and (4.30), such that

$$u \propto W^{3(7\nu-2)/(25\nu-6)} \quad (W > 1), \quad (4.32)$$

for the shear forces.

4.3 Computer simulations

In this section, we present data of computer simulations for two compressed, opposing polymer brushes under lateral steady-state motion of the adsorbing substrates. We compare systems with stars and without stars, i.e. Solvent C, D and Solvent B, which were defined in Chapter 2. We compare the simulation results with the theoretical predictions made above.

4.3.1 Density profiles and overlap region

Let us first analyse the structure of the system. An investigation of monomer and solvent density profiles (Fig. 4.1) reveals that solvent molecules accumulate at the substrates (seen also for a similar model[38]) and in the interface of the two brushes, even in static equilibrium in spite of the presence of stars. The brushes interpenetrate into each other. Solvent molecules are distributed in the system, even at the surfaces. The stars are located in the middle of the system between the brushes. Brushes under shear become more dense and squeeze solvent molecules into the interfacial region between the brushes (see Fig. 4.1 lower left plot). The stars become more compressed and are pushed out of the brush more significantly, such that the interpenetration between brushes and stars

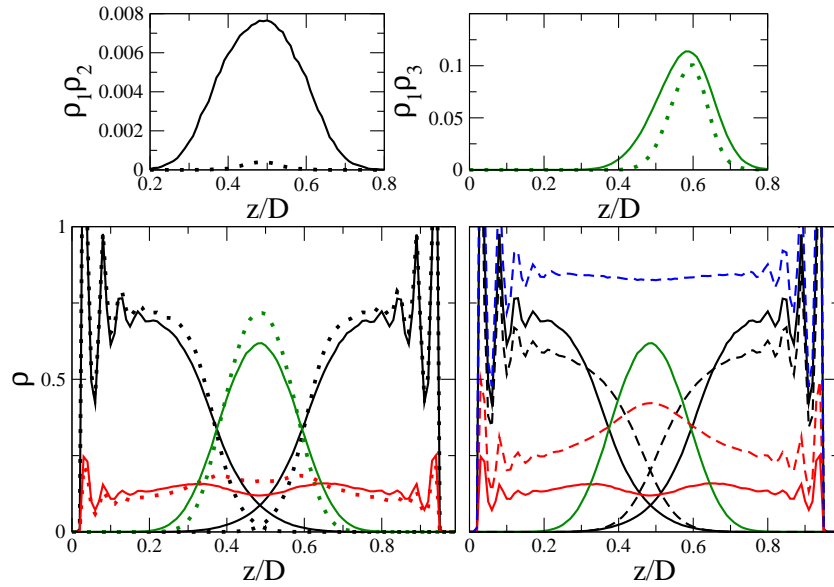


Figure 4.1: Monomer and solvent density profiles at distance $D = 17.5$ between grafting planes for chains of length $N = 30$. The grafting density is $\rho_g \approx 4.4\rho_g^*$ for all systems. Static equilibrium (firm lines) is compared to the steady shear conditions at our largest shear velocity, $v = 0.23$ (dotted lines). The dashed lines represent the Solvent B system. Black lines correspond to the brushes; green lines to stars of configuration $f = 30$, $N_{\text{mon}} = 5$; red lines to the solvent molecules. The panel above shows a plot of the overlap between the brushes (left) and between the top brush and stars (right), which can be quantified by the area under $\rho_1(z)\rho_2(z)$ and $\rho_1(z)\rho_3(z)$ correspondingly (see text). Both overlaps brush-brush and brush-star reveal Gaussian distributions. The lower panel shows density profiles of the brushes, solvent molecules, and stars. The left plot below shows a comparison between the sheared and unsheared systems of Solvent C, the right plot compares the Solvent B and Solvent C systems. The blue dashed line shows a sum of all components in the system.

reduces. The sum of the all components does not reveal significant differences, such that shear does not induce density fluctuations; the system keeps its low compressibility. While replacing the solvent molecules by stars the total density of the system remains the same. The systems without stars exhibit a larger brush thickness (see Fig. 4.1 lower right plot); the brushes in the presence of the stars are strongly deformed. The sum of all components reveal a flat density profile.

The interpenetration between the brushes can be quantified by an overlap integral[31, 37],

$$I_{\text{ov}}(\dot{\gamma}) \propto \int dz \rho_i(z)\rho_j(z), \quad (4.33)$$

where $\rho_i(z)$ and $\rho_j(z)$ are the density profiles of the component with $i = 1$ and $j = 2$ corresponding to the top and bottom brushes, $i = 1$ and $j = 3$ to the profiles of the top

brush and stars.

The upper plot of Fig. 4.1 shows the overlap between different components of the system characterized as defined in Eq. (4.33). It reveals, that the interpenetration between brushes with stars (Solvent C) is reduced compared to the star free case (Solvent B). Furthermore, we observe that, under sufficiently strong shear, the layer thickness decreases and this leads to a reduced interpenetration depth. The right upper plot shows the interpenetration between the stars and brushes. Similarly to the case of two brushes it has a Gaussian form.

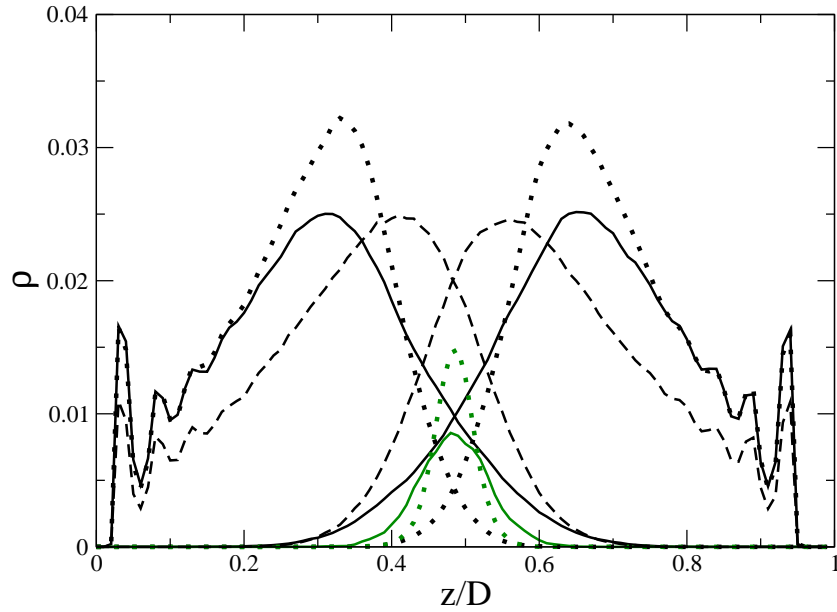


Figure 4.2: Distribution of brush ends and center monomer of stars at $D = 17.5$ between grafting planes for chain length $N = 30$. The grafting density is $\rho_g \approx 4.4\rho_g^*$. Black lines correspond to brushes, green lines to stars, dotted lines to steady shear motion, full lines to static equilibrium. The system without stars in static equilibrium is presented by dashed lines.

Figure 4.2 proves that brushes interpenetrate deeply into each other. The end-monomer distribution shows that chain ends of one brush interpenetrate deeply into the opposing brush. This effect decreases under shear. The interpenetration of the brushes still remains but is significantly decreased, the chains become more stretched, which can be concluded from the decrease of the maximum of the distributions. The stars hinder the interpenetration between the brushes. The distribution of center monomers becomes more narrow, stars are expelled out of the brushes similarly to the solvent molecules and concentrate in the interface of the bilayer.

The brushes and the stars deform each other significantly. The deformation of the stars was described in Chapter 3. Let us turn now to the deformation of the brushes. It can be

characterized by the analysis of the brush height around the center monomer of the stars, $H(r - r_m)$, with r_m is the position of the center monomer of the star. This is presented in Fig. 4.3. The brush height is lower around the center monomer. It continuously grows up to the level when the brush is not influenced by the presence of the stars. The deformation of the brushes decreases upon increasing softness of the stars. Under strong shear condition the brush around the star gets much weaker. The brush height becomes almost constant, the deformation is smoothed away, this leads on turn also to a strong deformation of the stars under shear, as we will see below.

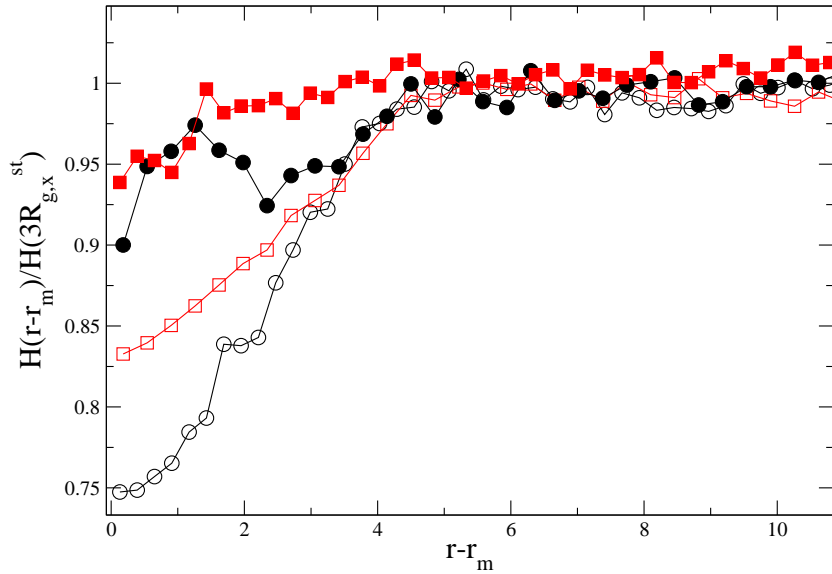


Figure 4.3: The brush height around the center monomer of a star. The brush height is normalized by its value, when the brush is not influenced by the presence of the stars (at $r - r_m = 3R_{g,x}^{st}$) for two different star configurations. The full symbols correspond to the steady shear, the empty symbols to static equilibrium. Black curves correspond to the star configuration $f = 30$, $N_{\text{mon}} = 5$, red lines to $f = 15$, $N_{\text{mon}} = 10$. The brushes are strongly deformed by the stars. Under shear the deformation is smoothed. The distance between the walls is $D = 12$, the grafting density is $\rho_g \approx 2.2\rho_g^*$, the chain length is $N = 30$.

Let us turn back to the interpenetration region between the brushes and forces acting in this region. The components are the brushes, stars and solvent molecules. Corresponding in the following to the indices "b", "so", "st". The forces acting between the different components, e.g. between brushes and solvent molecules, will be signatored by the index "b-so". A previous study[31] revealed that $I_{\text{ov}}(\dot{\gamma})$ is proportional to the number of binary interactions between monomers of different brushes, $N_{\text{int}}^{\text{b-b}}$, whereas the latter is proportional to the forces acting between the brushes in shear direction, $F_x^{\text{b-b}}$, i.e.

$$I_{\text{ov}}(\dot{\gamma}) \propto N_{\text{int}}^{\text{b-b}} \propto F_x^{\text{b-b}} \quad (4.34)$$

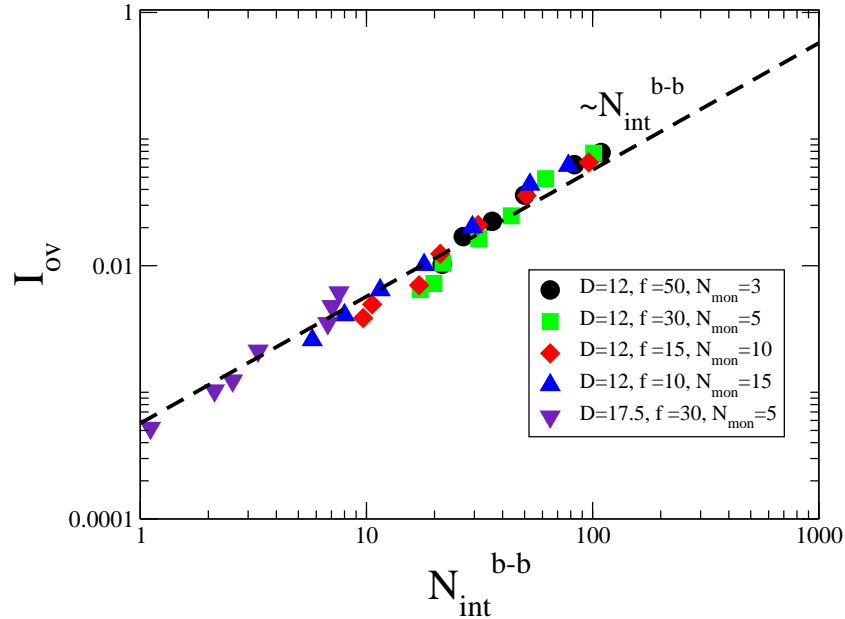


Figure 4.4: Overlap integral I_{ov} vs. number of binary interactions N_{int}^{b-b} . The full line represents the previously observed linear dependence for the star-free case[31]. All systems correspond to the solvent C.

In Fig. 4.4 the dependence of the overlap integral on the number of interactions between the brushes can be seen for the systems with stars. Stars decrease significantly the interpenetration between the brushes, but do not modify the proportionality given in Eq. (4.34).

Various numerical investigations[31–34, 36, 37] demonstrated shear thinning behavior. It was shown that this coincides with a reduced overlap between the grafted layers and that macroscopic transport properties, e.g. the shear viscosity, are correlated to $I_{ov}(\dot{\gamma})$.

While the overlap integral, in principle, may be measurable experimentally, we can straightforwardly count the number of binary inter-brush interactions or measure the forces acting between the brushes and other components of the system.

Figure 4.5 shows F_x^{b-b} as a function of shear rate for different star configurations and distances between the walls, D . The presence of stars decreases the force acting between the brushes, since the interpenetration decreases due to the fact that the stars are located in the middle of the system. Let us compare first the forces acting between the brushes for different star configurations. One can see (pronounced at the highest shear rate) that the softer the stars the quicker decreases the force between the brushes upon increase of the shear rate. Moreover, upon increase of the distances between the walls the force starts decreasing at higher shear rates. The same conclusion can be drawn when one compares the systems with and without stars, namely that the forces between the

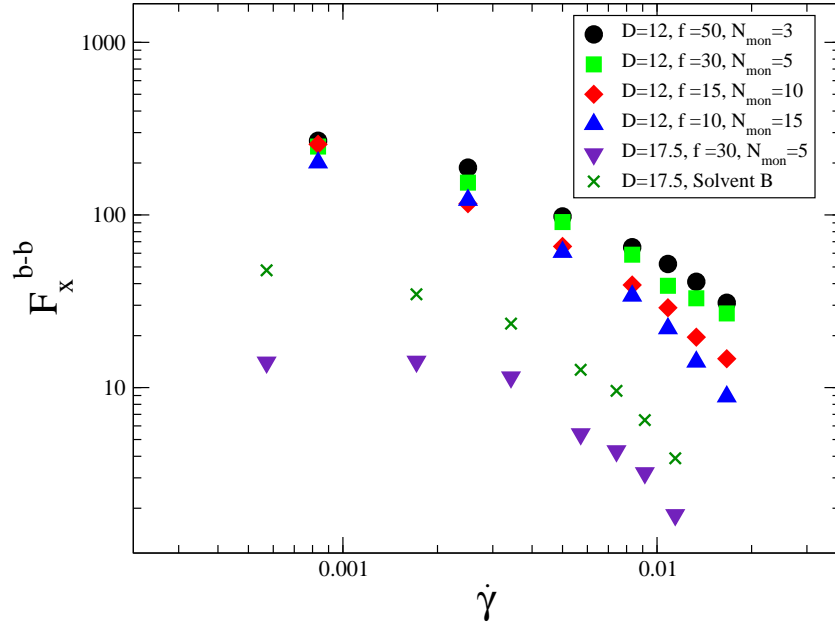


Figure 4.5: Forces acting between the brushes as a function of shear rate on a double-logarithmic scale. For the different considered systems, the force F_x^{b-b} varies over almost two orders of magnitude in static equilibrium. The presented systems, with the grafting density $\rho_g = 2.2\rho_g^*$, demonstrate different behaviors upon increase of the distance between the walls. The softer the star the quicker decreases the force acting between the brushes.

brushes in the case of the Solvent B start decreasing at lower shear rates than in the case of the Sovent C, when the half of the dimers is replaced by the stars.

In Fig. 4.6 the dependence of the forces acting between the brushes and stars on the shear rate is presented. It reveals that the increase of the distance between the substrates results in less interpenetration between the brushes and stars - the same effect, which is observed in the star-free case between the brushes. When the density of stars is kept constant, the systems with different star configurations demonstrate different responses to shear. The softer the star, the more interactions between stars and brushes occur. The interpenetration between them starts decreasing for smaller shear rates upon increasing the "softness" of stars.

The same law as in Eq. 4.34 can be observed for the interpenetration between the brushes and polymer stars. It demonstrates, for the overlap between the stars and the brushes, I_{b-st} , the number of binary interactions between them, N_{int}^{b-st} , and the forces in shear and in gradient direction between them F_α^{b-st} , with $\alpha = x$ or $\alpha = z$, respectively, the following law:

$$I_{b-st}(\dot{\gamma}) \propto N_{int}^{b-st} \propto F_\alpha^{b-st}. \quad (4.35)$$

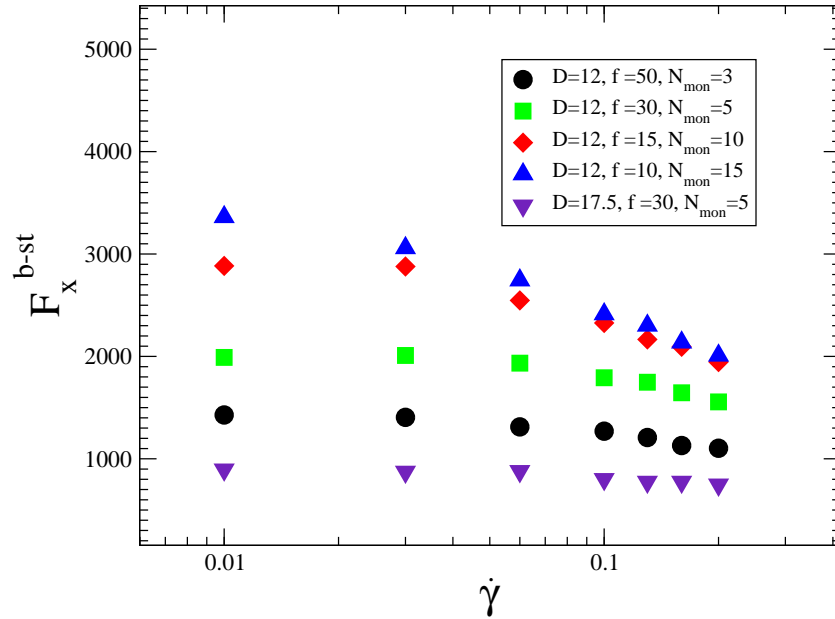


Figure 4.6: Semi-log plot of the forces, acting between the brushes and stars in shear direction ($F_x^{\text{b-st}}$) as a function of shear rate. With increasing distance, D , between the substrates the forces between brushes and stars decrease. Varying the "softness" of the stars via their functionality, f , and length of arms, N_{mon} , results in a different behavior. The shorter the length of the arms the less interaction occurs. The grafting density is $\rho_g = 2.2\rho_g^*$, the chain length, $N=30$

In Fig. 4.7 the last part of the relation (4.35) is demonstrated. The forces acting the stars and brushes are larger in the shear direction between, than in the gradient direction. One possible explanation may be that the brush interpenetrates through the layer of stars into the opposing brush, such that increasing the shear rate the brush has to leave first the opposing brush, which results also in a strong interaction with the stars in shear direction; upon further increase of the shear rate the brush starts leaving the layer of stars resulting in further decrease of the force. As can be seen, the forces in gradient direction decrease similarly to the forces in shear direction with increasing shear rate.

4.3.2 Kinetic friction coefficient

A different behavior of systems with and without stars can be observed for the kinetic friction coefficient, μ . We define μ as the ratio between shear and normal forces,

$$\mu(\dot{\gamma}) = \frac{f_x(\dot{\gamma})}{f_z(\dot{\gamma})}, \quad (4.36)$$

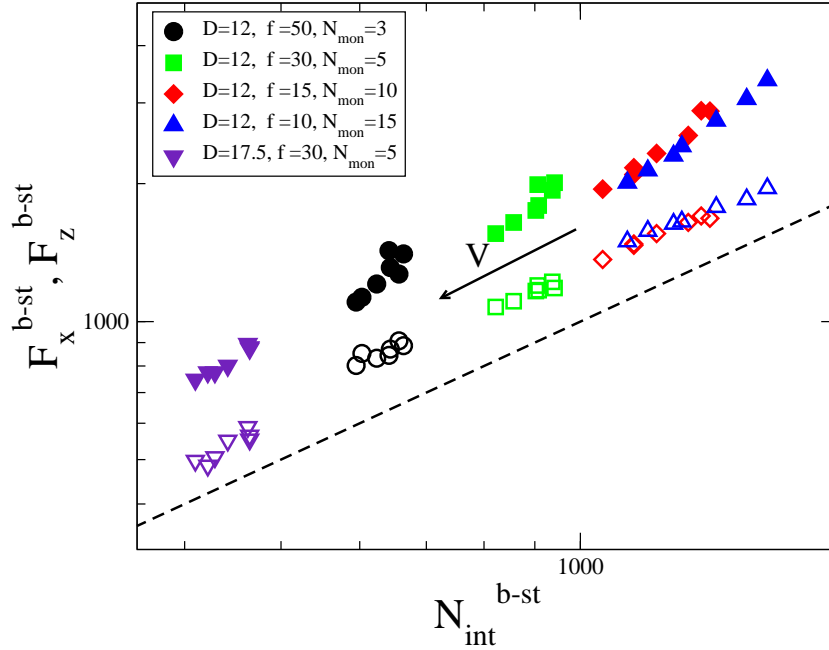


Figure 4.7: Forces in gradient and in shear direction F_{α}^{b-st} with $\alpha = x$ corresponding to shear direction (full symbols) and $\alpha = z$ gradient direction (empty symbols) as a function of number of interactions between brushes and stars N_{int}^{b-st} , demonstrating the relation (4.35). The systems are the same as in Fig. 4.6.

which we apply to the center-of-mass of the confining substrates to maintain constant v and D . We verified that our results are independent of whether we characterize the macroscopic response by measuring forces at the substrate or by calculating elements of the stress tensor, using the Irving-Kirkwood method[86] [see Eq. (2.25)].

All systems keep their low compressibility even under strong shear. Therefore, f_z remains almost independent of $\dot{\gamma}$, and only at our largest velocities we find (for some cases) a small increase of f_z by approximately 4%.

Upon increase of the shear rate and decrease of the distance between the walls while fixing the other parameters leads to an increase of the friction coefficient μ .

The dependence of μ on the shear rate $\dot{\gamma}$, where we vary the grafting density ρ_g between $\rho_g = 1.1\rho_g^*$ (when the brushes are in a slightly stretched regime) and $\rho_g = 4.4\rho_g^*$ (for highly stretched brushes), is presented in Fig. 4.8. It demonstrates that the increase of the grafting density at fixed D (such that the density of solvent decreases) results in higher friction. If one increases the length of chains, N , but keeps the density of the brush or the grafting density constant, leads in both cases to higher friction, too. This result is confirmed experimentally[108].

The solvent plays a crucial role in polymer-brush lubrication processes[32]. Effects of

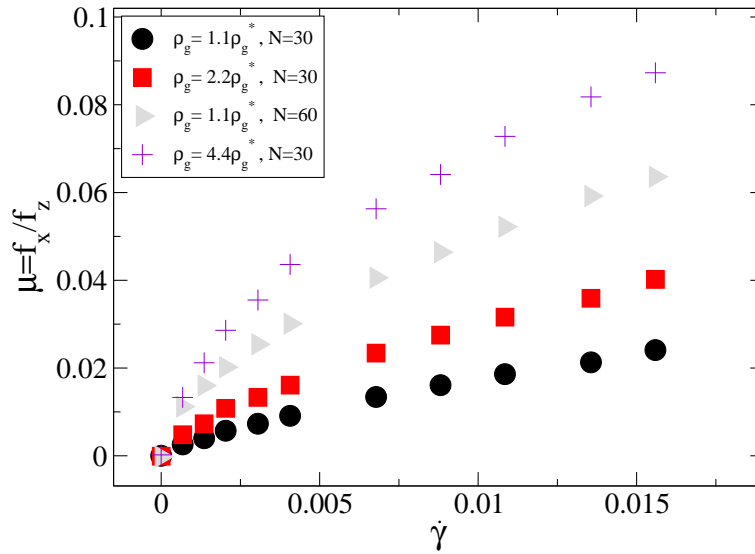


Figure 4.8: Kinetic friction μ as a function of the shear rate $\dot{\gamma}$. Increase of the grafting density ρ_g and of the chain length N leads to the increase of the friction coefficient. The distance between the walls is $D = 14.75$, Solvent C, the configuration of stars is $f = 30$ and $N_{\text{mon}} = 5$.

solvent are also in details analysed in Ref. [109]. The presence of explicit solvent leads to smaller values of μ . For solvent-free systems, μ decreases for larger grafting densities due to larger normal forces. Replacing a part of the solvent by stars leads effectively to an increase of the size of the solvent molecules.

Figure 4.9 shows the kinetic friction coefficient μ for systems of Solvent C and Solvent D. Increase of both size of stars and density of stars results in higher friction. This demonstrates that the bigger the solvent molecules or inclusions are and the more inclusions are in the system the higher the friction. The effect of mobile polymers on normal and shear forces between polymer brushes was investigated also experimentally[91] and in previous simulations[36] confirming these tendencies.

The whole picture is shown in Fig. 4.10, where the kinetic friction coefficient is presented for the solvent-free case (Solvent A), with dimers (Solvent B), and star molecules (Solvent C and Solvent D).

In Ref. [109] it was demonstrated, that an increase of the grafting density for the solvent-free cases leads to a decrease of friction. Experiments[108] confirm this effect.

Figure. 4.10 shows that replacing the solvent molecules by stars leads to a higher friction, which means, in other words, that all inclusions presented in experimental systems or in nature, i.e. disadsorbed chains, or any foreign chains, which can form either "soft" coils or "hard" globules depending on the chemical incompatibility with the brush, or proteins, or even dust or colloids, lead to higher friction.

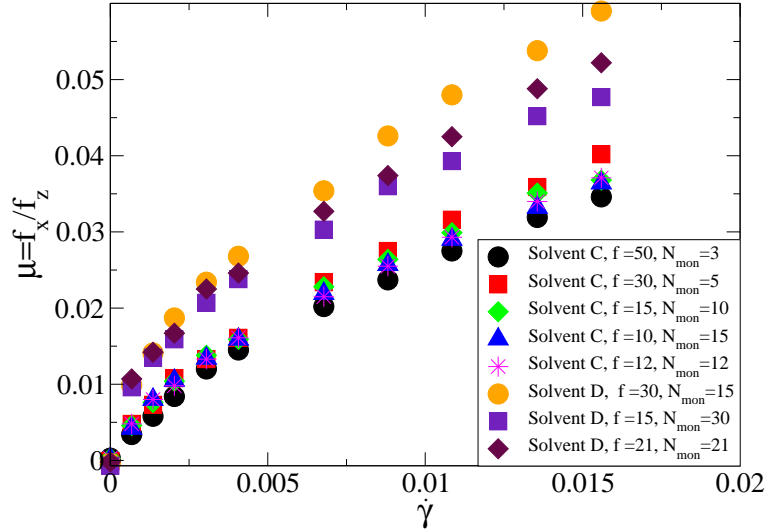


Figure 4.9: Comparison of the kinetic friction coefficient μ for different densities of stars of the systems Solvent C and Solvent D and different star configurations from small and colloid-like stars ($f = 50$, $N_{\text{mon}} = 3$) up to larger and softer ones ($f = 15$, $N_{\text{mon}} = 30$). The distance between the walls is $D=14.75$, the grafting density is $\rho_g = 2.2\rho_g^*$, the chain length is $N = 30$.

4.3.3 Structure of brushes

Now let us characterize the size of the brush in shear and gradient directions. The chain extension may be characterized by the radius of gyration [Eq. (1.2)] for different shear rates $\dot{\gamma}$. The gyration radius, R_g , as a function of shear rate, $\dot{\gamma}$, can be seen in Fig. (4.11). It reveals that systems of different composition, when we vary the grafting density, ρ_g , the chain length, N , the distance between the walls, D , functionality, f , and length of arms in stars, N_{mon} , also when we take the different solvent types from Solvent A to Solvent D, demonstrate different behaviors, similar to the behavior of forces between the brushes shown in Fig. 4.5. Some systems do not change their structure significantly under steady shear, other systems are in a crossover from the linear response regime to the non-Newtonian behavior, other systems exhibiting only non-Newtonian response. Often in computer simulations[60] one plots the gyration radius as a function of Weissenberg number, where the latter is defined via the relaxation time of a single chain in bulk of length N [see Eq. 1.56]. We will show below that another definition of the Weissenberg number is necessary.

Linear response should apply for small values of W , while non-linear effects are important for large values. However, the precise scale for W is somewhat arbitrary, because the bilayer has a broad spectrum of relaxation times and it is not clear which of them is best suited. Therefore, it is convenient to use an operational definition that sets

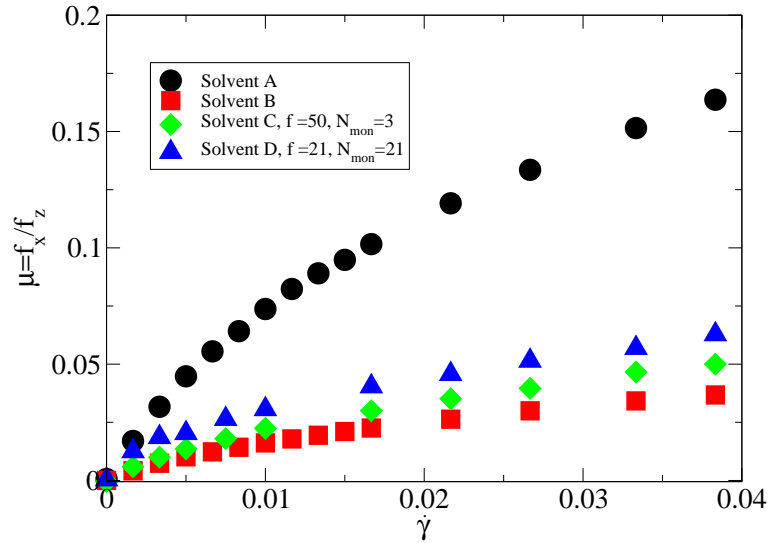


Figure 4.10: Comparison of kinetic friction coefficient μ as a function of shear rate, $\dot{\gamma}$, for four different investigated systems: Solvent A, Solvent B, Solvent C and Solvent D. The distance between the walls is $D = 12$, the grafting density is $\rho_g = 2.2\rho_g^*$, the chain length is $N = 30$. Systems with explicit solvent molecules demonstrate the smallest friction. Increase of the size of solvent molecules leads to an increase of friction.

the scale for W . Here, we determine $\dot{\gamma}^*$ operationally by plotting the raw data for q_x [see Eq. 4.12] against $\dot{\gamma}$ and shifting the data such that a master curve results. The fact that this procedure yields an (almost) perfect data collapse (Fig. 4.12) is a non-trivial result because the raw data strongly differ from each other. With this procedure we measure the critical shear rate, $\dot{\gamma}^*$, which is inversely proportional to the relaxation time, τ , of the bilayer.

Figure 4.12 shows that q_z decreases only weakly for $W > 1$. The chain extension in the gradient direction saturates at different values of W , depending on the chosen parameters (ρ_g , D , N , f , N_{mon}), due to the finite compressibility of the grafted layers. Moreover, Fig. 4.12 reveals that in gradient direction the relaxation time is different as compared to the shear direction.

In agreement with the early simulation studies[19], we find a pronounced stretching of the chains along the shear direction beyond the linear response regime. The data do not reach the limit of fully extended chains, where q_x should become constant. Rather we obtain a universal power-law,

$$q_x \propto W^\phi, \quad (4.37)$$

for Weissenberg numbers $W > 1$. The exponent $\phi \approx 0.5$ (indicated by straight lines) is in perfect agreement with the predictions (4.18) derived analytically in Sec. 4.2.1 for semidilute brushes with Zimm dynamics. For $\nu = 0.588$ the predicted exponent is equal

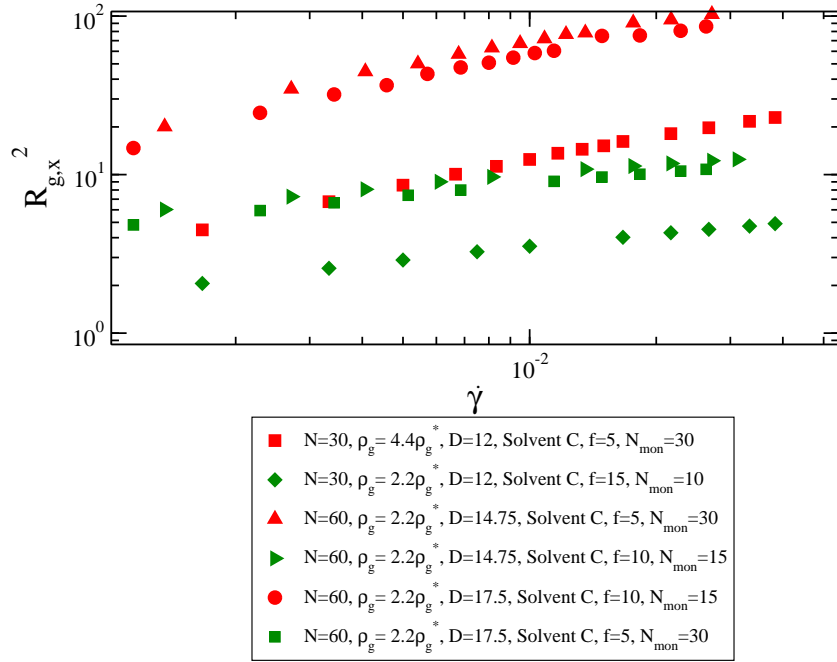


Figure 4.11: Log-log plot of the gyration radius squared R_g^2 of brushes in shear direction. Selected simulated systems, which have different distances between the substrates D , chain lengths N , grafting densities ρ_g , star configurations, with solvent demonstrate different behavior.

to $6(5\nu - 2)/19\nu \approx 0.5$.

Analysis of the static equilibrium properties shows that the lateral chain extension decreases upon increasing grafting density[109]. The opposite behavior is observed for the direction perpendicular to the surfaces. As expected, the brush thickness decreases under compression.

Larger values of $\dot{\gamma}^*$ are obtained for solvent-free systems compared to systems with explicit solvent, which indicates that the latter leave linear response earlier due to the additional monomer-solvent friction. A similar observation can be made for the surface separation. With decreasing compression, i.e. larger values of D , we systematically find larger critical shear rates. The presence of stars influences the relaxation times. Increase of the softness of stars leads to an increase of the gyration radius in both gradient and shear directions, and the brushes become effectively more compressed. The critical shear rate is slightly increased due to the presence of the stars comparing systems with and without stars at fixed grafting density and D . The dependence of the relaxation time on the star configuration, i.e. its functionality and the length of the arms, $\tau(f, N_{\text{mon}})$, is rather complex. The critical shear rate $\dot{\gamma}^*$ is still dominated by the brushes since the relaxation time of the arms in the stars (and of the star as whole) is smaller than of the

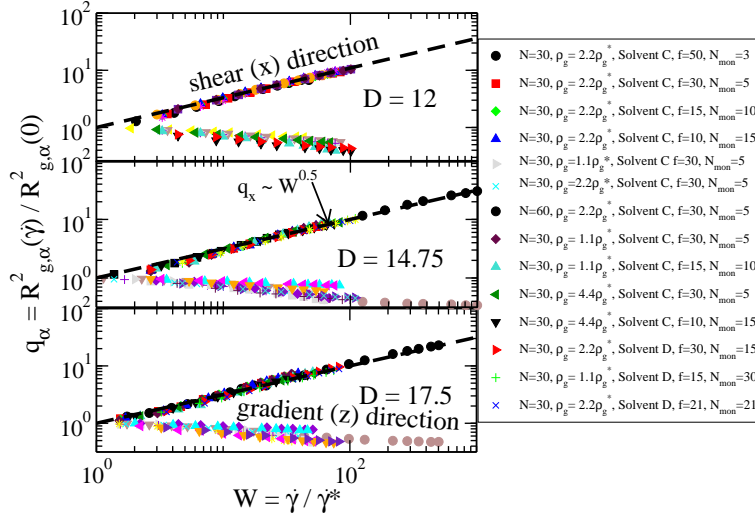


Figure 4.12: Double-logarithmic scaling plot for the chain extension in shear (x) and gradient (z) directions as a function of the Weissenberg number for $D = 12$, $D = 14.75$, and $D = 17.5$ (from above). The legend is shown for $D = 17.5$. Similarly, different star configurations, chain lengths, N , types of Solvent are presented for $D = 12$ and $D = 17.5$. Systems without solvent molecules are not deformed for $W \leq 1$ (not presented here, see Ref. [109]). Upon increasing W , the grafted layers shrink slightly and remain at constant height for larger shear rates. The chains stretch in shear direction, following a universal power-law (indicated by straight lines). Independently of the type of solvent (A, B, C or D) data for different values of D can be brought onto the same master curve (not shown).

brush due to the fact, that the length of arms in the stars is smaller than the length of the chains in the brush ($N_{\text{mon}} < N$).

The force that drives the system out of the linear-response regime increases with compression. This observation agrees with previous simulations[30] and experiments[18]. Increasing the chain length at fixed D and grafting density leads to a larger frictional force per chain. Moreover, larger chains need more time to relax. Systems with $N = 60$ thus leave the regime of linear response earlier than those with $N = 30$.

Interestingly, the structural response in shear direction is universal, independent of whether the solvent is explicitly included or not (when the density of the systems is not the same), and whether stars are included or not. The first conclusion is correlated with the fact that the DPD thermostat accounts for hydrodynamic correlations, at least at sufficiently large polymer concentrations. The second fact demonstrates universal behavior independently of the size of the solvent molecules or inclusions, provided they are small compared to the grafted chains, even though the interpenetration between the brushes is strongly influenced.

Finally, we point out that the same results are obtained when we define q_α via the mean

square end-to-end distance instead of using $R_{g,\alpha}^2$. Both quantities follow the same universal behavior.

4.3.4 Structure of stars

In this section we will analyse the behavior of stars in shear direction. For the case of sheared stars in the bulk [60] it is possible to produce scaling plots of the gyration radius in shear direction as a function of the Weissenberg number which is defined by the relaxation time of a single arm. However, due to the fact that the arms are connected to the center monomer of the star the relaxation times of each arm is influenced by the presence of the neighbor chains. The relaxation time of each star will strongly depend on the functionality of the star, f . In the following, we will demonstrate that the response of the stars on the shear not only strongly depends on the molecular parameters (f and N_{mon}), but also on the external environment, i.e. on the structure of the brushes.

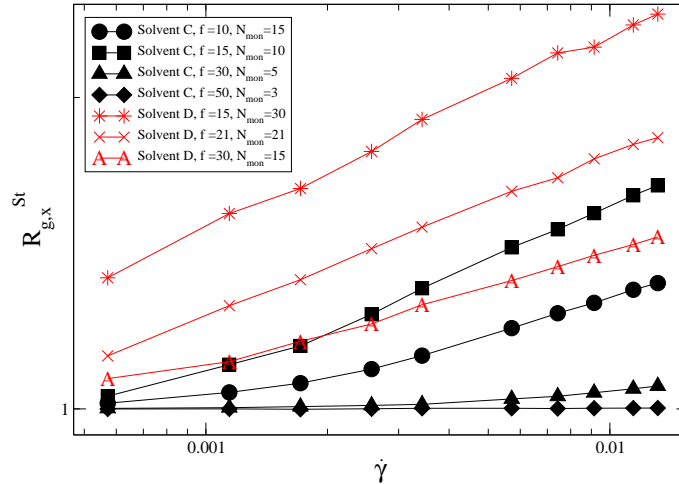


Figure 4.13: Gyration radius of stars R_g vs. shear rate $\dot{\gamma}$ for different star configurations (from small and colloid-like with $f = 50$ and $N_{\text{mon}} = 3$ increasing the size and softness of the stars up to $f = 15$ and $N_{\text{mon}} = 30$). The grafting density is $\rho_g = 2.2\rho_g^*$, chain length of brushes, $N = 30$, and distance between the substrates, $D = 17.5$. Different stars demonstrate different type of behavior from constant to power-law. The power-law seems to depend on the density of stars in the system (compare System C and System D).

In Fig. 4.13 one can see the dependence of the gyration radius on the shear rate. The strongest response shows the star configuration with the longest arms, $N_{\text{mon}} = 30$. Decreasing the length of arms while keeping the density of stars constant leads to a weaker response, as expected. For large shear rates the system with lower density of stars (Solvent C) can be more deformed in shear direction in comparison to systems, where the stars are packed denser (Solvent D).

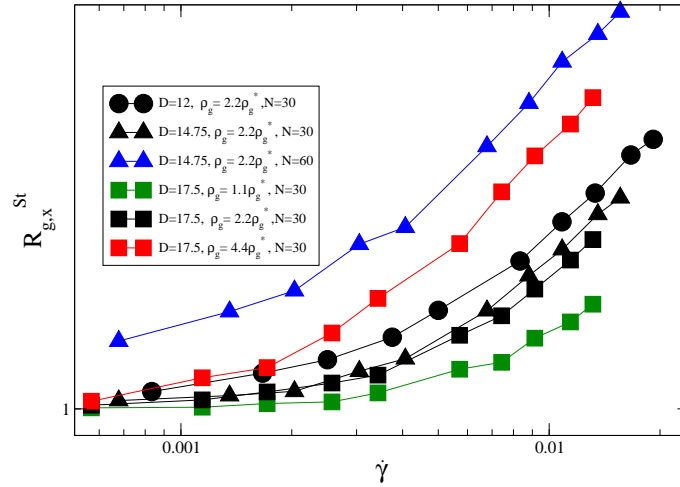


Figure 4.14: Gyration radius of stars R_g of configuration $f = 30$, $N_{\text{mon}} = 5$ vs. shear rate $\dot{\gamma}$ for different chain lengths ($N = 30$ and $N = 60$) and distances between substrates D . The grafting density is kept constant, $\rho_g = 2.2\rho_g^*$. The larger the distance between walls the less deformed the stars. The increase of the chain length leads to stronger response of the stars.

Figure 4.14 shows the dependence of the gyration radius of colloid-like stars ($f = 30$, $N_{\text{mon}} = 5$) for different chain lengths, N , and distances between the substrates, D , on $\dot{\gamma}$. Keeping the grafting density constant while increasing the chain length one observes stronger deformation of the stars. Stars have less freedom due to the stronger interpenetration between the brushes. In case of longer chains, the brushes leave the linear response regime at lower shear rates[109], which in turn influences the behavior of the stars as well.

Figure 4.15 presents the response of stars on steady shear for rather "soft" stars ($f = 15$, $N_{\text{mon}} = 10$) for different grafting densities of the brush. Since stars under high compression are already strongly deformed and shear leads to further deformation, a situation, when the gyration radius does not depend on the shear rate anymore, can be achieved. For small shear rates an increase of the grafting density leads to an increase of the stars' gyration radius in shear direction. Further increase of the shear rate may lead to the saturation of the stars' response (as can be seen in the case of the highest investigated grafting density, $\rho_g = 4.4\rho_g^*$, when the gyration radius approaches a plateau behavior).

The properties of the surfaces can be tuned easily by the polymer brushes. By varying the grafting density or chain length, the critical shear rate $\dot{\gamma}^*$ can be modified. Adding stars of functionality f and length of arms N_{mon} leads to a modification of the characteristic relaxation time (Eq. [4.9], which results in a modification of the gyration

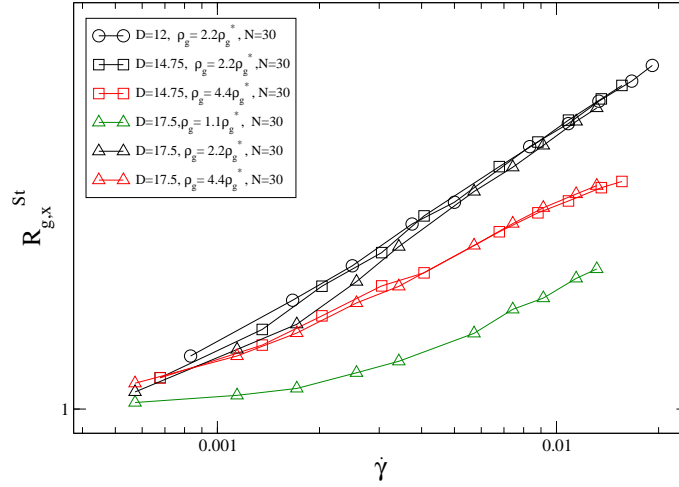


Figure 4.15: Gyration radius of stars of configuration $f = 15$, $N_{\text{mon}} = 10$ vs. shear rate for different grafting densities. The distance between substrates is $D=17.5$, chain length $N = 30$. For small shear rates the higher the grafting density of brushes the more deformed is the star in shear direction. For large shear rates, due to the incompressibility of stars, this behavior is modified.

radius of the stars. It turns out, that the relaxation time of stars crucially depends not only on the functionality and arm length, but also on the total density of stars, ρ_{st} , and, moreover on the molecular parameters of the brush, i.e. it depends on ρ_g , N , f , N_{mon} , ρ_{st} .

4.3.5 Viscosity and shear forces

To perform scaling plots for the transport properties, it is not sufficient to know the critical shear rate. For instance, to plot the ratio (4.14), where $\eta_{xz}(\dot{\gamma})$ represents the shear viscosity, we need $\eta_{xz}(0)$ for each examined system. In order to compute the (collective) zero-shear viscosity we have to perform simulations in the linear response regime at small Weissenberg numbers and this is related to a bad signal-to-noise ratio. However, in principle we can calculate $\eta_{xz}(0)$ from the measured shear forces for $W < 1$. In the linear response regime, the Weissenberg number may be expressed via the acquired energy per chain [see Eq. (1.58)]; the critical shear rate can be found from the requirement that the acquired energy is comparable to $k_B T$, i.e. when W is of order unity. The shear force is proportional to $\dot{\gamma}$ in linear response. With the zero-shear viscosity

$$\eta_{xz}(0) = \frac{f_x(\dot{\gamma})}{A\dot{\gamma}}, \quad (W \leq 1), \quad (4.38)$$

one thus may write

$$\dot{\gamma}^* \approx \frac{\rho_g k_B T}{\eta_{xz}(0) R_{g,x}(0)}, \quad (4.39)$$

where we have used $\rho_g = N_g/A$.

Equation (4.39) provides the possibility to compute $\eta_{xz}(0)$ for a given critical shear rate up to a (constant) numerical factor. Unfortunately, when plotting the ratio s [Eq. (4.14)], we find strong statistical fluctuations. Therefore, we use a different way of presentation by shifting the data along the ordinate to obtain an estimate for the zero-shear viscosity. Figure 4.16 shows the viscosity η_{xz} as a function of Weissenberg number $W = \dot{\gamma}/\dot{\gamma}^*$, where $\dot{\gamma}^*$ is taken from the scaling plot of gyration radius (Fig. 4.12).

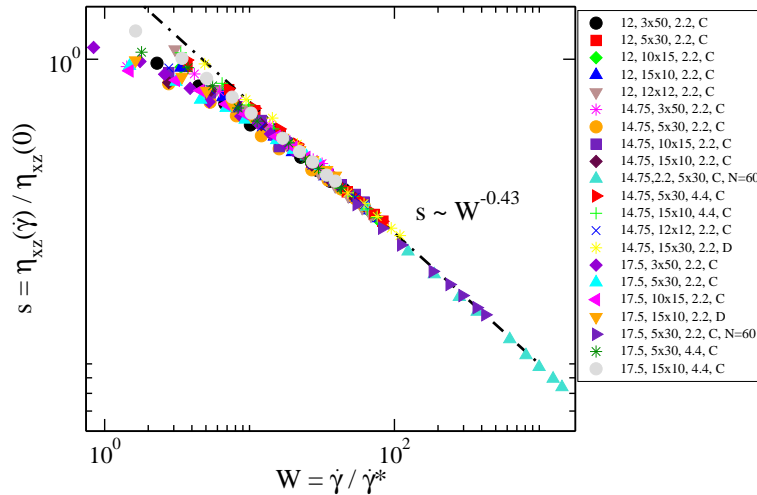


Figure 4.16: Double-logarithmic scaling plot for the shear viscosity as a function of the Weissenberg number. Similarly to Fig. 4.12 we show systems with stars of Solvent B, C, and D of grafting density $\rho_g \geq 2.2\rho_g^*$, the chain length is $N = 30$ (if not mentioned differently in legend), star configurations. The first number in the legend corresponds to the distance between the walls, D , the second number to the length of arms in the stars, N_{mon} , the third to the functionality of the stars, f , the fourth to the grafting density divided by the critical grafting density, ρ_g/ρ_g^* , the last letter corresponds to the type of solvent. The normalization constant, $\eta_{xz}(0)$, follows from shifting the data along the ordinate, such that $s \rightarrow 1$ for $W \ll 1$. The straight line corresponds to the analytically derived relation, $s \approx W^{-0.43}$ for $\nu = 0.588$ [see Eq. (4.22)]. All data can be mapped onto each other.

Systems without explicit solvent molecules (Solvent A), with solvent molecules as dimers (Solvent B) and with polymer stars (Solvent C and Solvent D) can be mapped onto each other. This again is a non-trivial result, which indicates a strong correlation between the deformation of chains and the macroscopic response. Beyond linear response the data follow a power-law,

$$s \propto W^\zeta \quad (W > 1). \quad (4.40)$$

The exponent $\zeta = -0.43$ (indicated by a straight line) is derived analytically [Eq. (4.22)] in Section 4.2.1.

The values for $\eta_{xz}(0)$ used in Fig. 4.16 were cross-checked with [Eq. (4.39)] for all simulated systems[109]. However, the data reveal strong fluctuations, which explains why it is almost impossible to produce a successful scaling plot for s from the direct calculation of $\eta_{xz}(0)$.

Polymer brushes demonstrate a universal power-law behavior in the non-linear response regime independently of the grafting density, distance between the substrates and chain length. In case of solutions of polymer stars the viscosity demonstrates different power-laws depending on the concentration of stars[110]. In our simulations of a mixture between polymer brushes and stars we observe deviations from the universal behavior when the brushes are not dominating the characteristic relaxation time of the system and and for a larger density of stars.

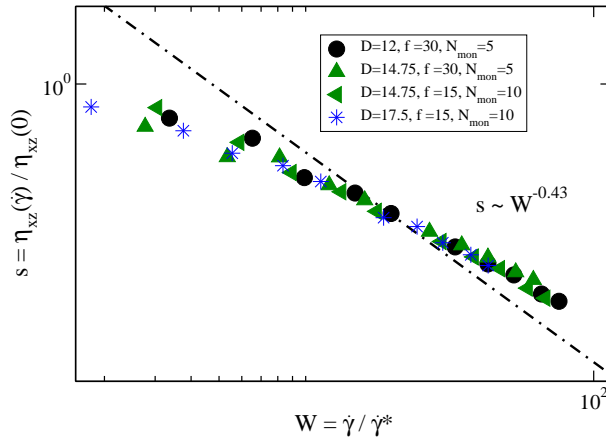


Figure 4.17: Shear viscosity as a function of Weissenberg number W , grafting density $\rho_g = 1.1\rho_g^*$, chain length $N=30$, Solvent C, density of stars $\rho_{st} \simeq 0.22$, when the stars lead to deviations from the predicted behavior $s \approx W^{0.43}$ (plotted as a line).

Figure 4.17 indicates that for systems of grafting density $\rho_g = 1.1\rho_g^*$ the presence of stars (of the density $\rho_{st} \simeq 0.22$) leads to a smaller exponent of the power-law. Computer simulations of an equivalent system of a solution of polymer stars without brushes reveal a power-law with an exponent $s \approx W^{-0.35}$ [110]. It indicates that inclusions might strongly influence the rheological properties of such complex systems.

Plotting the shear viscosity always reveals strong fluctuations at small shear rates. A somewhat clearer picture is obtained from the analysis of the shear force. Here, we measure $f_x(\dot{\gamma})$ at the substrates.

Figure 4.18 shows the ratio (4.13) as a function of W for all considered parameter combinations. The data collapse is even better than for the viscosity. As expected, u

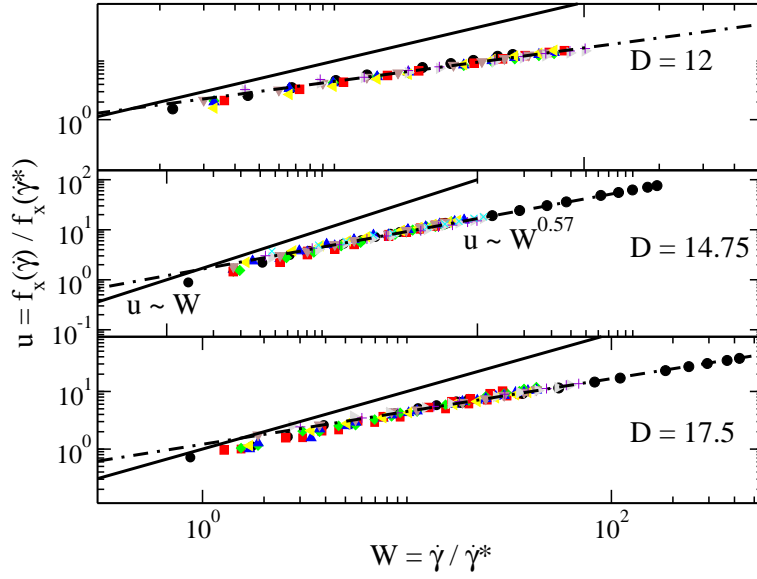


Figure 4.18: Double-logarithmic scaling plot for the shear force as a function of the Weissenberg number. Data is shown for two chain lengths, different surface coverage at distances $D = 12$, $D = 14.75$, and $D = 17.5$ between grafting planes, also different star configurations and different densities of stars (Solvent C and Solvent D). The same systems are presented as in Fig. 4.12. The normalization constant, $f_x(\dot{\gamma}^*)$, is obtained by shifting the data along the ordinate such that $u = 1$ for $W = 1$.

scales linearly with W for $W \leq 1$. Beyond linear response we obtain a power-law,

$$u \propto W^\kappa \quad (W > 1). \quad (4.41)$$

The dashed-dotted lines represent an exponent of $\kappa = 1 + \zeta = 0.57$, which follows from Eq. (4.15).

The values for $f_x(\dot{\gamma}^*)$ are obtained by shifting the data along the ordinate, such that $u(W = 1) = 1$. For the same reason as before, we do not get a satisfying scaling plot when using the relation Eq. (4.10).

We emphasize that we observe deviations between shear forces at the critical shear rates and Eq. (4.11) due to a dependence of the effective solvent viscosity, η_s , and monomer size, a , on the variation of compression and molecular parameters, because η_s and a depend on solvent and monomer density, hence implicitly on N , ρ_g , and D [109].

In conclusion, it is possible to describe systems of Solvent A, B, C and D on the basis of the same analytical concept. For this purpose we extract a characteristic time scale and the related length scale, which determine the response of a given system to shear. We suggest a method to obtain the time scale, where we assume that the mean extension of a grafted chain in shear direction represents a relevant length scale.

We expect deviations from our approach for weaker compression, when the distance between the grafting planes exceeds h , such that the assumption of a uniform monomer concentration is no longer valid. This regime was considered in Ref. [111] for molten brushes, where a disentanglement instability is predicted for a critical shear rate. This points in the same direction as the shear thinning we observe. It is to be noted that extrapolating from the strong to the weak overlap regime reveals a minimum in the interpenetration depth[109].

The above results are built on the chain deformation averaged over the entire layer. The critical shear rate we obtained does not correspond to any simple characteristic frequency. As a matter of fact, the structure of the sheared layer is more complex than reflected by the averaged deformations. Chain deformation takes place in the interface and is subsequently transported deeper into the layer by longitudinal chain end diffusion, which leads to chain end exchange between the interface and the bulk of the layers. Because the lateral deformation relaxes in the same time, deformed chains are hardly found far away from the interface. Though chains that reside temporarily rather than permanently in the interface are less deformed and chains outside the interface are deformed to some extent as well, chain end exchange does not distribute the chain deformation evenly across the layer.

The exponents for the non-linear regime predicted by both theories are very close. Simulation results could hardly discriminate between them.

For much longer chains, each grafted chain laterally wiggles around many others. Our theory describes a non-entangled central sublayer (comprising the interface) embedded into a gel-like elastic layer. A slightly different approach is needed when the interface is wide enough to be entangled itself. In spite of that, the entanglements between two opposing brushes are not crucial for our theory. Our approach predicts the power-law behavior in the non-Newtonian regime. For large Weissenberg numbers, here, chains must disentangle or break.

4.3.6 Comparison to experiment and other numerical approaches

Experimental limitations prevent the exploration of equivalently large compressions and shear rates as they can be studied in simulations. However, some experimental data that reach the non-Newtonian regime have become available. Schorr *et al.* recently measured shear forces in bilayers of polystyrene brushes on mica with the Surfaces Forces Apparatus (SFA)[18]. In toluene (good solvent), the authors observe linear response over a wide range of compressions and shear rates. However, at large compression ($2h/D \approx 4.6$) they find a sublinear increase of the shear force with sliding velocity. Interestingly, the experimental data is comparable with Eq. (4.21) [or Eq. (4.41)], as can be seen from Fig. 4.19. Identifying the critical shear rate and $f_x(\dot{\gamma}^*)$ via the crossover from linear to non-Newtonian behavior, we can compare the SFA data to our results at

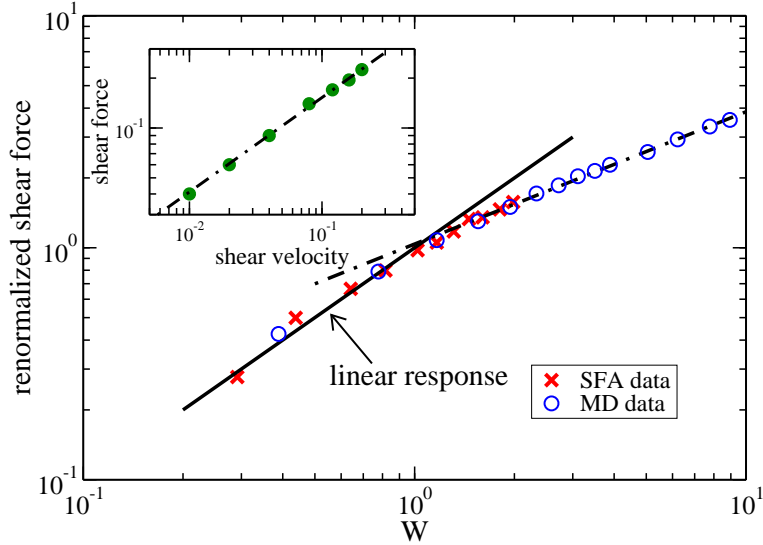


Figure 4.19: SFA data from PS/PVP [25/4]k in toluene at $T = 32^\circ\text{C}$ (taken from Ref. [18]). Shear force and velocity have been scaled by the same procedure as our simulation data [$D = 14.75$, $N = 60$, $\rho_g \approx 1.1\rho_g^*(N = 30)$, solvent-free] using $f_x(\dot{\gamma}^*) \approx 88\mu\text{N}$ and $\dot{\gamma}^* \approx 16.8/\text{s}$. Both experiment and simulation find a linear increase of the shear force for $W \leq 1$ and are in agreement with Eq. (4.21) in the non-Newtonian regime. The inset shows data[18] (in LJ units) from Brownian dynamics simulations, which agree nicely with the predicted power-law of Eq. (4.21) (dash-dotted line).

similar compression and chain length. For this purpose we use a solvent-free system with $D = 14.75$, $N = 60$, and $\rho_g \approx 1.1\rho_g^*(N = 30)$, corresponding to a compression of $2h/D \approx 4.1$ [81].

In the same study, Schorr *et al.* performed Brownian dynamics simulations using a Brinkman type equation to describe the solvent flow. They observe shear thinning at their largest compression ($2h/D \approx 7.4$) over the entire range of investigated shear rates. As shown in the inset of Fig. 4.19, also this data follows the scaling-law predicted by Eq. (4.21), despite the different approach to treat solvent effects.

Goujon *et al.*[35] recently investigated sheared polymer brushes with an off-lattice bead-spring model by means of MD simulations using a DPD thermostat with larger intrinsic friction. The length of the grafted polymers ($N = 20$) was somewhat smaller than considered here.

More importantly their study differs from ours in the way solvent molecules are incorporated. While our simulations are performed at constant particle number, Goujon *et al.* operate in the grand-canonical ensemble, allowing the number of solvent particles to fluctuate. This procedure guarantees a constant normal pressure for all shear rates. However, our numerical data indicates that the normal stress changes very weakly with

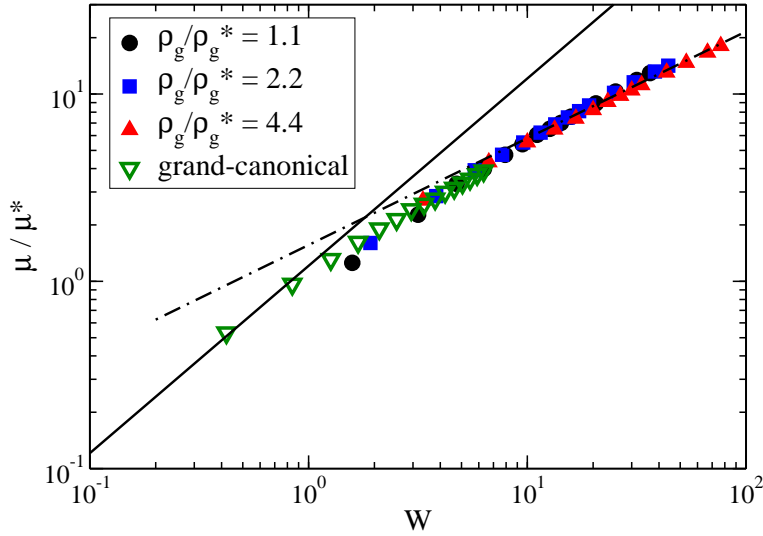


Figure 4.20: Renormalized kinetic friction coefficient (see text) as a function of the Weissenberg number. Results of grand-canonical MD simulations[112] are included. One can see a crossover from the linear behavior (solid line), $W \leq 1$, to the non-Newtonian regime $W > 1$. We find a reasonable agreement to the exponent suggested by Eq. (4.21) (dash-dotted line) beyond linear response. The distance between the walls is $D = 14.75$, Solvent C, the configuration of stars is $f = 30$ and $N_{\text{mon}} = 5$.

shear rate.

On the other hand, a grand-canonical solvent treatment might bear the risk of suppressing some hydrodynamic correlations. Also this effect seems negligible, as can be seen from Fig. 4.20, where we compare our data for the friction coefficient to the results of Goujon[112]. Since f_z is virtually constant, the dependence of the friction coefficient and f_x on W must be similar. We find that both numerical approaches reveal the same universal behavior, which is in good agreement with Eq. (4.21). The data superimposes when the kinetic friction coefficient is normalized by $\mu^* = \mu(W = 1)$ to obtain a scaling plot.

In conclusion, we find the same universal macroscopic response in numerical simulations despite very different approaches to incorporate solvent-effects, including the implicit treatment using a DPD thermostat or the self-consistent solution of the Brinkman equation. Approaches with explicit solvent molecules in different thermodynamic ensembles provide the same general picture. All these methods seem equivalently valid for steady-shear simulations of strongly compressed brushes, providing hydrodynamic correlations on the relevant length scales.

To the best of our knowledge, there is only one study[33] that reported a power-law behavior of the chain extension beyond linear response. In this investigation a Langevin

thermostat without explicit solvent molecules is used; an approach widely used in the past (see, e.g. Refs. [19, 21, 26, 30, 31, 33, 34, 37]). However, the Langevin thermostat cannot account for hydrodynamic correlations, because it does not apply random and dissipative forces in a pair-wise form[113]. In this case, the response to shear should be described by our scaling theory for semidilute, dry brushes. The previous study reported an exponent of $\phi \approx 0.6$, which is slightly smaller than our predicted value, 0.65.

Chapter 5

Non-stationary shear

5.1 Introduction

The results presented in the previous Chapter dealt with the stationary sliding of two opposing surfaces. In this section we present the results concerning the transient behavior of the system during shear inversion, when we start from a steady state configuration and change the shear direction. In order to better understand these complex systems it is necessary to investigate the transient dynamics from one configuration to another. For instance, most of the experiments are performed under oscillatory shear conditions, when shear inversion is performed several times. The shear and normal forces can be measured directly. The authors of these measurements report an increase of the normal forces[15, 91] with increasing frequency of the oscillatory shear or during shear inversion and an overshooting of the shear forces[92, 108]. This can be applied also for the onset of motion, when a starting configuration from static equilibrium is taken. These effects depend strongly on the solvent conditions[92]. However, except Ref. [33], there is no detailed analysis of the interplay between the static equilibrium and steady shear properties and the behavior during the crossover from one state to the other. The vast majority of investigations dealt with the effects of the waiting time[108] after which shear is performed and explained an increase of the friction coefficient and overshooting of the shear force with increasing waiting time through the presence of entanglements. Previous numerical investigations[33] were done using the Langevin thermostat, which does not take into account hydrodynamic interactions and without explicit solvent molecules, which might be crucial in non-equilibrium simulations. In our study, we investigate the systems under good solvent conditions with explicit solvent molecules. We take rather short chains and vary the grafting densities and composition of the system (including stars). We intend to understand the behavior of the shear and normal forces via an analysis of their components and characterize the structure of the system, i.e. by interpenetration between the brushes, gyration radius of the chains and brush height.

Moreover, the influence of the stars and their structure will be discussed.

5.2 Shear inversion

The shear inversion is started from a steady state configuration and performed during a finite time t_{turn} after which the final velocity in the opposite direction is reached. This time t_{turn} is small compared to the relaxation time of the bilayer. A velocity protocol for the walls is presented in Fig. 5.1.

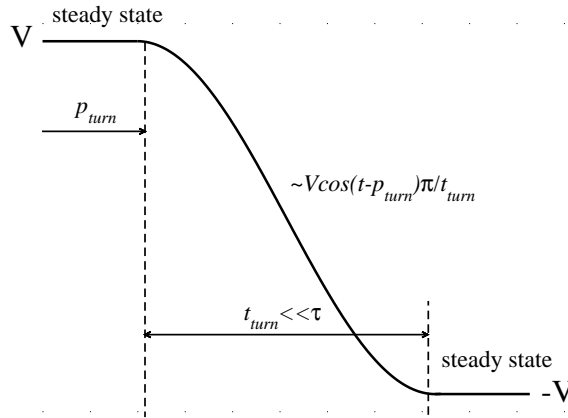


Figure 5.1: Shear protocol of the walls during shear inversion. The turn time is much shorter than the relaxation time of the bilayer, $t_{\text{turn}} \ll \tau$.

In contrast with the previous simulations we do not perform a strictly instantaneous inversion of the shear, as it has been done in Ref. [33] (a step function shear protocol). Instead we use a continuous change of the shear direction and imply a smooth shear protocol

$$V = V \cos \frac{(t - p_{\text{turn}})\pi}{t_{\text{turn}}} \quad (5.1)$$

where V is the shear velocity. p_{turn} is the time, when shear inversion is started, $t_{\text{turn}} + p_{\text{turn}}$ when the inversion is finished.

First, let us analyse the response of the shear stress to the shear inversion. Figure 5.2 shows the time series of the response of the system for different compositions and shear rates during shear inversion. Let us define a characteristic time of the bilayer via the relaxation of the shear stress when it reaches a steady state value. As can be seen, the systems with implicit solvent molecules react very quickly on the inversion; these configurations demonstrate the shortest characteristic time due to the low density in the system. Decrease of the shear rate and increase of the density leads to an increase of the characteristic time.

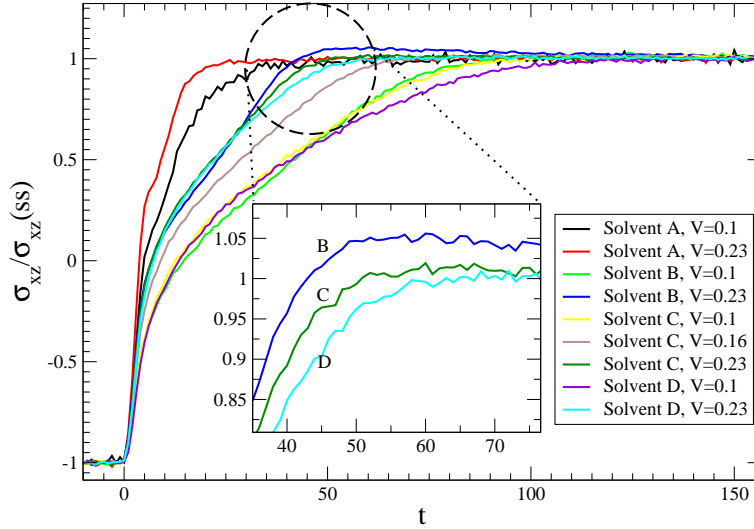


Figure 5.2: Time series of shear stress σ_{xz} normalized by the steady-state value for different compositions of the system (Solvent A, B, C, D). The distance between the walls is $D = 17.5$, grafting density is $\rho_g = 4.4\rho_g^*$. Depending on the shear rate and the system composition bilayers show different characteristic times. The inset shows how three different systems with Solvent B, C, D approach a steady state value. The shear velocity is $V = 0.23$. Solvent C and Solvent D contain stars of configuration $f = 30$, $N_{\text{mon}} = 5$. The turn time is $t_{\text{turn}} = 1.25$ in LJ units. The replacement of dimers by the stars leads to a decrease of the overshooting.

Keeping the density of the system and the shear rate constant, one can compare the behavior of different types of solvent. Solvent B, C, and D approach the steady state value differently, as can be seen in the inset. Solvent B shows an overshooting effect at time $t_0 = 50$ of approximately 6%. The replacement of the dimers by stars leads to a damping of this effect. It seems that the phenomenon depends on the size of the solvent molecules, and might be connected with their inertia. Solvent C shows approximately 2.5% overshooting above the steady state value, whereas Solvent D does not produce an overshooting at all. Moreover, systems with the highest density of stars demonstrate the longest characteristic time for the shear stress. This is due to the slow relaxation of binary interactions between the brushes and stars as well as between the interacting brushes. The brush experiences a strong deformation during the inversion. The inversion is started from a steady state configuration, in which the chains are stretched and the interpenetration between the brushes is low, as it was shown in the previous chapter. During the inversion the interpenetration between brushes significantly increases; the brushes become also strongly deformed in X - and Y -directions. The size of the brush in X -direction decreases quickly, whereas in Y - and Z -direction an increase is observed for short times; it reaches an extremum at different times depending on the type of solvent.

Afterwards, the gyration radius of the chains slowly relaxes back to the steady state value $R_{g,\alpha}^b(ss)$, where "ss" is the abbreviation for steady state, α corresponds to three directions, X , Y , and Z (see Fig. 5.3). Note, that in all three directions the extremum is reached simultaneously at time t_1 .

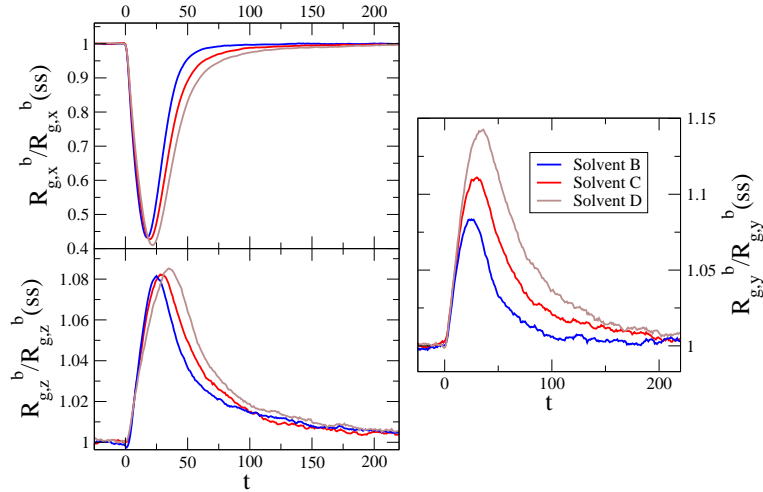


Figure 5.3: Gyration radius in X -, Y -, and Z -directions of the brush during shear inversion normalized by its steady state value $R_{g,\alpha}^b(t)/(R_{g,\alpha}^b(ss))$ with $\alpha = x$, $\alpha = x$, $\alpha = x$ respectively. The grafting density is $\rho_g = 4.4\rho_g^*$, the distance between walls $D = 17.5$, the systems of Solvent C and Solvent D include the stars of configuration $f = 30$, $N_{\text{mon}} = 5$, the shear velocity is $V = 0.23$. The biggest relative response shows the system of Solvent D. The characteristic time when the steady state value is reached in X - and in Y -directions is the shortest for the system of Solvent B, whereas in Z -direction one finds the opposite effect.

As can be seen, the more stars are in the system the longer it takes to reach a steady state value. The higher is the density of the stars in the system the larger is the relative deformation of the brushes during shear inversion. Comparing different directions one can see that the brush shows a longer relaxation in X - and in Z -directions than in Y -direction. The most significant deformation of about 55% is in the shear direction where the chains have to change the direction of the stretching. Change of the shear direction leads also to the deformation in Y -direction of about 7 – 12% depending on the type of solvent. Under steady state shear, chains were strongly stretched and the brush shows a response of about 8% in gradient Z -direction. The latter can be better characterized by the interpenetration between the opposing brushes, brushes and stars as well as the brush height.

The stars hamper the interpenetration of the brushes into each other; this effect is more pronounced under steady shear than in static equilibrium. During shear inversion the brushes interpenetrate deeply into each other, as can be seen in Fig. 5.4b). The relative

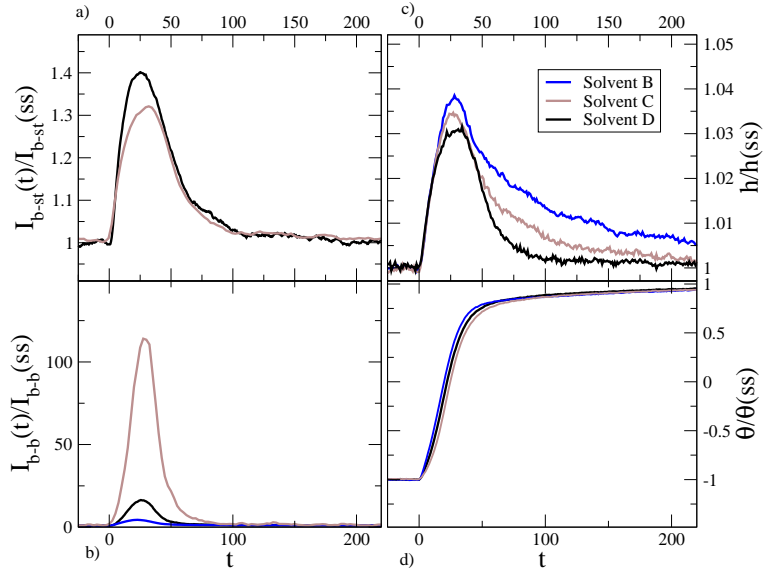


Figure 5.4: a) Relative interpenetration [see Eq. (4.33)] between brushes and stars for systems Solvent C and Solvent D; b) Relative interpenetration between opposing brushes; c) Brush height and d) Inclination angle of the chains in the brush. All variables are normalized by their steady state values ("ss"). The grafting density is $\rho_g = 4.4\rho_g^*$, the distance between the walls $D = 17.5$, configuration of stars for Solvent C and Solvent D is $f = 30$, $N_{\text{mon}} = 5$.

interpenetration at the time t_1 is the larger, the more stars are present in the system. At the same time t_1 the brushes interpenetrate 40% deeper into the stars [see Fig. 5.4a)] than during the steady shear and the brush height exhibits a maximum [Fig. 5.4c)]. It can be seen, that the more stars are located in the interface between the brushes, the quicker the brush height relaxes after shear inversion.

After reaching a maximum solvent molecules slowly diffuse out of the brush into the interface between the brushes and it takes the longest time until the system reaches the steady state in case of Solvent B. One can see, that the bigger the solvent molecules are the more compressed the brushes become in steady state and therefore the larger is the maximum of the relative brush height compared to the steady state value, $h/h(ss)$.

Brushes almost do not interpenetrate into each other in case of System D in steady-state; the decrease of the density of stars (from Solvent D to Solvent B) leads to an increase of interpenetration between the brushes. During shear inversion they interpenetrate deeply into each other through the layer of stars. Brushes do not prefer to be confined by the layer of stars during the inversion but to deform them and interpenetrate through the stars exhibiting a high relative interpenetration depth.

The inclination angle, θ , of the brushes behaves independently on the composition of the

system. θ is measured via the direction of the end-to-end distance,

$$\theta = \arccos\left(\frac{R_{e,z}}{R_{e,x}}\right), \quad (5.2)$$

where $R_{e,x}$ and $R_{e,z}$ are end-to-end distances in shear and gradient directions respectively. It reaches the static equilibrium value, $\theta = 0$, shortly before time t_1 when the brush height shows its maximum. It means that the free chain ends first reach the position above the grafted heads of the chains, shortly afterwards, due to the incompressibility of the brushes, they deform the layer of stars and the brush height reaches the maximum, as well as the interpenetration between the brushes.

Figure 5.4a) shows that an increase of the density of the stars leads also to a decrease of the relative interpenetration between brushes and stars. Our investigations reveal, that the softer the stars, the more interpenetration between the brushes and stars occurs. Due to their size the stars can not penetrate deeply into the brush. Dimers are smaller and more mobile, they are distributed in the whole system and can easier interpenetrate into the brush than the stars. In a steady state configuration beyond linear response solvent molecules are expelled out of the brush to the center of the bilayer. During the shear inversion in turn the solvent is pulled back into the brush. This effect can be analysed via the density profile of solvent molecules comparing static equilibrium and steady state configurations with the situation when the brush height shows the maximum at time t_1 during shear inversion. Figure 5.5 presents this comparison.

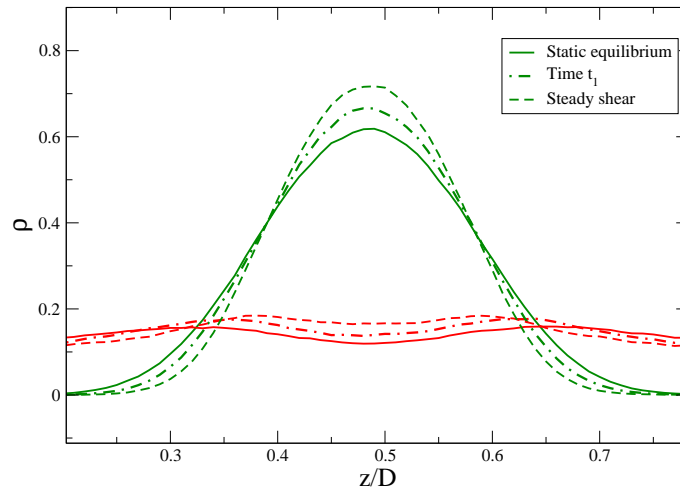


Figure 5.5: Comparison of the distribution of solvent molecules in the bilayer in static equilibrium, in steady state ($V=0.23$) and during shear inversion at time t_1 when the interpenetration between the brushes shows a maximum. The grafting density is $\rho_g = 4.4\rho_g^*$, the distance between walls $D = 17.5$, the star configuration of Solvent C is $f = 30$, $N_{\text{mon}} = 5$. Green lines correspond to the stars and red lines to the solvent molecules.

Our results reveal that during very short times solvent molecules are expelled out of the interface between the brushes and then become distributed within the brushes again. The brushes do not reach the interpenetration depth that they have in static equilibrium, as well as the solvent molecules do not have enough time to enter the brush as deep as under static equilibrium conditions. The same conclusion can be drawn about the stars, which become thicker during shear inversion but still remain more compressed than in static equilibrium.

During the shear the brushes can show slip, stick or slip-stick behavior depending on the grafting density, which can change the hydrodynamic boundary change between the different regimes. This phenomenon can be influenced by the presence of the stars. In order to characterize it one should analyse the velocity profiles of each component of the system[36].

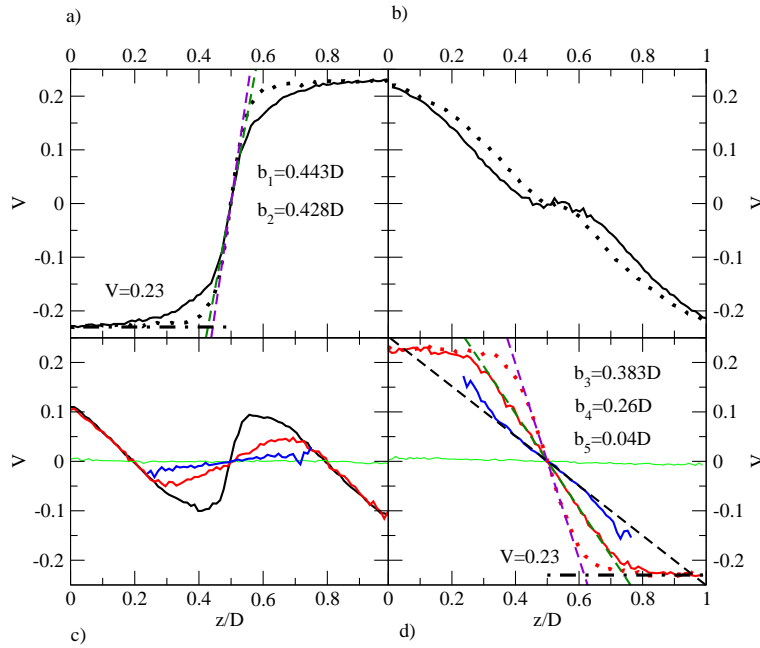


Figure 5.6: Velocity profiles of each component in the system. The comparison between the configurations under steady shear [Figs. a) and d)], the configuration when interpenetration between brushes exhibits a maximum [Fig. b)] and the configuration shortly after inversion [Fig. c)]. The systems of the Solvent B (dotted lines) and Solvent C (full lines) are compared. The grafting density of the brushes is $\rho_g = 4.4\rho_g^*$, the distance between the walls $D = 17.5$, the star configuration in system of Solvent C is $f = 30$, $N_{\text{mon}} = 5$, the shear velocity is $V = 0.23$. The black lines correspond to the profiles of the brush, the blue lines to the stars, the red lines to the solvent molecules. The dashed lines show the linear approximation of the profiles in the middle of the system for different components. The full green lines correspond to the center monomer of the stars.

Figures 5.6a) and d) show the velocity profiles in steady state ($W \gg 1$). Figure 5.6a) corresponds to the profiles before shear inversion and Fig. 5.6d) shows the velocity profile after shear inversion in the inverted steady state configuration. These states are equivalent but the shear is applied in the opposite direction. The hydrodynamic boundary can be characterized by the slip length, $z = -b$, behind the substrate, when the extrapolation of the linear profile $v(z)$ attains the steady state substrate velocity V , as assumed when no slip occurs. As can be seen, the slip length is positive for all components, therefore the brushes show strong sticking effects with $b_1 = 0.443$ without stars (Solvent B) and $b_2 = 0.428$ when half of the solvent molecules are replaced by stars (Solvent C). Solvent molecules follow the behavior of the brushes exhibiting a smaller sticking effect. Similarly to the behavior of brushes the slip length is smaller in case of Solvent C ($b_2 = 0.383$ and $b_3 = 0.26$). Stars are located in the middle of the bilayer, they are rotating since the center monomers reveal zero profile [see Fig. 5.6c) and d)]. The slip length is finite for the stars and equal to $b_1 = 0.04$. Shortly after the shear inversion [Fig. 5.6b)], when the shear inversion is almost performed ($t < t_{\text{turn}}$), brushes and solvent molecules follow the behavior of the substrates close to them, but the profile of the brushes in the middle of the bilayer is still not altered, whereas stars stop rotating and solvent molecules yield a much smaller slip length. Stars react on the external changes very quickly, solvent molecules follow the behavior of stars and the profile of the solvent molecules is altered. When the interpenetration of the brushes show a maximum (at time t_1) [see Fig. 5.4c)], brushes and solvent molecules for the systems without stars (Solvent B) show a linear profile. At this time the brushes behave like an ideal Newtonian liquid and "forget" effectively that they have a backbone connectivity. Solvent molecules follow the behavior of the brushes. In case of Solvent C brushes and solvent molecules seem to follow the behavior of stars in the middle of the bilayer and build a plateau. In the next configurations this effect is slowly destroyed and the brushes start dominating.

This can be observed more precisely in the time series of the slip length for each component. The modification of the slip length due to the presence of the stars can be seen in Fig. 5.7a). In presence of stars the brushes reach the steady state slip length later than in case of Solvent B. The behavior of the solvent molecules is also altered by the presence of the stars but less significantly as for the brushes. Stars show a slight overshooting effect by exhibiting a larger slip length than in the steady state. Similarly to the overshooting effect of the shear stress, σ_{xz} , the effect occurs also at time point t_0 . Further analysis of the structure can be done via the chain end distribution. The relative interpenetration of the chain ends into the opposing brush is strongly influenced by the presence of the stars.

Figure 5.7b) shows that the maximum of the interpenetration of the chain ends into the opposing brush is not correlated with the maximum of the interpenetration of the brushes into each other ($t = t_1$) in the presence of the stars. It is connected with the fact,

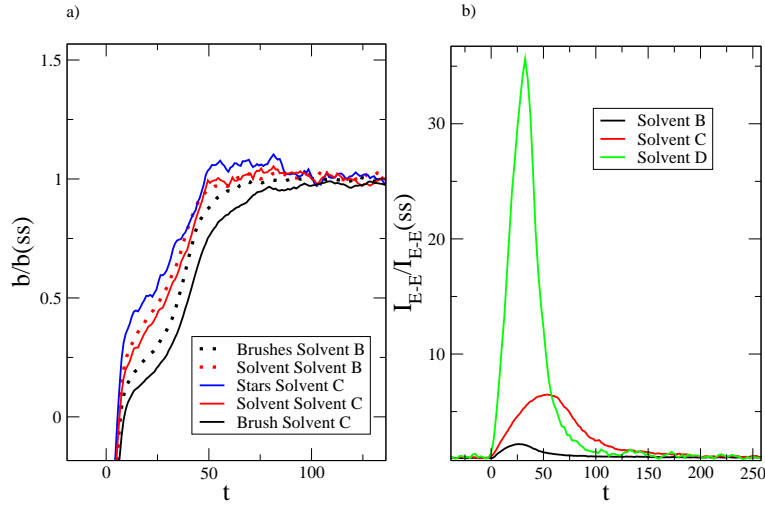


Figure 5.7: The time series of the slip length normalized by its value in steady state (left plot) and the relative interpenetration of the chain ends (right plot) during shear inversion. The grafting density is $\rho_g = 4.4\rho_g^*$, the chain length $N = 30$, the distance between the walls is $D = 17.5$, the star configuration of Solvent C and Solvent D is $f = 30$, $N_{\text{mon}} = 5$. Different compositions of the system exhibit different characteristic times for approaching the steady state after shear inversion.

that the chain ends first reach the static equilibrium position (at time $t < t_1$) when the tilting angle is zero. Then, the interpenetration of the brushes reaches the maximum (at $t = t_1$), such that chain ends start pushing on the layer of the stars, penetrate through them and enter the opposing brush. Afterwards, the maximum of the interpenetration of the chain ends distribution is reached.

In the steady state the chains are tilted and stretched, the stars are compressed in the interface between the brushes as it is shown schematically in Fig. 5.8a).

Configurations, where the walls start moving in the opposing direction and shear inversion is already started are shown in Fig. 5.8b). In this time the brushes interpenetrate through the stars with a part of their chains. This leads to a significant increase of the interpenetration depth between the brushes. The layer of stars is strongly deformed. After a characteristic time the system reaches again the steady state configuration [Fig. 5.8c)].

In order to complete the characterization of the system let us analyse the gyration radius of the stars. Figure 5.9 shows the response of the stars in X -, Y -, and Z -directions.

Stars experience deformation in all three directions. The strongest relative deformation can be seen in Z - and in X -directions due to the fact, that the stars are squeezed strongly in the gradient and stretched out in the shear direction in steady state beyond linear response. The more stars are located in the system and, therefore, the less freedom and

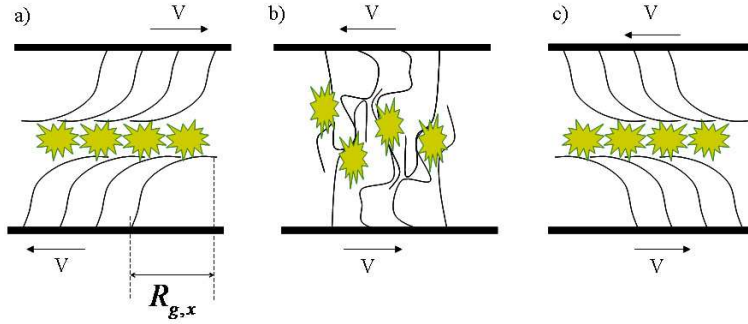


Figure 5.8: Schematic picture of brushes and stars during shear inversion. a) corresponds to the configuration in steady state with shear velocity V . Chains are tilted and stretched. Stretching can be characterized by the gyration radius $R_{g,x}$. b) is the configuration during shear inversion, stars are located in the interface between brushes and strongly deformed, chains interpenetrate through the layer of stars into the opposing brush. c) shows the new "reflected" steady state configuration after shear inversion.

space is left in the interface between the brushes, the smaller is the relative deformation of the stars during shear inversion. The Y -direction shows a response of about 1%. In the case of Solvent D one can see that the stars follow the collective motion in Y -direction showing periodic movement, which was first observed in bulk systems[60].

Let us turn back to the gyration radius of the brushes. As it was already mentioned, it shows a different behavior with different characteristic times depending on the composition of the system. As can be seen in Fig. 5.10, the response of the system of Solvent A is very small, the system is in a crossover from the linear response regime to the non-Newtonian behavior. The systems of Solvent B, C, and D demonstrate more significant responses. The steady state value of the gyration radius for each composition of the system depends on the density of stars in the system. Furthermore, the gyration radius of the brushes exhibit a different behavior depending on the shear rate.

To characterize the crossover behavior from one steady state configuration to the inverted one we follow an idea originally developed in Ref. [33]. From the steady-state investigations we know the dependence of the gyration radius of the brushes on the shear rate. As it was shown, it has a power-law behavior

$$\frac{R_{g,x}^2(\dot{\gamma})}{R_{g,x}^2(0)} = \left(\frac{\dot{\gamma}}{\dot{\gamma}^*} \right)^{0.5}, \quad (W \gg 1) \quad (5.3)$$

for semidilute brushes under good solvent conditions.

The characteristic time of the system, τ_c , after which the shear stress reaches its steady state value, can be defined by the characteristic length scale divided by the characteristic velocity in the system, V . During shear inversion the free chains' ends move above the

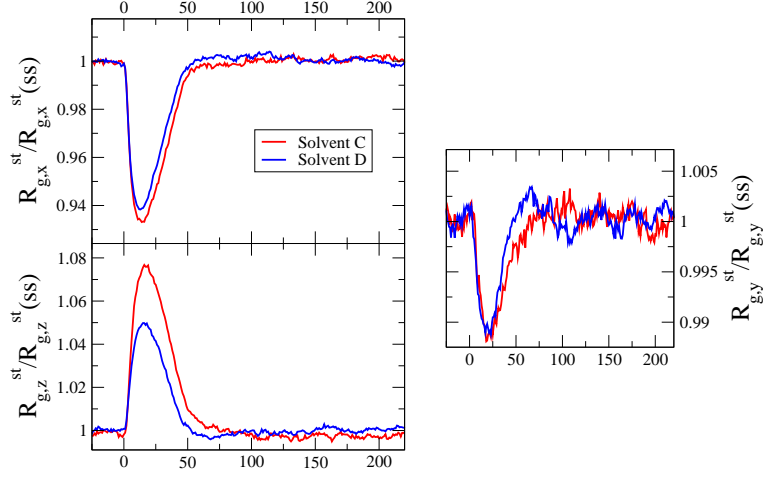


Figure 5.9: Gyration radius of stars in X -, Y -, and Z -directions normalized by its value in steady state as a function of time during shear inversion ($R_{g,\alpha}^{\text{st}}(t)/R_{g,\alpha}^{\text{st}}(ss)$ with $\alpha = x, \alpha = x, \alpha = x$, respectively). The grafting density is $\rho_g = 4.4\rho_g^*$, the chain length $N = 30$, the distance between the walls is $D = 17.5$, the star configuration of Solvent C and Solvent D is $f = 30, N_{\text{mon}} = 5$. The strongest deformation is observed in shear (X) and gradient (Z) directions, whereas in Y -direction stars show a weak response.

grafted chain ends from one steady state configuration [see Fig. 5.8a)], when the chains exhibit the gyration radius $R_{g,x}(\dot{\gamma})(ss)$ in shear direction, to the equivalent reflected steady state configuration [Fig. 5.8c)], such that the free chain ends traveled an approximate distance proportional to twice the gyration radius in shear direction. Therefore, $R_{g,x}(\dot{\gamma})(ss)$ can be defined as a characteristic length scale, meaning that the whole chain has to travel over its own (extended) size during the characteristic time τ_c . Therefore, for the decay of the gyration radius in time after the shear inversion is started, one may write

$$\frac{R_{g,x}(\dot{\gamma}, t)}{R_{g,x}(\dot{\gamma})(ss)} = 1 - \frac{t}{\tau_c}. \quad (5.4)$$

Using the definition of the Weissenberg number as a ratio of the shear rate $\dot{\gamma}$ and the critical shear rate $\dot{\gamma}^*$, where $\dot{\gamma} = 2V/D$ [see Eq. 5.3], the characteristic time of the system can be written as

$$\tau_c \propto \frac{R_{g,x}}{V} = \frac{2R_{g,x}(0)}{\dot{\gamma}D} \left(\frac{\dot{\gamma}}{\dot{\gamma}^*} \right)^{0.25}. \quad (5.5)$$

This approximation should work for systems far beyond the linear response regime, where the power-law behavior [Eq. 5.3] dominates.

Figure 5.11 shows the gyration radius of chains, which are normalized by their value under steady shear, $R_{g,x}(ss)$, as a function of time divided by the characteristic time, τ_c .

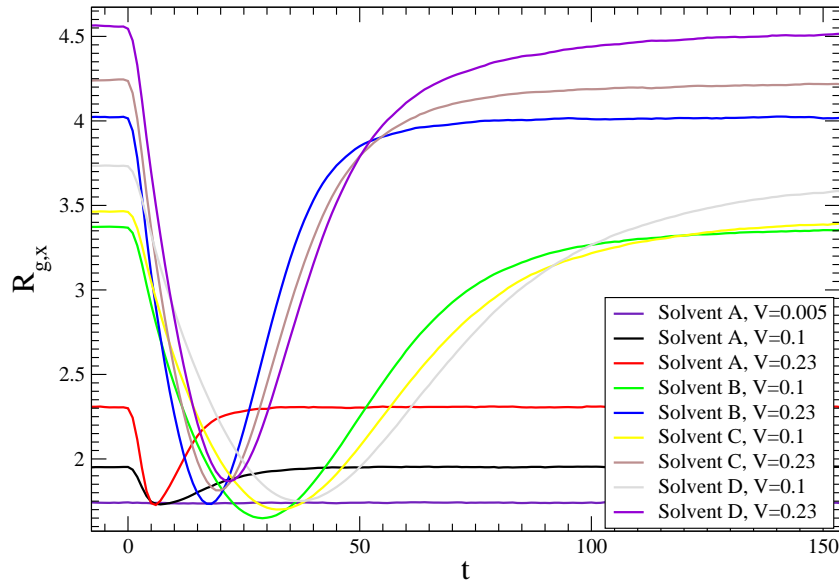


Figure 5.10: Gyration radius of brushes in shear direction as a function of time during shear inversion for different compositions of systems and shear rates. The distance between the walls is $D=17.5$, the grafting density is $\rho_g = 4.4\rho_g^*$, the chain length $N = 30$. The systems show different behaviors from the case when the gyration radius does not respond on shear inversion up to the strong deformation. The behavior depends on the shear rate, components of the system, molecular parameters of the brushes and stars (if present).

One can see that the decay of the gyration radius of different parameters from the steady state configuration shortly after inversion can be mapped onto each other and it follows the ratio (5.4). Moreover, the steady state value is reached on the same time scale for the different systems.

The same procedure can be done with the shear stress for large shear rates corresponding to the non-Newtonian behavior. This is shown in Fig. 5.12. The shear stress is normalized by its value in steady state and the time is rescaled by the characteristic time τ_c . One can see that, independently of the shear rate, systems with different molecular parameters (grafting densities, chain lengths, star configurations etc.) and different types of the solvent can be mapped onto each other. The way how the shear stress approaches the steady state value still slightly depends on the type of the solvent (the overshooting effect discussed above). This may be explained by the fact that objects of different sizes in the brush have different diffusion constants.

The same scaling plots can be performed not only for the shear inversion, but also for the onset of motion, when as a starting point the static equilibrium configuration is taken and afterwards shear is started. Moreover, it is tested that the same scaling arguments work also for the end-to-end distance of the chains, number of binary interactions

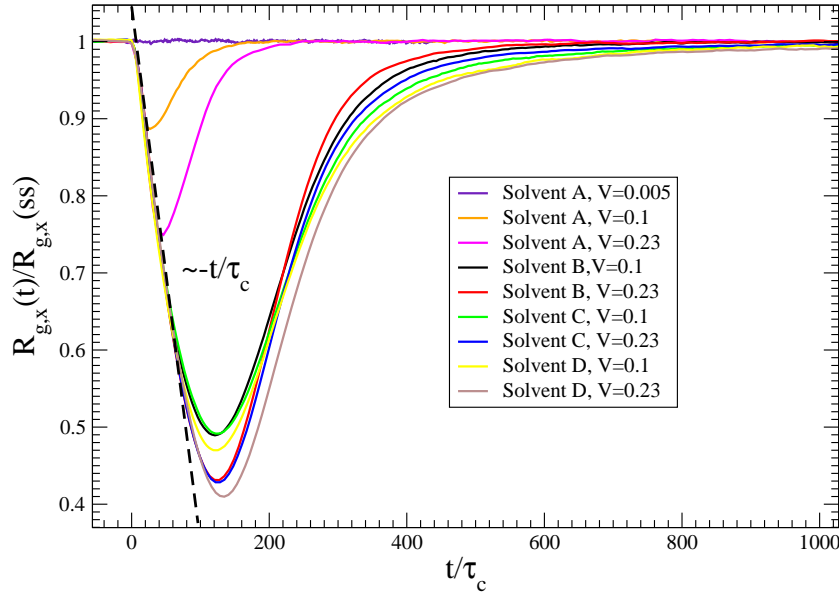


Figure 5.11: The gyration radius of the chains normalized by its value in steady state, $R_{g,x}/R_{g,x}(ss)$, as a function of rescaled time, t/τ_c . The distance between the walls is $D = 17.5$, the grafting density is $\rho_g = 4.4\rho_g^*$, the chain length $N = 30$. Different systems of different compositions show the same decay of the gyration radius shortly after inversion; the steady state value is reached on the same time scale in non-Newtonian regime ($W \gg 1$). The dashed line corresponds to the predicted decay of the gyration radius [Eq. 5.4].

between opposing brushes and therefore also for lateral forces acting between them. It shows that knowledge of characteristics of the system in static equilibrium, such as the gyration radius of chains, $R_g(0)$, and the critical shear rate $\dot{\gamma}^*$, delivers non-equilibrium characteristics of the system even for non-stationary shear.

Now let us turn to the response of the stress tensor in the gradient direction, σ_{zz} .

Systems with implicit solvent molecules show no response for the normal stress [see Fig. 5.13]. Due to the low density of the system compared to systems with explicit solvent molecules, fluctuations are much stronger. In order to get a signal with the fluctuations of σ_{zz} of about 1% it is necessary to average over more than 500 different configurations. In spite of that the response of the normal stress can not be seen. This can be also due to the fact, that the critical shear rate for these systems is much larger than for the systems of the Solvent B, C and D. For systems with explicit solvent molecules the averaging was done over 100 configurations. Let us now analyse the system of Solvent B. The system does not show any response to the inversion for the shear rates in the linear response regime. Increase of the shear rate leads to the occurrence of the non-trivial response. With the highest simulated shear rate of $V = 0.23$ we observe a minimum of about 1.2%. The normal stress starts showing a response for shear rates

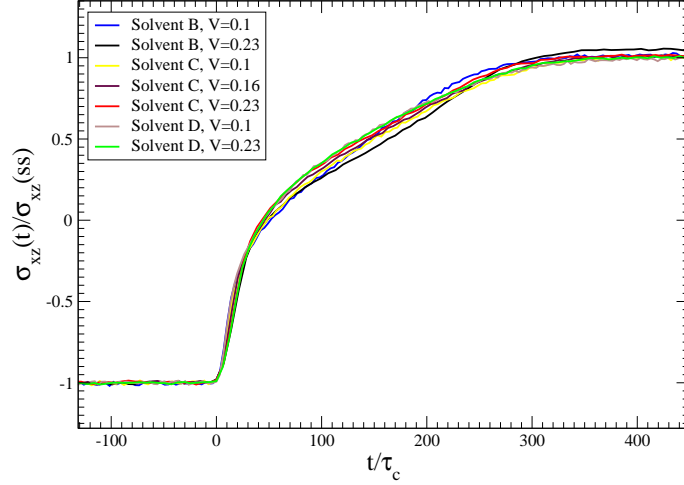


Figure 5.12: The shear stress normalized on its value in steady state, $\sigma_{xz}(t)/\sigma_{xz}(ss)$, as a function of rescaled time t/τ_c . The distance between the walls is $D = 17.5$, the grafting density is $\rho_g = 4.4\rho_g^*$, the chain length $N = 30$. Different systems with different characteristic times can be mapped onto each other for shear velocities beyond linear response regime.

higher than the critical shear rate. Also, the systems of the Solvent C and D do not show any differences in the normal stress in the linear response regime. Fixing the shear velocity and increasing the size of the solvent molecules (going to the Solvents C and D) leads to a larger response. We find that the more macroobjects are present in the system, the stronger is the observed response. Increase of the chain length N leads to a slight increase of the response and to a significant increase of the characteristic time while approaching the steady state value (similarly to the steady shear).

For systems without stars (Solvent B) we observe a small overshooting effect of about $\approx 1\%$. This phenomenon appears during short times just after the inversion due to the inertia of the brushes and the solvent molecules. An increase of the turn time, t_{turn} , leads to a decrease of the effect (see the inset of Fig. 5.13). The overshooting effect was not observed for the systems with stars since the stars are located in the middle of the system and dissipate the energy via rotation instead of following the movement of the brushes in shear direction.

In order to understand the response of the normal stress let us analyse the components of it. It consists of the LJ interactions and the backbone connectivity of the brushes, σ_{zz}^b , stars, σ_{zz}^{st} , and solvent molecules, σ_{zz}^{so} , as well as of the pairwise LJ interactions between the solvent molecules and the brushes, $\sigma_{zz}^{b-\text{so}}$, solvent molecules and stars, $\sigma_{zz}^{\text{so}-\text{st}}$, brushes and stars, $\sigma_{zz}^{b-\text{st}}$. The total normal stress then reads

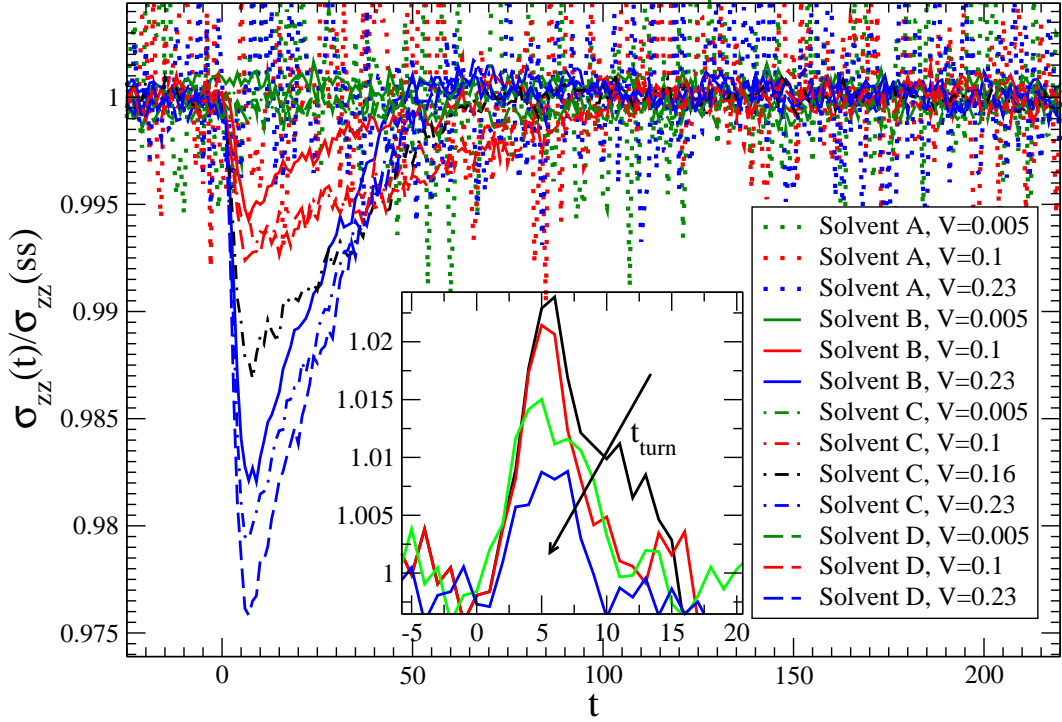


Figure 5.13: Normal component of the stress tensor normalized by the steady state value, $\sigma_{zz}/\sigma_{zz(ss)}$, as a function of time during shear inversion. Depending on the shear rate and components of the system, the stress shows a different response. Distance between the walls is $D = 17.5$, the grafting density is $\rho_g = 4.4\rho_g^*$, the chain length $N = 30$, the turn time of the inversion $t_{turn} = 10$. The higher the shear rate is and the more stars are present in the system, the more pronounced is the response. The inset shows the response of σ_{zz} for different turning times $t_{turn} = 1.25, t_{turn} = 2.5, t_{turn} = 5, t_{turn} = 10$ for the system of Solvent B. The quicker the shear inversion is performed, the larger is the overshooting of the normal component.

$$\sigma_{zz} = \sigma_{zz}^b + \sigma_{zz}^{st} + \sigma_{zz}^{so} + \sigma_{zz}^{b-so} + \sigma_{zz}^{so-st} + \sigma_{zz}^{b-st}. \quad (5.6)$$

The Fig. 5.14a) shows the response of these components, that reveal a minimum. These are σ_{zz}^b , σ_{zz}^{st} , and σ_{zz}^{b-so} . All the other components exhibit a maximum. Due to the presence of the stars the number of binary interactions between the brushes decreases. This fact leads also to the undershooting effect of this component. The stars can be interpreted as a brushes in the limit of high grafting density and finite radius of curvature for the anchored surfaces. Therefore, the stars reveal similarities to the brush behavior. The solvent molecules show a more complicated behavior. First, the number of binary interactions between the brush and solvent molecules decreases; the dimers penetrate back into the brush from the middle of the bilayer. At this time the brush has a strong

interaction with the opposing brush showing a strong interpenetration. Further relaxation from this configuration leads to an increase of the interaction between the brushes and the solvent molecules, such that the brush tends to expel the solvent molecules back to the interface. This two-step process can be seen in more detail in the layer resolved analysis of the interaction between the brushes and the solvent molecules. Figure 5.14b) shows that in different layers of the system one can see different processes. The middle layer (5) shows an increase of the interactions between the brushes and the solvent molecules. The stars are dominating the middle layer. Therefore the brush-solvent component, σ_{zz}^{b-so} is rather small for this layer [see inset of Fig. 5.14b)]. The analysis of the 4th layer shows how the solvent is expelled from the layer. Closer to the substrates a two-step process appears. The contributions of the 2nd and the 3d layers are the most significant. They reveal a slow diffusion of the solvent molecules back to the interface between the brushes.

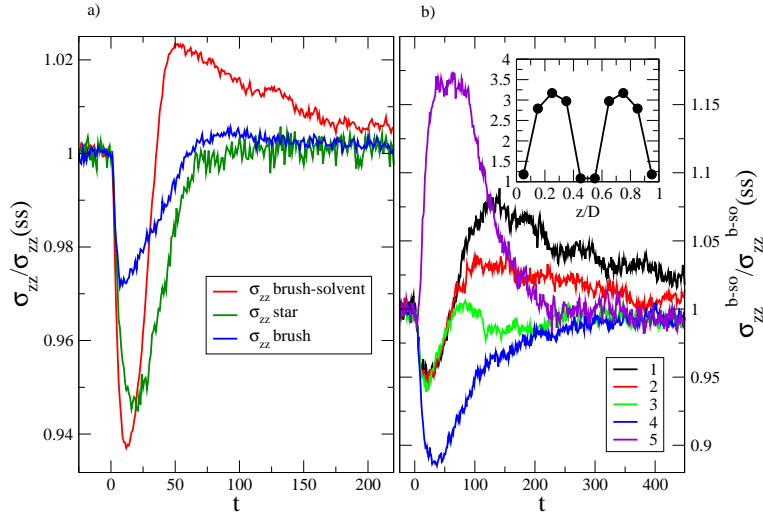


Figure 5.14: Components of the normal stress in the systems during shear inversion. The distance between the walls is $D=17.5$, the grafting density is $\rho_g = 4.4\rho_g^*$, the chain length $N = 30$. The system of the Solvent C with the stars of configuration $f = 30$, $N_{mon} = 5$. Left panel shows the response of the normal stress of the different components. Right panel shows the layer resolved response of the interactions between brush and solvent molecules. The numbers from 1 to 5 correspond to the layer number. The 5th layer is the middle layer. The inset shows the steady state value in each layer.

The same layer resolved analysis can be done for the contribution of the interactions between the solvent molecules. The same two-step process can be seen in the 4th layer. The solvent is first compressed by the brushes and hence solvent molecules interact stronger with each other. Afterwards, they leave the layer and diffuse back after some relaxation time. The results are presented in Fig. 5.15a). The inset shows the profile of

this component. Since the solvent molecules are expelled out of the brush, the most significant input is observed in the middle of the system. The pressure of the solvent decreases moving towards the substrates.

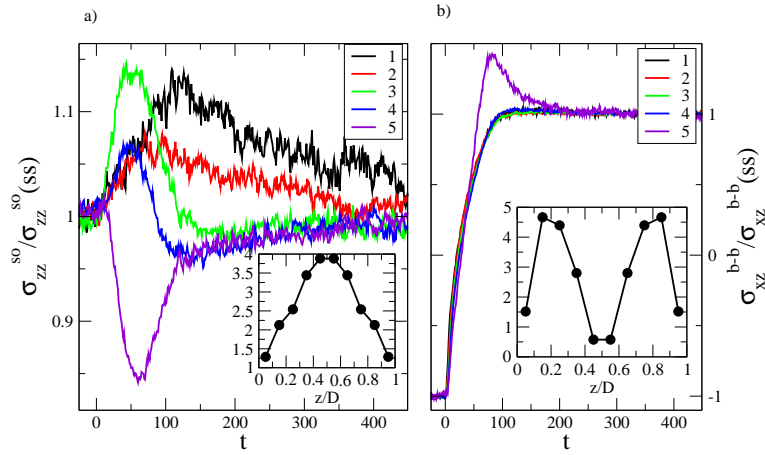


Figure 5.15: Component of the normal pressure (layer resolved) due to the interactions between the solvent molecules (a) and component of the shear stress (layer resolved) due to the interactions between the brushes during the shear inversion (b). The distance between the walls is $D=17.5$, the grafting density is $\rho_g = 4.4\rho_g^*$, the chain length $N = 30$. The system of Solvent C with the stars of configuration $f = 30$, $N_{\text{mon}} = 5$. Insets show the profiles of the steady state values in each layer.

The layer resolved analysis can be helpful also in explaining the overshooting effects of the shear stress. As can be seen in Fig. 5.15b), the first 4 layers show a universal behavior of the shear stress, whereas the 5th layer shows the overshooting. This effect is more pronounced in the absence of stars (the case of the Solvent B) in correspondence with the data presented above for the whole shear stress. The chain ends, as well as the binary interactions between the brushes and the other components in the interpenetration region play a crucial role.

Chapter 6

Charged systems

6.1 Introduction

Up to now we have dealt with electrically neutral brushes. Charged brushes have a very rich spectrum of properties depending on grafting density, chain length, charge fraction, and salt concentration. They enable controlling of segregation and aggregation processes and therefore are important in many industrial applications, such as food industry, water treatment, mining, medical science etc. Moreover, experiments reveal that the friction coefficient between two opposing polymer brushes can be significantly decreased for charged grafted chains with counterions and added salt [42]. As for neutral systems, also for charged brushes there is no complete picture of the rheological mechanisms causing the small friction. In contrast to the experiment, computer simulations with soft potentials report equivalent friction coefficients when comparing charged and neutral systems[114]. In this chapter, we present our results for charged systems and show how charges modify the lubrication properties of polymer brush bilayers.

6.2 Influence of long-range interactions

As a first step we ensured, that the program and implemented technique work correctly. We tested the program for a simple system, which consists of two types of monomers, positively and negatively charged. The number of negatively charged ions is larger than the number of positively charged ions, $n_- > n_+$. The Gouy-Chapman theory[115] predicts for this situation the double layer effect in monomeric profiles[116]. Measured density profiles from our simulations can be fitted well by the theoretical predictions. Moreover, the measured densities of the positive and the negative ion species in the bulk are in good agreement with Poisson-Boltzmann equation [see Eq. 1.39] and are in good agreement.

Moreover, we performed simulations of charged opposing brushes and directly compared

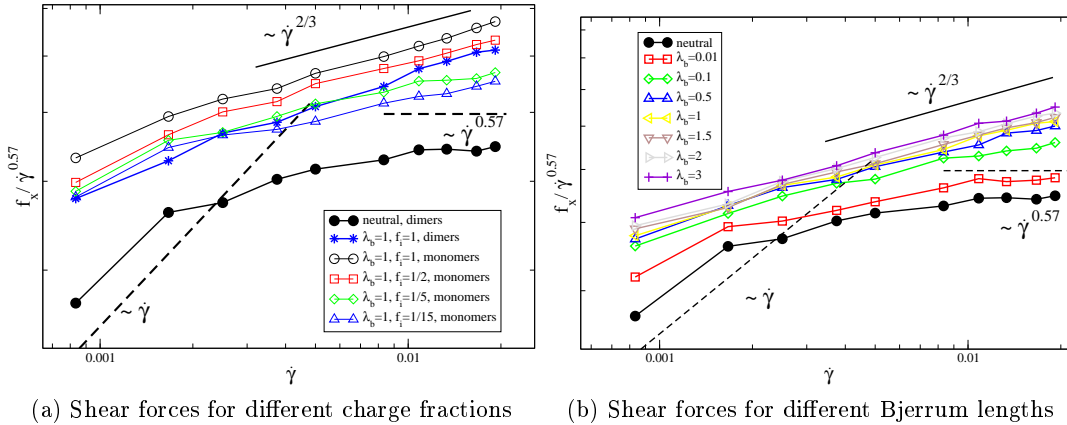


Figure 6.1: Shear forces normalized by the predicted power-law, $\dot{\gamma}^{0.57}$, for the neutral systems as a function of the shear rate $\dot{\gamma}$. The dashed lines correspond to the predicted linear response (linear dependence) and the non-Newtonian behavior (power-law dependence). The full line corresponds to empirically measured for strongly charged systems power-law. The grafting density is $\rho_g = 2.2\rho_g^*$, the distance between the walls is $D = 12$.

with already existing results from Ref. [117] for the same model static equilibrium.

In this chapter we will focus on sheared opposing polyelectrolyte brushes. Similarly to the neutral brushes we characterize the charged brushes by the lateral gyration radius. Our simulations reveal the same power-law behavior as for the neutral systems (see Fig. 4.12). The charged and neutral systems can be mapped onto each other for different grafting densities, ρ_g , Bjerrum lengths, λ_B , and charge fractions, f_i . We observe that the critical shear rate becomes smaller, such that the crossover from the linear response to the non-newtonian behavior occurs at smaller shear rates.

In order to observe crossover in the behavior from neutral to charged systems we varied the strength of the long-range interactions through the Bjerrum length, λ_B , and the charge fraction, f_i and analysed the shear stress. Due to the presence of the Coulomb interactions, the shear forces should be influenced significantly compared to neutral systems. In this section we investigate only the case without stars (Solvent B).

Figure 6.1 shows the shear forces as a function of the shear rate for different charge fractions and Bjerrum lengths. The shear forces are normalized by the prediction for the shear force of neutral systems, $f_x \propto \dot{\gamma}^{0.57}$, such that for large $\dot{\gamma}$ and neutral systems a plateau is reached. Increasing the Bjerrum length (Fig. 6.1b) leads to a modification of the power law. The systems with larger Bjerrum lengths leave the linear regime earlier than the neutral systems. The charges lead to a swelling of the brushes in Z -direction. One can observe, that there is an interplay between the long-range interactions and the steric contributions. As can be seen, the Coulomb interaction starts dominating from the Bjerrum lengths $\lambda_B > 0.5$ and the exponent of the power-law converges to $\dot{\gamma}^{2/3}$ for large λ_B . The variation of the charge fraction can be interpreted as a variation of the degree of

dissociation of the charged chains. Similarly to the increase of the Bjerrum length, the increase of the number of charged monomers in the grafted chains leads to a modification of the power-law behavior and shows a crossover from the neutral regime to strongly charged systems (Fig. 6.1a). Up to now, we modeled counterions and solvent molecules as a dimers. This may lead to a bridging effect, when two monomers of different chains are "connected" by an oppositely charged dimer between them. In order to surpass this effect, we simulate systems with the charged monomeric counterions and compare the shear forces to the case of dimers. Independently of the size and valence of the counterions we observe a convergence of the power law to $f_x \propto \dot{\gamma}^{2/3}$ for strongly charged systems.

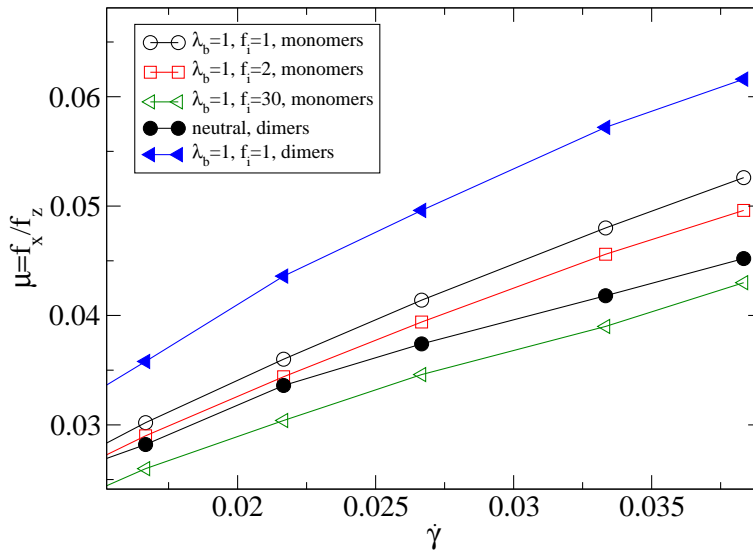


Figure 6.2: Kinetic friction coefficient as a function of shear rate. Comparison of different charge fractions f_i for a given $\lambda_B = 1$. Increase of the strength of the long-range interactions leads to an increase of the friction. The distance between the walls is $D = 12$, the grafting density $\rho = 2.2\rho^*$, the length of the grafted chains $N = 30$.

Measurements of the shear and normal forces allow to compare the friction coefficients for different strengths of the Coulomb interactions. Figure 6.2 shows the kinetic friction coefficient as a function of the shear rate. It reveals that an increase of the Bjerrum length leads to an increase of the friction coefficient. Similarly, an increase of the charge fraction, while fixing the Bjerrum length at $\lambda_B = 1$, increases the friction. Comparing different types of counterions reveals that monovalent counterions (modeled as monomers) yield a lower friction coefficient than bivalent counterions (simulated as dimers). One can see that the system of the monovalent counterions with the charge fraction, $f_i = 1/N$, when only the end-monomers are charged, shows a lower friction coefficient than the neutral system with the solvent molecules simulated as dimers. This means that decrease

of the size of solvent molecules leads to a decrease of the friction coefficient, the same result that is observed for neutral systems when different types of solvent are used.

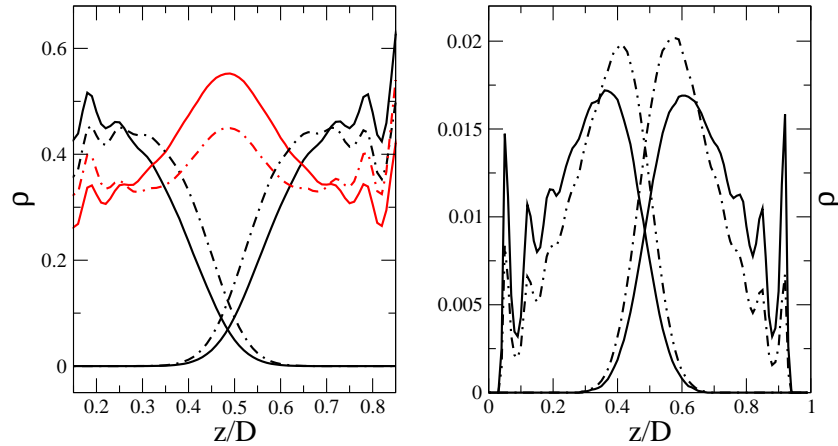


Figure 6.3: Density profile of each component of the system (right plot) and distribution of end-monomers for charged (dashed-dotted lines) and neutral (full lines) systems. The red lines represent the solvent molecules, black lines the brushes. The distance between the walls is $D = 12$, the grafting density is $\rho = 2.2\rho^*$, the chain length $N = 30$, the Bjerrum length $\lambda_B = 1$, the shear velocity $V = 0.23$. Charged systems expell less solvent molecules to the center of the bilayer and result in a larger interpenetration between the brushes as compared to neutral systems.

In order to understand the mechanisms of the rheological response we analyse the density profiles. Figure 6.3 shows the difference between charged and neutral systems. Compared to simulations with soft potentials[114], our model reveals a larger overlap region. Similarly to the solvent in neutral systems, charged brushes expel the counterions under shear. This effect is less pronounced due to the attraction between counterions and brushes. One can see that the brushes are swollen compared to the neutral case. The brush height is larger and so is the interpenetration region, which leads to a larger friction coefficient. A comparison of the distribution of the chain ends between charged and neutral systems shows that the chains are more stretched in the shear direction. The maximum of the distribution of the free chain ends is closer to the center of the bilayer and is higher compared to the neutral brushes. One can see that the free chain ends interpenetrate into the opposing brush deeper than in the neutral case.

Let us compare the overlap integrals [see Eq. (4.33)] for the different Bjerrum lengths. As can be seen in Fig. 6.4, increasing the Bjerrum length leads to an increase of the overlap integral. A slight increase of the overlap integral upon increasing the Bjerrum length is observed for all simulated shear rates; this fact effects also the shear forces, which show the same tendency. As mentioned above, the brushes become swollen, which was confirmed by the measurements of the brush height. Moreover, our simulations reveal,

that increase of the Bjerrum length leads to a stronger inclination of the chains. The chains become stiffer and more stretched, but still the gyration radius in shear direction increases while increasing the strength of the long-range interaction. The counterions are more and more condensed on the chains being strongly attracted.

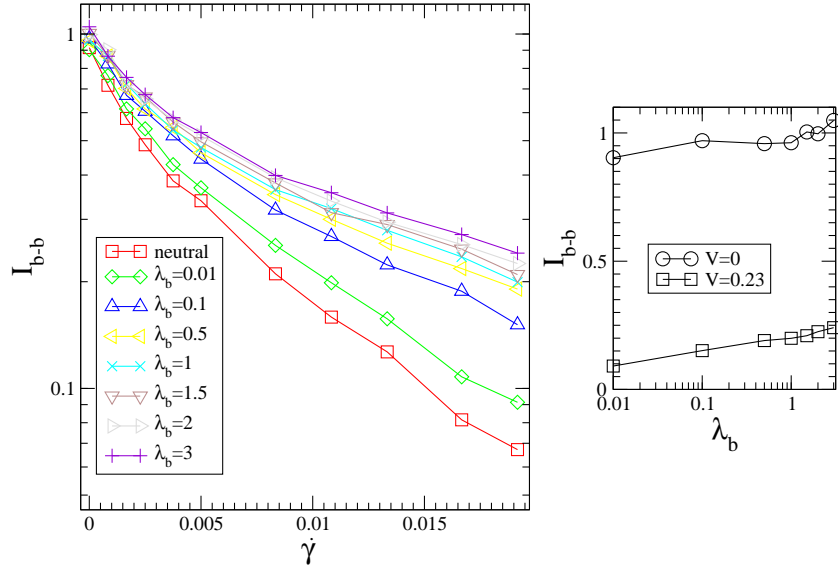


Figure 6.4: Overlap integral of the brushes vs. shear rate for different Bjerrum lengths (left plot) and dependence of the overlap integral on the Bjerrum length in static equilibrium and steady state (right plot). The distance between the walls is $D = 12$, the grafting density is $\rho = 2.2\rho^*$, the chain length $N = 30$. An increase of the strength of the Coulomb interaction leads to an increase of the overlap between the brushes.

In order to further compare neutral and charged systems under static equilibrium and steady shear, we measure the pair correlation function between the solvent and brush monomers, $g(r)$. This function is normalized such that it reaches unity on large distances and can be interpreted as the probability to find another particle at the distance r away from a test particle.

It turns out that in static equilibrium the neutral systems show smaller correlations than the charged systems, which is an expected effect due to the long-range interactions. A periodical structure appears at small distances ($r \lesssim 3\sigma$); the periodicity is proportional to the size of the monomers, σ . The neutral systems show larger correlations at larger distances ($r > 3\sigma$) in steady shear, while the charged systems exhibit stronger correlations at smaller distances ($r < 2\sigma$), when more counterions are attracted by the oppositely charged chains. A continuous increase of the Bjerrum length from $\lambda_B = 0.01$ up to $\lambda_B = 3$ shows a continuous change of this property.

The expulsion of counterions can be characterized by the charge distribution. It can be

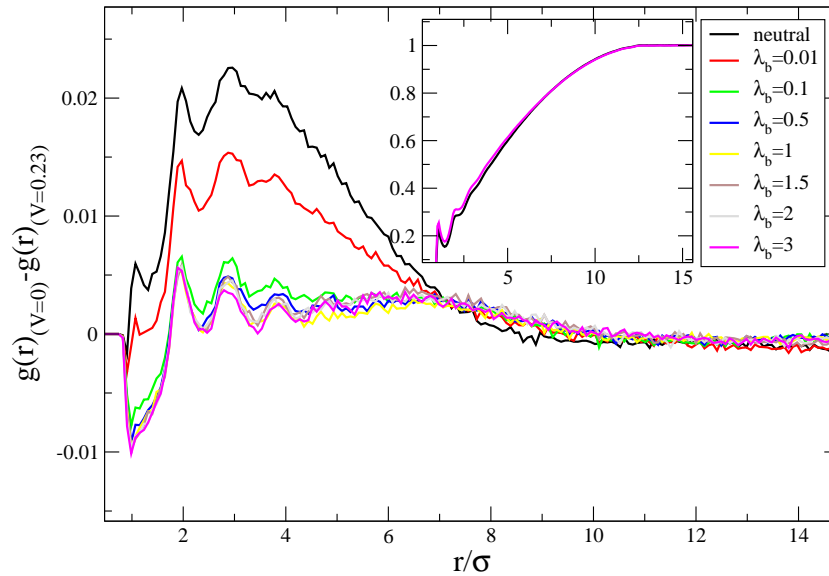


Figure 6.5: Difference between the pair correlation functions of the brush monomers with the counterion monomers in static equilibrium and steady shear $[g(r)_{V=0} - g(r)_{V=0.23}]$ for different Bjerrum lengths. The distance between the walls is $D = 12$, the grafting density $\rho = 2.2\rho^*$, the chain length $N = 30$. The inset shows pair correlation functions for the neutral system (black line) and the strongly charged system, $\lambda_B = 3$ (red line).

calculated as a difference between the density profiles of the counterions, that are positively charged, and the brush monomers, that are negatively charged, $\rho_c = \rho_s - \rho_b$. Figure 6.6 shows the charge distribution for different Bjerrum lengths in static equilibrium and steady shear ($V = 0.23$).

Let us first focus on the systems without shear. For the almost neutral systems when the Bjerrum length is $\lambda_B = 0.01$, one can see that the counterions are distributed through the whole layer, but the steric repulsion dominates over the electrostatic interactions and one observes an overcharging effect in the middle of the system. The integral under the curve is zero, such that the whole system is electrically neutral. Upon increase of the Bjerrum length the influence of the electrostatic interactions increases and the positively charged counterions are pulled inside the brush by the negatively charged chains. The charge distribution becomes flat; however for the largest simulated Bjerrum length the system is still not completely neutral in the middle of the bilayer and yields about 1.5% overcharging.

Let us now turn to the sheared systems. As we have already seen, the solvent molecules are expelled out of the neutral brushes upon increasing shear rate. This effect remains for charged systems, but decreases with an increase of the Bjerrum length. The larger the Bjerrum length, the stronger is the attraction between the grafted chains and

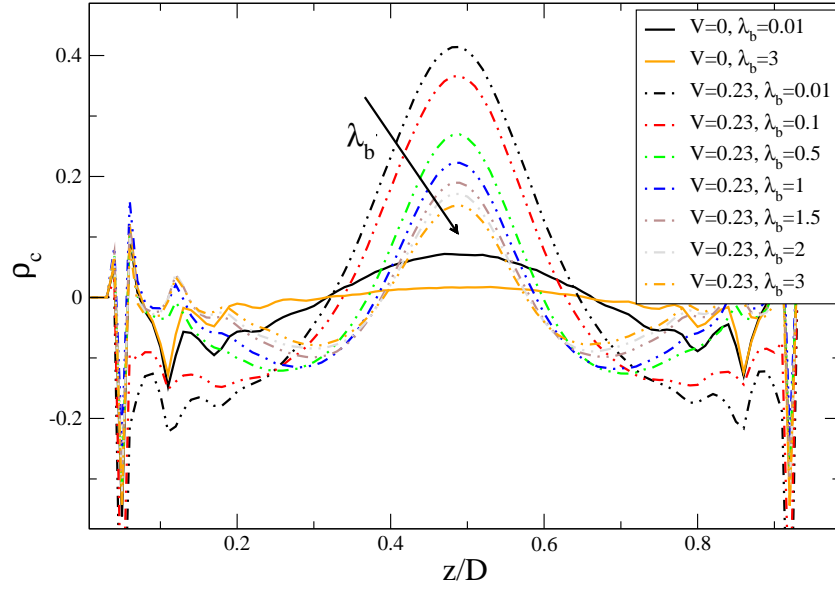


Figure 6.6: Charge distribution for $V=0$ and $V=0.23$ for different Bjerrum lengths. The distance between the walls is $D = 12$, the grafting density $\rho = 2.2\rho^*$, the length of the grafted chains $N = 30$. The stronger the system is charged the less overcharging effects (maximum in the middle of the system) occurs. The effect is stronger upon increasing shear rate.

counterions, and therefore the less counterions are expelled to the middle of the bilayer. The molecular field, which is known theoretically for neutral brushes (see Eq. (1.26)) is modified by the presence of charges. In order to derive a similar theory that describes the power-law behavior of the gyration radius and the shear forces for the charged systems, one has to take into account electrostatic interactions. Two variables are strongly modified, the molecular field, $\phi(z)$, and the electrostatic correlation length. One of the possible ways for taking into account the long-range interactions in the system is to solve the Poisson-Boltzmann equation, Eq. (1.39). Moreover, one has still to take into account excluded volume interactions. All this may deliver an explicit molecular field which may allow to recalculate the interpenetration length for charged bilayers leading finally to a prediction for the dependence of the shear force on the shear rate, as it has been done for neutral bilayers (Chapter 4). However, these calculations are, due to the interplay between electrostatics and excluded volume effects, non-trivial. We leave this for future work.

Chapter 7

Conclusions and outlook

In the present study, we investigated neutral and charged brush-like systems by means of Molecular Dynamics simulations using a classical coarse-grained polymer model.

Investigations of systems consisting of two opposing brushes with soft inclusions (polymer stars), reveal strong modifications of the size and shape of the polymer stars and brushes, compared to the pure polymer-brush bilayer or the stars in the bulk

Both brushes and stars are strongly deformed. Stars experience a significant deformation in all three spatial directions in the presence of the brushes, they become compressed and aspherical. In spite of that the presence of the brushes leads to the decrease of the effective repulsion acting between the stars such that the resulting interaction potential between them is smaller than for brush-free cases. Effective attractions between inclusions mediated by the brushes are found to be to about $40k_{\text{B}}T$ depending on the softness of the stars, chain length, grafting density of the brushes. Increase of the density of the brushes, as well as increase of the functionality of stars, lead to an increase of the attraction. It is shown that the number of beads that belong to the brushes play an important role for this interactions. The closer the stars, the more brush molecules is expelled from the region between the stars. When the stars start overlapping, the number of interactions between the brushes and stars starts decreasing, and effective attractions occur. Decreasing the functionality down to linear chains leads to potentials less than $k_{\text{B}}T$ [119]. In case of fluid brushes, where the grafted chains are allowed to move on the surface without detaching, we expect therefore the effect to become significantly smaller. These investigations are left for future work.

Investigations of the response of two opposing brushes in presence of polymer stars to stationary Couette flows of different shear rates indicate, that the relaxation time of the bilayer is modified by the presence of the stars. The critical shear rate, which separates linear from non-Newtonian response, becomes larger in the presence of stars compared to the star-free case. We varied the compression of the confined layers and their molecular parameters, grafting density and chain length, as well as the functionality of stars and

length of arms. Star-free cases have been compared to systems with inclusions. Our investigations revealed that the increase of the grafting density or the chain length leads to a decrease of the critical shear rate. Moreover, we observe the formation of a fluid layer between the brushes for large shear rates, such that solvent molecules and polymer stars are expelled out of the brushes.

In agreement with previous computer studies (see Refs. in [30] and [31–34, 36, 37]), we observe only small changes of the layer thickness, but a pronounced swelling of polymer chains along the shear direction. This behavior goes along with a non-Newtonian response, i.e. a sublinear increase of the lateral friction force with sliding velocity.

Our data indicates that the swelling of chains in the shear direction can be described by a universal power-law increase of the chain extension (characterized by the radius of gyration) with the Weissenberg number. Using the shear-induced deformation of the grafted chains, we demonstrated how to estimate the critical shear rate. This allows to superimpose the data of all considered parameter combinations, revealing a rather closed picture that relates the chain deformation to the macroscopic response. Despite their distinct differences, systems with stars, star-free cases, and even solvent-free cases[109] can be described consistently. Independently of the star configuration we observe similar responses of the system. The behavior is modified when the stars start dominating the response at large densities.

We developed a scaling theory that allows one to explain the structural changes of the bilayer and its macroscopic response to shear. Our analytical approach is capable of reproducing not only the data stemming from very different numerical models but also recent experimental observations. A central result of our scaling approach is that the critical shear rate, at which the linear response regime is left and non-Newtonian behavior sets in, depends on compression and molecular parameters as

$$\dot{\gamma}^* \propto N^{-2.44} \rho_g^{-0.27} D^{0.6}, \quad (7.1)$$

in the limit of strongly compressed, semidilute brushes with Zimm dynamics (N is the chain length, ρ_g the grafting density, D the distance between grafting planes. A Test of this relation is numerically rather difficult due to the fact that the dependence of $\dot{\gamma}^*$ on grafting density and compression is rather weak. In addition, the parameter regime that can be probed for ρ_g and D is limited because one has to assure strongly compressed brushes. The theory works also for long chains, when the brushes are entangled in static equilibrium. These entanglements have to be released for large Weissenberg numbers($W \gg 1$).

We have shown that the definition of the Weissenberg number via the relaxation time of a single chain of equivalent length in the bulk is not suitable. The relaxation time of such complex systems is strongly dependent on the system parameters.

Our results and previous investigations[18, 35] indicate that the universal macroscopic response, as we report it here for the first time, is not influenced by the type of the solvent molecules incorporated in the system, although the interpenetration between the brushes is strongly influenced by the stars. The structural response is altered when hydrodynamic effects are suppressed in simulations, and when the solvent molecules are completely replaced by the stars, while effectively increasing the size of the solvent molecules[118].

We have demonstrated, that an increase of the size of solvent molecules (replacing dimers by polymer stars) and an increase of the density of included objects lead to the increase of the kinetic friction coefficient. A comparison of systems where solvent molecules are modelled as monomers instead of dimers reveal the same tendency.

Investigations of the non-stationary shear, i.e. shear inversion, show a direct connection between static properties of the system and its dynamic behavior. The characteristic time of each system can be described in terms of the gyration radius and critical shear rate. Independently of the grafting density, the configuration of the stars, the distance between the walls, as well as the shear rate beyond linear response, the behavior of the gyration radius of the brushes, as well as the shear stress, can be explained by a simple scaling approach. The systems in linear response reveal different relaxation behaviors.

We demonstrated that the response of the normal stress to shear inversion show a two-step effect: first an overshooting (depending on the turn time) and then an undershooting. Increase of the turn time, such that shear inversion is performed smoother, leads to a decrease of the overshooting effect, whereas the undershooting remains unaffected. The systems in the linear response regime do not show any response. The effect appears only for shear rates, where non-Newtonian behavior is observed. The larger the shear rate, the larger is the response. Moreover, our investigations revealed, that the presence of the stars leads to an increase of the effect.

While the stars lead to an increase for the response of the normal stress, it overdamps an overshooting of the shear stress. The more stars are in the system, the smoother the shear inversion can be performed. This fact can be crucial for the experiments with oscillatory shear, when inversion is performed several times. Here, large overshooting effect may lead to a rupture break of the grafted chains. Our data show that for long times after shear inversion the total shear stress is almost constant, whereas single components, as e.g. the brush-solvent interaction, are still not fully relaxed. This fact may crucially influence the measurements of the structure and rheological properties in real oscillatory shear experiments.

The structural behavior is modified when brushes are charged. The system exhibit a continuous transition from the neutral to a highly charged behavior. Our measurements show a larger friction coefficient compared to the neutral brushes. Increase of the strength of the Coulomb interaction leads to an increase of the shear forces. Normal forces are influenced only slightly. Both gyration radius and shear forces show a

power-law behavior. A theoretical description, similar to the neutral systems, can be done by taking into account the Poisson-Boltzmann equation. However, we leave these (non-trivial) calculations for future work.

We plan to continue all investigations mentioned above with different inclusions, e.g. bottle brushes, or under modification of the grafted polymers, such that, e.g. both chain ends are grafted to the surfaces or that the grafted linear are replaced by chains with side groups.

We can not change the world right now, but we are making steps forward in understanding it. We live and learn.

Bibliography

- [1] Brown, H. R. *IBM J. Res. Dev.* **1994**, *38*, 379.
- [2] Druelle, M.; Leger, L. *Macromolecules* **1995**, *28*, 7419.
- [3] Ligoure, C. *Macromolecules* **1996**, *29*, 5459.
- [4] Gast, A.; Leibler, L. *Macromolecules* **1986**, *19*, 686.
- [5] Borukhov, I.; Leibler, L. *Phys. Rev. E* **2000**, *62*, R41.
- [6] Wootton, I. A.; Spainhour, L. K.; Yazdani, N. *Compos. for Constr.* **2003**, *7*, 339.
- [7] Pugh, R. J. *Int. J. Miner. Process.* **1989**, *25*, 101.
- [8] Bogusz, E.; Brienne, S.R.; Butler, I.; Rao, S. R.; Finch, J. A. *Miner. Eng.* **1997**, *10*, 441.
- [9] Boulton, A.; Fornasiero, D; Ralston, J. *Int. J. Miner. Process.* **2001**, *61*, 13.
- [10] Stanislav, J. F. *Rheol. Acta* **2005**, *21*, 564.
- [11] Roy, I.; Gupta, M. N. *Chem. Bio.* **2003**, *10*, 1161.
- [12] Advincula, R. C.; Brittain, W. J.; Caster, K. C.; Ruhe, J. (Eds.), *Polymer Brushes*; Wiley-VCH: Weinheim, 2004.
- [13] Muller, M.; Pastorino, C.; Kreer, T.; Binder, K.; MacDowell, L.G. *ACS Abstracts* **2006**, *231*, 416-PMSE.
- [14] Moro, T.; Takatori, Y.; Ishihara, K.; Konno, T.; Takigawa, Y.; Matsushita, T.; Chung, U.; Nakamura, K.; Kawaguchi, H. *Nat. Mater.* **2004**, *3*, 829.
- [15] Klein, J.; Perahia, D.; Warburg, S. *Nature* **1991**, *352*, 143.
- [16] Klein, J. *Annu. Rev. Mater. Sci.* **1996**, *26*, 581.
- [17] Klein, J. *Proc. IMechE J* **220**, 691 (2006).

- [18] Schorr, P. A.; Kwan, T. C. B.; Kilbey II, S. M.; Shaqfey, E. S. G.; Tirrell, M. *Macromolecules* **2003**, *36*, 389.
- [19] Murat, M.; Grest, G. S. *Phys. Rev. Lett.* **1989**, *63*, 1074.
- [20] Lai, P.-Y.; Binder, K. *J. Chem. Phys.* **1993**, *98*, 2366.
- [21] Grest, G. S.; Murat, M. *Macromolecules* **1993**, *26*, 3108.
- [22] Miao, L.; Hong, G.; Zuckermann, M. J. *Macromolecules* **1996**, *29*, 2289.
- [23] Lai, P.-Y.; Lai, C.-Y. *Phys. Rev. E* **1996**, *54*, 6958.
- [24] Grest, G.S.; Kremer, K. *Phys. Rev. A* **1986**, *33*, 3628.
- [25] Kremer K.; Grest, G.S. *J. Chem. Phys.* **1990**, *92*, 5057.
- [26] Grest, G. S. *Phys. Rev. Lett.* **1997**, *76*, 4979.
- [27] Doyle, P. S.; Shaqfeh, E. S. G.; Gast, A. P. *Phys. Rev. Lett.* **1997**, *78*, 1182.
- [28] Saphiannikova, M. G.; Pryamitsyn, V. A.; Cosgrove, T. *Macromolecules* **1998**, *31*, 6662.
- [29] Neelov, I. M.; Borisov, O. V.; Binder, K. *Macromol. Theory Simul.* **1998**, *7*, 141.
- [30] Grest, G. S. In *Advances in Polymer Science*; Granick, S., Eds.; Springer: Berlin, 1999; Vol. 138, p. 149.
- [31] Kreer, T.; Müser, M. H.; Binder, K.; Klein, J. *Langmuir* **2001**, *17*, 7804.
- [32] Irfachsyad, D.; Tildesley, D.; Malfreyt, P. *PhysChemChemPhys* **2002**, *4*, 3008.
- [33] Kreer, T.; Binder, K.; Müser, M. H. *Langmuir* **2003**, *19*, 7551.
- [34] Kreer, T.; Müser, M.H. *Wear* **2003**, *254*, 827.
- [35] Goujon, F.; Malfreyt, P.; Tildesley, D. J. *ChemPhysChem* **2004**, *5*, 457.
- [36] Pastorino, C.; Binder, K.; Kreer, T.; Müller, M. *J. Chem. Phys.* **2006**, *124*, 064902.
- [37] Pastorino, C.; Kreer, T.; Müller, M.; Binder, K. *Phys. Rev. E* **2007**, *76*, 026706.
- [38] Dimitrov, D. I.; Milchev, A.; Binder, K. *J. Chem. Phys.* **2007**, *127*, 084905.
- [39] Brinkman, H. C. *Appl. Sci. Res.* **1947**, *A1*, 27.
- [40] Succi, S. In *The Lattice Boltzmann Equation for Fluid Dynamics and Beyond*; Oxford University Press: Oxford, 2001.

- [41] Malevanets, A.; Kapral, R. *J. Chem. Phys.* **1999**, *110*, 8605.
- [42] Klein, J. *Science* **2009**, *323*, 347.
- [43] McCutchen, C.W. *Wear* **1962**,*5*, 1.
- [44] Raviv, U.; Giasson, S.; Kampf, N.; Gohy, J.F.; Jerome, R.; Klein, J. *Nature* **2003**, *425*, 163.
- [45] P.G. de Gennes, *Scaling concepts in Polymer Physics* (Cornell University Press, 1979).
- [46] Alexander S. *J. Phys* **1977**, *38*, 977.
- [47] Edwards S.F. *Proc. Phys. Soc. London* **1965**, *85*, 613.
- [48] Semenov A.N. *Sov. Phys. JETP* **1985**, *61*, 733.
- [49] Milner, S. T.; Witten, T. A.; Cates, M. E. *Macromolecules* **1988**, *21*, 2610.
- [50] S.T., Milner *Science* **1991**, *251*, 905.
- [51] Netz, R. R.; Schick, M. *Europhys. Lett.* **1997**, *38*, 37.
- [52] Likhtman, A.E.; Semenov, A.N. *Europjs. Letters* **2000**, *51*, 307.
- [53] Matson, M.W. *J. Chem. Phys.* **2002**, *117*, 2351.
- [54] Kim, J.U.; Matson, M.W. *Eur. Phys. J. E* **2007**, *23*, 135.
- [55] Witten, T. A.; Leibler, L.; Pincus, P. A. *Macromolecules* **1990**, *23*, 824.
- [56] Odijk, T. *J. Polym. Sci., Polym. Phys. Ed.* **1977**, *15*, 477.
- [57] Csajka, F.S., Netz, R.R., Seidel, C. *Eur. Phys. J. E* **2003**, *12*, 223.
- [58] Pincus, P. *Macromolecules* **1991** *24*, 2912.
- [59] Zhulina, E.B.; Borisov, O.V. *J. Chem. Phys.* **1997**, *107*, 5952.
- [60] Ripoll, M.; Winkler, R.G.; Gompper, G. *Phys. Rev. Lett.* **2006**, *96*, 188302.
- [61] Ruth., M; Johannsmann, D.; Ruehe J.; Knoll, W. *Macromolecules* **2000**, *33*, 3860.
- [62] Taunton, H.J.; Toprakcioglu, C.; Fetters, L.J.; Klein, J. *Nature* **1988** *332*, 712.
- [63] Auroy, P.; Auvray, L.; Leger, L. *Phys. Rev. Lett.* **1991**, *66*, 719.
- [64] Marques, C.M.; Joanny, J.F.; Leibler, L. *Macromolecules* **1988**, *21*, 1051.

- [65] Hamilton, W.A.; Smith, G.S.; Alcantar, N.A.; Majewsky, J.; Toomey, R.G.; Kuhl, T.L. *J. Polym. Science B* **2002**, *42*, 3291.
- [66] Field J.B.; Toprakcioglu C.; Dai L.; Hadziioannou G.; Smith G.; Hamilton W. *J. Phys. II France* **1992**, *2*, 2221.
- [67] Kent, M.S.; Lee, L.T.; Factor, B.J.; Rondelez, F.; Smith, G.S. *J. Chem. Phys.* **1995**, *103*, 2320.
- [68] Teppner, R.; Motschmann, H. *Macromolecules* **1998**, *31*, 7467.
- [69] Bijsterbosch, H.D.; de Haan, V.O.; de Graaf, A.W.; Mellema, M.; Leermakers, F.A.M.; Cohen Stuart, M.A.; van Well, A.A. *Langmuir* **1995**, *11*, 4467.
- [70] Israelachvili, J.N.; Adams, G.E. *J. Chem. Soc. Faraday Trans.* **1978**, *74*, 975 (1978).
- [71] Balko, S.M.; Kuhl, T.L.; Patten, T.E.; Costanzo, P.J.; Kreer, T.; Johner, A.; Marques, C.M. "Pinning" down the repulsive forces of polymer brushes submitted to *Phys. Rev. Lett.*
- [72] Kelley, T.W.; Schorr, P.A.; Johnson, K.D.; Tirrell, M.; Frisbie, C.D. *Macromolecules* **1998**, *31*, 4297.
- [73] Sauer B.B.; Yu H.; Kim M.W. *Langmuir* **1989**, *5*, 278.
- [74] Allain, C.; Ausserre, D.; Rondelez, F. *Phys. Rev. Lett.* **1982**, *49*, 1694.
- [75] Kawaguchi, M.; Kawarabayashi, M.; Nagata, N.; Kato, T.; Yoshioka, A.; Takahashi, A. *Macromolecules* **1988**, *21*, 1059.
- [76] Cosgrove, T.; Heath, T.G.; Ryan, K.; Crowley, T.L. *Macromolecules* **1987**, *20*, 2879.
- [77] Auroy, P.; Auvray, L. *Macromolecules* **1992**, *25*, 414.
- [78] Kremer, K.; Grest, G. S.; Carmesin, I. *Phys. Rev. Lett.* **1988**, *61*, 566.
- [79] Meyer, H.; Kreer, T.; Cavallo, A.; Wittmer, J. P.; Baschnagel, J. *Eur. Phys. J. - Special Topics* **2007**, *141*, 167.
- [80] Gennis, R.B. *Biomembranes - Molecular Structure and Finction*; Springer Verlag: New York, 1989.
- [81] Kreer, T.; Metzger, S.; Müller, M.; Binder, K.; Baschnagel, J. *J. Chem. Phys.* **2004**, *120*, 4012.
- [82] Kreer T.; Metzger S.; Müller M.; Binder K. *J. Chem. Phys.* **2003**, *120*, 4012.

- [83] D., Frenkel, B., Smit, *Understanding Molecular Simulation, 2nd edition* San Diego, Academic Press, 2002.
- [84] Zhulina, E. B.; Pryamitsyn, V. A.; Borisov, O. V. *Polymer Science USSR* **1989**, *31*, 205.
- [85] Yeh, I.C.; Berkowitz, M.L. *J. Chem. Phys* **1999**, *111*, 3155).
- [86] Irving, J. H.; Kirkwood, J. G. *J. Chem. Phys.* **1950**, *18*, 817.
- [87] Hoogerbrugge, P. J.; Koelman, J. M. V. A. *Europhys. Lett.* **1992**, *19*, 155.
- [88] Espanol, P. *Phys. Rev. E* **1995**, *52*, 1734.
- [89] Espanol, P.; Warren, P. *Europhys. Lett.* **1995**, *30*, 191.
- [90] Groot, R. D.; Warren, P. B. *J. Chem. Phys.* **1997**, *107*, 4423.
- [91] Eiser, E.; Klein, J. *Macromolecules* **2007**, *40*, 8455.
- [92] Tsarkova, L.; Xueyan, Z.; Hadjichristidis, N.; Klein, J. *Macromolecules* **2007**, *40*, 2539.
- [93] Galuschko A. *Dissertation* Strasbourg, 2010.
- [94] Milchev, A.; Dimitrov, D.I.; Binder, K. *Polymer* **2008**, *49*, 3611.
- [95] Ermilov V.; Lazutin A.; Halperin A. *Macromolecules* **2010**, *43*, 3511.
- [96] Darnel, J.; Lodish, H.; Baltimore, D. *Molecular Cell Biology*, Scientific American, New York, 1986.
- [97] Bloom, M.; Evans, E.; Mouritsen, O.G. *Q Rev. Biophys.* **1991**, *24*, 293.
- [98] Lehle, H.; Noruzifar, E.; Oettel, M. *Europ. Phys. J. E* **2008**, *26*, 151.
- [99] Ajdari, A.; Peliti, L.; Prost, J. *Phys. Rev. Lett.* **1959**, *66*, 1483.
- [100] Schmid, F. *Macromol. Rapid. Commun.* **2009**, *30*, 741.
- [101] Sintès, T.; Baumgartner, A. *J. Chem. Phys.* **1996**, *106*, 5744.
- [102] Reynwar, B.J.; Deserno, M. *Biointerphases* **2008**, *3(2)*, FA117.
- [103] Asakura, S.; Oosawa, F. *J. Chem. Phys.* **1954**, *22*, 1255.
- [104] Jusufi, A.; Dzubiella, J.; Likos, C.N.; von Ferber, C.; Lowen, H. *J. Phys.: Condens. Matter*, **2001**, *13* 6177.

- [105] Huang, F.; Addas, K.; Ward, A.; Flynn, N.T.; Velasco, E.; Hagan, M.F.; Dogic, Z.; Fraden, S. *Phys. Rev. Lett.* **2009**, *102*, 108302.
- [106] Clement, F.; Charitat, T.; Johner, A.; Joanny, J.-F. *Europhys. Lett.* **2001**, *54*, 65.
- [107] Semenov A.N. *Langmuir* **1995**, *11*, 3560.
- [108] Cohen C.; Dissertation; Group of Leger L.; Paris.
- [109] Galuschko, A.; Spirin, L.; Kreer, T.; Johner, A.; Pastorino, C.; Wittmer, J.; Baschnagel, J. *Langmuir* **2010**, *26(9)* 6418.
- [110] Yasuda, K.; Armstrong R.C.; Cohen R.E. *Rheol. Acta* **1981**, *20*, 163.
- [111] Joanny, J.-F. *Langmuir* **1992**, *8*, 989.
- [112] Goujon, F. *Dissertation* Clermont-Ferrand, 2003.
- [113] Soddemann, T.; Dünweg, B.; Kremer, K. *Phys. Rev. E* **2003**, *68*, 046702.
- [114] Sirchabesan, M.; Giasson, S. *Langmuir* **2007**, *23*, 9713.
- [115] Israelachvili, J.N. *Intermolecular and surface forces, 2nd edition* London, Academic Press LTD, 1991.
- [116] D. Henderson, D. Boda, *Phys. Chem. Chem. Phys* **2009**, *11*, 3822.
- [117] Kumar, N.A.; Seidel, C. *Phys. Rev. E* **2007**, *76*, 20801.
- [118] Spirin, L.; Galuschko, A.; Kreer, T.; Johner, A.; Baschnagel, J.; Binder, K. *submitted to PRL*.
- [119] Wijmans, C.M.; Zhulina, E.B.; Fleer, G.J. *Macromolecules* **1994**, *27*, 3228.

Curriculum vitae

Name Leonid Spirin
Address Insitute for Physics
Johannes Gutenberg University
Staudingerweg 7
Mainz 55128, Germany
Date of birth 08.02.1985
Place of birth Moscow (Russia)
Nationality Russian
Marital status Single

Academic career

1997-2001 **Gymnasium 1557**, Moscow, Russia
2001-2006 **Moscow State Lomonosov-University (MSU)**
Physics department
Branch of study: Polymer and Crystals Physics,
Computer Simulations
Final degree: Specialist in Physics
2005 - 2006 **Studying and research at the**
Humboldt-University,
Chair of Macromolecules Physics, Berlin (Germany)
Humboldt-University Fellowship
as of 2007 **PhD Student** at the Johannes Gutenberg University,
Mainz (Germany) in the group of Prof. K. Binder